Hazard-Compatible Three-Component Stochastic Ground Motion Simulation for Performance-Based Earthquake Engineering

Sayed Mohammad Sajad Hussaini

UMinho | 2026

Universidade do Minho
Escola de Engenharia

Sayed Mohammad Sajad Hussaini

Hazard-Compatible Three-Component Stochastic Ground Motion Simulation for Performance-Based Earthquake Engineering

Doctoral Thesis
Civil Engineering

July 2026



Universidade do Minho
Escola de Engenharia

Sayed Mohammad Sajad Hussaini

Hazard-Compatible Three-Component Stochastic Ground Motion Simulation for Performance-Based Earthquake Engineering

Doctoral Thesis
Civil Engineering

Supervised by:
Professor Paulo B. Lourenço
Doctor Shaghayegh Karimzadeh
Doctor Sanaz Rezaeian

July 2026

DIREITOS DE AUTOR E CONDIÇÕES DE UTILIZAÇÃO DO TRABALHO POR TERCEIROS

Este é um trabalho académico que pode ser utilizado por terceiros desde que respeitadas as regras e boas práticas internacionalmente aceites, no que concerne aos direitos de autor e direitos conexos. Assim, o presente trabalho pode ser utilizado nos termos previstos na licença abaixo indicada. Caso o utilizador necessite de permissão para poder fazer um uso do trabalho em condições não previstas no licenciamento indicado, deverá contactar o autor, através do RepositóriUM da Universidade do Minho.

Licença concedida aos utilizadores deste trabalho



Atribuição-NãoComercial-CompartilhaIgual
CC BY-NC-SA

https://creativecommons.org/licenses/by-nc-sa/4.0/

Acknowledgements

I would like to express my sincere gratitude to Professor Paulo B. Lourenço for providing the opportunity to carry out this research and for his supervision throughout this work. I am also deeply grateful to Dr. Shaghayegh Karimzadeh for her close guidance, continuous support, and valuable scientific discussions. A special note of thanks goes to Dr. Sanaz Rezaeian for her co-supervision and for graciously hosting me at the U.S. Geological Survey, which contributed to strengthening the novelty and scientific direction of this research.

To my family, you have been my anchor. I am profoundly grateful for your persistent support and belief in me across all these years. To my parents, Sayed Hussain and Zakieh, words can never truly express my gratitude for the values you instilled in me and the endless encouragement that brought me here. To my brother Sayed Bagher, my sisters Fereshteh, Zahra, and Hanieh, and my sweet niece Hoorieh, thank you for keeping me grounded, bringing joy into my days, and always being there when I needed to step away from the research and just be with family.

Above all, my deepest love and gratitude belong to my wonderful wife, Omalbanin. Thank you for standing by my side and for everything we have built together through every challenge and sacrifice. Your strength, patience, and unyielding presence have been the quiet forces that carried me through the hardest days of this journey. And to our sweet son, Sayed Sadra, you are the light that shines in our lives. Your arrival brought an entirely new meaning, joy, and motivation to my world, reminding me every single day of what truly matters.

Finally, I gratefully acknowledge the financial support that made this research possible. This work was conducted within the framework of the STAND4HERITAGE project (New Standards for Seismic Assessment of Built Cultural Heritage), funded by the European Research Council under the European Union's Horizon 2020 research and innovation program through an Advanced Grant (Grant Agreement No. 833123). This work is financed by national funds through FCT (Foundation for Science and Technology), under grant agreement UI/BD/153379/2022 (https://doi.org/10.54499/UI/BD/153379/2022). Furthermore, this research was supported by FCT/MCTES under the R&D Unit Institute for Sustainability and Innovation in Structural Engineering (ISISE), under the references UID/4029/2025 (https://doi.org/10.54499/UID/04029/2025), UID/PRR/04029/2025 (https://doi.org/10.54499/UID/PRR/04029/2025) and UID/PRR2/04029/2025 (https://doi.org/10.54499/UID/PRR2/04029/2025), and under the Associate Laboratory Advanced Production and Intelligent Systems ARISE under reference LA/P/0112/2020 (https://doi.org/10.54499/LA/P/0112/2020).

STATEMENT OF INTEGRITY

I hereby declare having conducted this academic work with integrity. I confirm that I have not used plagiarism or any form of undue use of information or falsification of results along the process leading to its elaboration.
I further declare that I have fully acknowledged the Code of Ethical Conduct of the University of Minho.

Simulação Estocástica de Movimentos do Solo Tridimensionais Compatíveis com a Perigosidade Sísmica para Engenharia Sísmica Baseada no Desempenho

Resumo. Um desafio central na engenharia sísmica baseada no desempenho é a escassez de séries temporais de movimentos do solo tridimensionais (3C) compatíveis com a perigosidade sísmica, necessárias para análises não lineares no domínio do tempo (NRHA). Os modelos empíricos de movimento do solo (GMMs) preveem medidas de intensidade de forma fiável, mas não geram séries temporais; os métodos de simulação estocástica produzem formas de onda completas, mas são difíceis de condicionar a objetivos de perigosidade sem comprometer o realismo físico e as correlações entre componentes; e as abordagens de aprendizagem automática (ML) puramente orientadas por dados podem generalizar mal quando treinadas com os conjuntos de dados reduzidos típicos da prática de engenharia.

Esta dissertação propõe uma abordagem unificada para gerar movimentos do solo estocásticos 3C, compatíveis com a perigosidade sísmica e fisicamente consistentes, sem recorrer a registos históricos de referência nem a ajuste espectral posterior à simulação. A abordagem integra simulação estocástica, modelação estatística multivariada e ML informada pela física.

A primeira contribuição é um método melhorado de simulação estocástica totalmente não estacionária, capaz de reproduzir movimentos de banda larga — incluindo efeitos de diretividade de falhas próximas, de bacias sedimentares e de múltiplas fases de movimento forte — numa formulação unificada, validado com a sequência sísmica de Kahramanmaraş, Turquia (2023), e um subconjunto de registos impulsivos da base PEER NGA-West2.

A segunda contribuição é um enquadramento modular de regressão multivariada com efeitos mistos (MMER) para a modelação conjunta dos parâmetros estocásticos, captando tendências medianas, variabilidade aleatória hierárquica e a estrutura de covariância entre parâmetros correlacionados, com uma arquitetura que admite regressão clássica ou algoritmos de ML.

Com base nestes desenvolvimentos, a dissertação apresenta um enquadramento de simulação condicional em que os parâmetros estocásticos são previstos por um modelo aditivo neuronal informado pela física, aplicado às três componentes ortogonais do movimento. O enquadramento gera formas de onda sintéticas que satisfazem objetivos de perigosidade escalares ou vetoriais, preservando relações empíricas de escala, dependências entre componentes, características espectrais e variabilidade entre registos.

A abordagem proposta estabelece uma ligação prática entre a avaliação da perigosidade sísmica e a geração realista de movimentos do solo estocásticos, permitindo produzir diretamente séries 3C compatíveis com a perigosidade para aplicações de engenharia. As metodologias desenvolvidas estão disponibilizadas como pacotes Python de código aberto (SGSIM, MMER e PINAGMM), apoiando investigação reprodutível e extensível em engenharia sísmica baseada no desempenho.

Palavras-chave: Engenharia sísmica baseada no desempenho, Modelos de movimento do solo, Movimentos do solo compatíveis com a perigosidade sísmica, Movimentos do solo de três componentes, Simulação estocástica de movimentos do solo.

Hazard-Compatible Three-Component Stochastic Ground Motion Simulation for Performance-Based Earthquake Engineering

Abstract. A fundamental challenge in performance-based earthquake engineering is the limited availability of hazard-consistent three-component (3C) ground motion time series required for nonlinear response history analysis (NRHA). While empirical ground motion models (GMMs) reliably predict intensity measures (IMs) for seismic hazard assessment, they do not generate acceleration time series. Conversely, stochastic simulation methods can produce full waveforms but are difficult to condition directly on prescribed hazard targets while preserving physical realism and inter-component correlations. In addition, purely data-driven machine learning (ML) approaches for GMM development may exhibit limited generalization when trained on the relatively small datasets available in engineering practice.

This thesis addresses these limitations by developing a unified end-to-end approach for generating hazard-compatible, physically consistent 3C stochastic ground motions without relying on historical seed records or post-simulation spectral matching. The proposed approach integrates stochastic simulation, multivariate statistical modelling, and physics-informed ML within a conditional generation framework.

The first contribution is an enhanced fully nonstationary stochastic simulation method capable of reproducing broadband earthquake motions, including low-frequency features associated with near-fault directivity, basin effects, and the evolution of multiple strong-motion phases within a unified formulation. The method improves the representation of temporal and spectral nonstationarity while maintaining computational efficiency, and is validated using recorded earthquakes, including the 2023 Kahramanmaraş, Türkiye, earthquake sequence and a pulse-like subset of the PEER NGA-West2 database.

The second contribution is a modular multivariate mixed-effects regression (MMER) framework for jointly modelling the stochastic parameters governing ground motion simulation. Unlike conventional approaches that estimate parameters independently, the proposed framework captures median trends, hierarchical aleatory variability, and the covariance structure among correlated parameters. Its modular structure allows the predictive component to use either classical regression models or ML methods while preserving statistically consistent variance decomposition.

Building on these developments, the thesis introduces a conditional simulation framework in which stochastic parameters are predicted using a physics-informed neural additive model across the three orthogonal ground motion components. By combining physically constrained learning with multivariate statistical conditioning, the framework generates synthetic waveforms that satisfy prescribed scalar or vector-valued hazard targets while preserving empirical scaling relationships, inter-component dependencies, spectral characteristics, and record-to-record variability.

Overall, the proposed approach provides a practical link between seismic hazard assessment and realistic stochastic ground motion generation, enabling the direct production of hazard-compatible 3C time-series for engineering applications. The methodologies developed in this research are released as open-source Python packages (SGSIM, MMER, and PINAGMM), supporting reproducible and extensible research in performance-based earthquake engineering.

Keywords: Ground motion models, Hazard-compatible ground motions, Performance-based earthquake engineering, Stochastic ground motion simulation, Three-component ground motions.

List of Publications

Journal Publications Arising Directly from This Thesis

1. **Hussaini SMS**, Karimzadeh S, Rezaeian S, Lourenço PB. Broadband stochastic simulation of earthquake ground motions with multiple strong phases with an application to the 2023 Kahramanmaraş, Türkiye (Türkiye), earthquake. Earthquake Spectra 2025: 87552930251331981. DOI: 10.1177/87552930251331981. (from Chapter 2)
2. **Hussaini SMS**, Karimzadeh S, Lourenço PB. A Multivariate Mixed-Effects Regression Framework for Ground Motion Modeling: Integrating Parametric and Machine Learning Approaches. Earthquake Engineering & Structural Dynamics 2026: eqe.70168. DOI: 10.1002/eqe.70168 (from Chapter 3)
3. **Hussaini SMS**, Karimzadeh S, Lourenço PB. A Physics-Informed Neural Additive Ground Motion Model for Hazard-Compatible Three-Component Stochastic Simulation. Earthquake Engineering & Structural Dynamics 2026: (Under Review) (from Chapter 4)

Other Journal Publications Completed During the PhD

1. Karimzadeh S, **Hussaini SMS**, Caicedo D, Carvalho A, Rezaeian S, Lourenço PB. Simulated Ground Motion Dataset in the Azores Plateau, Portugal, on Rock and Soil Sites. Journal of Earthquake Engineering 2026: 1–29. DOI: 10.1080/13632469.2026.2619832
2. Temiz C, **Hussaini SMS**, Karimzadeh S, Askan A, Lourenço PB. Seismic scenario simulation and ANN-based ground motion model development on the North Tabriz Fault in Northwest Iran. Journal of Seismology 2025; 29(1): 147–169. DOI: 10.1007/s10950-024-10264-x
3. Bernardo V, Karimzadeh S, Caicedo D, **Hussaini SMS**, Lourenco P. Fragility-Based Seismic Assessment of Traditional Masonry Buildings on Azores (Portugal) Using Simulated Ground Motion Records. Earthquake Spectra 2024. DOI: https://doi.org/10.1177/87552930241256287
4. Karimzadeh S, Mohammadi A, **Hussaini SMS**, Caicedo D, Askan A, Lourenço PB. ANN-based ground motion model for Türkiye using stochastic simulation of earthquakes. Geophysical Journal International 2023; 236(1): 413–429. DOI: 10.1093/gji/ggad432
5. Karimzadeh S, Funari MF, Szabó S, **Hussaini SMS**, Rezaeian S, Lourenço PB. Stochastic simulation of earthquake ground motions for the seismic assessment of monumental masonry structures: Source-based vs site-based approaches. Earthquake Engineering & Structural Dynamics 2024; 53(1): 303–330. DOI: 10.1002/eqe.4012

Table of Contents

Abstract. ..... **vi**

List of Publications ..... **vii**

List of Figures ..... **xi**

List of Tables ..... **xiv**

List of Abbreviations and Symbols ..... **xv**

Chapter 1 Introduction **1**

1.1. Engineering Motivation 1

1.2. Scarcity of Ground Motion Data 1

1.3. Ground Motion Simulation Approaches 2

1.3.1. Physics-Based Deterministic Methods 2

1.3.2. Stochastic Methods 2

1.3.3. Hybrid Simulation Frameworks 3

1.3.4. Validation of Simulated Ground Motions 3

1.4. Site-Based Stochastic Methods 4

1.5. Challenges in Ground Motion Modeling 5

1.5.1. Univariate Constraints and Multivariate Dependencies 5

1.5.2. Trade-offs in Parametric and Data-Driven Frameworks 5

1.6. Bridging Empirical GMMs and Stochastic Simulation 6

1.7. Research Objectives 7

1.8. Thesis Overview 8

Chapter 2 Broadband Stochastic Ground Motion Simulation **9**

2.1. Introduction 9

2.2. Selected Datasets 10

2.3. The Stochastic Ground Motion Model 13

2.3.1. The Reference Model 13

2.3.2. The Limitations 14

2.3.3. The Proposed Improved Stochastic Model 15

2.4. Ground Motion Frequency and Energy Evolution 19
2.4.1. Time-Varying Frequency Content 19
2.4.2. Time-Varying Energy Content 21
2.5. Parameter Identification 21
2.5.1. Parameter Identification for the Filter Function 22
2.5.2. Parameter Identification for the Time-Modulating Function 24
2.6. Validation 26
2.6.1. Visual Qualitative Comparisons of Target and Simulated Motions 26
2.6.2. Quantitative Model Evaluation for the Selected Datasets 31
2.7. Conclusions 36
Chapter 3 Multivariate Mixed-Effects Framework 37
3.1. Introduction 37
3.2. Multivariate Mixed-Effects Modeling Framework 38
3.2.1. General Formulation 38
3.2.2. Estimation of Unknown Parameters 39
3.3. Ground Motion Dataset and Variables 41
3.4. Model Development Methodology 42
3.4.1. Data Processing 43
3.4.2. Fixed-Effects Models 43
3.5. Model Results and Physical Interpretation 45
3.5.1. Overall Model Performance 45
3.5.2. Analysis of Variance 48
3.6. Conclusions 58
Chapter 4 Hazard-Compatible Three-Component Stochastic Simulation 59
4.1. Introduction 59
4.2. Ground Motion Dataset and Parameter Extraction 60
4.2.1. Dataset Selection and Intensity Measures 60
4.2.2. Parameterization of the Stochastic Simulation Method 61

4.2.3. Dataset Preprocessing 63
4.3. Predictive Modeling Framework 63
4.3.1. Physics-Informed Neural Additive Model 63
4.3.2. Multivariate Mixed-Effects Regression 65
4.4. Model Validation and Physical Scaling 66
4.4.1. Predictive Performance 66
4.4.2. Median Physical Scaling 67
4.4.3. Variance Partitioning and Residual Analysis 72
4.4.4. Inter-Parameter and Spectral Correlations 75
4.5. Hazard-Compatible Ground Motion Simulation 78
4.5.1. Unconditional Simulation 78
4.5.2. Spectral Consistency Verification 79
4.5.3. Validation Against Empirical GMMs 80
4.5.4. Conditional Simulation for Prescribed Hazard 81
4.6. Conclusions 83
Chapter 5 Conclusions and Future Research Directions 85
5.1. Introduction 85
5.2. Summary of Research Findings 85
5.3. Broad Scientific Impact and Open-Source Software 86
5.4. Limitations and Future Research Directions 87
References 89
Appendix 95

List of Figures

Figure 2.1. Frequency distribution of the selected ground motions from Kahramanmaraş, Türkiye, earthquake 10
Figure 2.2. Scatter plot of V_{S30} versus R_{JB} for the Kahramanmaraş, Türkiye, earthquake dataset 11
Figure 2.3. Sample ground motion time-series from the Kahramanmaraş, Türkiye, earthquake dataset 11
Figure 2.4. Frequency distribution of the selected ground motions from the NGA-West2 dataset 12
Figure 2.5. Scatter plot of V_{S30} versus R_{JB} for the selected pulse-like NGA-West2 dataset 12
Figure 2.6. Schematic representation of the improved stochastic model in the time and frequency domains. . 16
Figure 2.7. The Kahramanmaraş accelerogram with multiple strong phases 17
Figure 2.8. Parameters of the basic Beta function fitted to the Northridge accelerogram 18
Figure 2.9. Relationships between time-series characteristics of recorded ground motions 19
Figure 2.10. Cumulative mean zero crossings of the target acceleration, velocity, and displacement time-series 23
Figure 2.11. Cumulative mean positive-minima and negative-maxima of the target velocity and displacement time-series 24
Figure 2.12. L'Aquila target motion corresponding to 0.1%–99.9% of the total energy of the input accelerogram. 25
Figure 2.13. Fitted modulating function to target accelerograms and their respective cumulative energy 26
Figure 2.14. Target accelerograms and two alternative simulations using the corresponding fitted models 27
Figure 2.15. Velocity time-series and two alternative simulations using the corresponding fitted models 28
Figure 2.16. Displacement time-series and two alternative simulations using the corresponding fitted models 28
Figure 2.17. Cumulative energy of the target accelerograms and 20 random simulations 29
Figure 2.18. Fourier amplitude spectrum of the target accelerograms and 20 alternative simulations 30
Figure 2.19. Spectral acceleration of the target accelerograms and 20 alternative simulations 30
Figure 2.20. Empirical cumulative distribution function (CDF) of metrics errors for the Kahramanmaraş 32
Figure 2.21. Empirical cumulative distribution function (CDF) of metrics errors for the NGA-West2 32
Figure 2.22. Mean goodness-of-fit (GoF) scores for the east-west (EW) and north-south (NS) components across stations for the Kahramanmaraş, Türkiye, earthquake dataset. 33
Figure 2.23. Mean goodness-of-fit (GoF) scores for the east-west (EW) and north-south (NS) components across record sequence number (RSN) for the NGA-West2 dataset. 34
Figure 2.24. Mean goodness-of-fit (GoF) scores for each metric averaged across all stations, for pulse-like and non-pulse-like motions from the Kahramanmaraş, Türkiye, earthquake dataset. 35
Figure 2.25. Mean goodness-of-fit (GoF) scores for each metric, averaged across all stations, for pulse-like motions from the NGA-West2 dataset 35

Figure 2.26. Correlations between spectral acceleration ordinates.....36
Figure 3.1. Distribution of different seismological parameters of the selected dataset.....42
Figure 3.2. Performance metrics using the test set for SA values across spectral periods.....46
Figure 3.3. Predicted versus actual values for $SA_{0.1}$, $SA_{1.0}$, and $SA_{4.0}$ using the test set.....47
Figure 3.4. Feature importance using SHAP values.....47
Figure 3.5. Epistemic uncertainty in the median predicted spectral acceleration.....48
Figure 3.6. Maximum likelihood estimates of the standard deviation.....50
Figure 3.7. Between-event standard deviation along with 95% confidence intervals.....50
Figure 3.8. Variation of the between-event standard deviation with M_w.....51
Figure 3.9. Variation of unexplained residuals with R_{rup}.....51
Figure 3.10. Variation of between-site residuals with V_{S30}.....52
Figure 3.11. Variation of total effective between-event residuals with M_w.....52
Figure 3.12. Variation of total effective between-event residuals with Z_{tor}.....53
Figure 3.13. Variation of total effective between-event residuals with F_m.....53
Figure 3.14. Variation of the maximum likelihood estimates of total correlation coefficients.....54
Figure 3.15. Variation of the maximum likelihood estimates of total correlation coefficients.....54
Figure 3.16. Variation of the maximum likelihood estimates of total correlation coefficients.....55
Figure 3.17. Scaling relationships for $SA_{0.1}$.....56
Figure 3.18. Scaling relationships for $SA_{1.0}$.....56
Figure 3.19. Scaling relationships for $SA_{4.0}$.....57
Figure 4.1. Distribution of different seismological parameters of the selected dataset.....60
Figure 4.2. Illustrative fit of the Beta modulating function to a sample ground motion record.....62
Figure 4.3. Illustrative comparison of the Fourier Amplitude Spectrum (FAS) for a sample recording against the proposed spectral backbone model.....63
Figure 4.4. Schematic architecture of the physics-informed neural additive model.....64
Figure 4.5. Predictive performance metrics for simulation parameters (major component).....67
Figure 4.6. Predictive performance metrics for intensity measures (major component).....67
Figure 4.7. Median scaling relationship for spread parameter of the major component (S_M).....68
Figure 4.8. Median scaling relationship for total energy of the major component (E_M).....69
Figure 4.9. Median scaling relationship for the lower dominant frequency of the major component ($f_{L,M}$).....70
Figure 4.10. Median scaling relationship for upper dominant frequency of the major component ($f_{U,M}$).....70
Figure 4.11. Median scaling relationship for peak ground acceleration of the major component (PGA_M).....71
Figure 4.12. Median scaling relationship for spectral acceleration at a period of 4.0s of the major component ($SA_{4.0s,M}$).....72

Figure 4.13. Standard deviations of the aleatory components across major-component simulation parameters. 73
Figure 4.14. Standard deviations of the aleatory components across major-component intensity measures.... 73
Figure 4.15. Variation of unexplained within-event residuals with R_{rup}..... 73
Figure 4.16. Variation of between-site residuals with V_{S30}..... 74
Figure 4.17. Variation of between-event residuals with M_w. 74
Figure 4.18. Variation of between-event residuals with Z_{tor}..... 75
Figure 4.19. Total correlation matrix of the simulation parameters 76
Figure 4.20. Total correlation matrix of the simulation parameters and intensity measures 77
Figure 4.21. Total correlation coefficients of spectral acceleration (SA) at representative periods (0.1, 1.0, and 4.0 s)..... 78
Figure 4.22. Qualitative visualization of simulated major, intermediate, and vertical component time-series ... 79
Figure 4.23. Comparison of spectral accelerations from stochastic simulations (SA_{Sim}) and the corresponding predicted empirical values (SA_{NAM})..... 80
Figure 4.24. Comparison of spectral accelerations from stochastic simulations (SA_{Sim}), the corresponding predicted empirical values (SA_{NAM}), and predictions from reference ground motion models..... 81
Figure 4.25. Comparison of spectral accelerations from stochastic simulations (SA_{Sim}) and the corresponding predicted empirical values (SA_{NAM}) conditioned on $SA_{1.0s}$..... 82
Figure 4.26. A direct comparison of unconditional versus conditional ground motion simulation. 83

List of Tables

Table 2.1. Seismological characteristics of example target accelerograms 12
Table 2.2. Parameters of the filter function fitted to target accelerograms. 24
Table 2.3. Parameters of the modulating function fitted to target accelerograms. 25
Table 2.4. Errors associated with Fourier amplitude spectrum (FAS) and spectral acceleration (SA) 31
Table 3.1. Validation of the MMER numerical optimization against the standard lme4 45
Table 3.2. Average model performance across all SA values. 46
Table 4.1. Summary of physical constraints and hyperparameters for grouped variables. 65
Table 4.2. Average model performance metrics across all response variables (ln units). 66

List of Abbreviations and Symbols

Symbol / Abbreviation	Definition	Chapters
Seismological Input Parameters		
M_w	Moment magnitude	2, 3, 4
R_{JB}	Joyner-Boore distance (km)	2, 3, 4
R_{rup}	Closest distance to rupture plane (km)	2, 3, 4
V_{S30}	Time-averaged shear-wave velocity in the top 30 m of soil (m/s)	2, 3, 4
Z_{tor}	Depth to the top of the rupture plane (km)	3, 4
F_m	Fault mechanism (strike-slip, normal, reverse, etc.)	3, 4
Intensity Measures (IMs)		
IM	Intensity measure (general)	1, 3, 4
PGA	Peak ground acceleration	1, 2, 3, 4
PGV	Peak ground velocity	1, 2, 3, 4
PGD	Peak ground displacement	2
SA(T)	5%-damped spectral acceleration at period T	1, 2, 3, 4
SV(T)	Spectral velocity at period T	2
SD(T)	Spectral displacement at period T	2
RotD50	Orientation-independent median SA (median over all horizontal rotation angles)	3, 4
Stochastic Simulation — Time-Modulating Function		
x(t)	Simulated acceleration time-series	2
q(t, α)	Time-modulating function with parameter vector α	2
w(t)	Gaussian white noise process	2
E_t / E	Total energy of the ground motion ($g^2 \cdot s$)	2, 4
D	Total significant duration of strong shaking (s)	2, 4
C	Energy centroid, temporal center of seismic energy release (s)	4
S	Energy spread, effective active duration of strong motion (s)	4
C_r	Normalized energy centroid ratio ($0 < C_r < 1$)	4
S_r	Relative dispersion of energy arrival	4
P	Ratio of peak-amplitude time to total duration	2
C	Energy-concentration parameter around the peak time	2
α_i	Fraction of total energy in the i^{th} strong-motion phase	2
Stochastic Simulation — Spectral Filter Parameters		
h(t, λ(t))	Impulse response function of the evolutionary band-pass filter	2
H(w, λ(t))	Frequency response function of the evolutionary band-pass filter	2
ω_l / f_L	Lower dominant angular/cyclic frequency of the band-pass filter (rad/s or Hz)	2, 4
ω_u / f_U	Upper dominant angular/cyclic frequency of the band-pass filter (rad/s or Hz)	2, 4
ζ_l	Damping ratio for the lower dominant-frequency sub-filter	2
ζ_u	Damping ratio for the upper dominant-frequency sub-filter	2
ω_c	Low-cut angular frequency of the post-simulation high-pass filter (reference model)	2
sh(t)	Variance normalization function of the integral process	2
Stochastic Simulation — Spectral and Energy Descriptors		
FAS	Fourier amplitude spectrum	2, 4
PSD	Power spectral density	2
CE(t)	Cumulative energy up to time t	2
MZC	Mean zero-crossing rate	2
MLE	Mean local-extrema rate	2
MPMNM	Mean positive-minima and negative-maxima rate	2
Φ_E	Expected evolutionary power spectral density	2
Ground Motion Component Directions		
M	Major horizontal component (principal axis of maximum energy)	4
I	Intermediate horizontal component (principal axis of minimum energy)	4

Symbol / Abbreviation	Definition	Chapters
V	Vertical component	4
EW	East-west as-recorded direction	2
NS	North-south as-recorded direction	2
3C	Three-component (ground motion)	All chapters
θ_p	Rotation angle for principal-axis transformation	4
Statistical Model — MMER Framework		
y	Vector of multivariate response variables	3, 4
f(x)	Fixed-effects component (parametric or ML-based)	3, 4
b_i	Random-effects vector for the i-th grouping factor	3, 4
ε	Within-group residual vector	3, 4
Φ	Core residual covariance matrix (between-response, m x m)	3
τ_i	Core random-effects covariance matrix for grouping factor i	3
V	Marginal covariance matrix of the observations	3
L_m	Marginal log-likelihood	3
μ_i	Posterior mean of random effects (BLUP)	3
Σ_i	Posterior covariance of random effects given data	3
η_j	Multivariate between-event residual for earthquake j	4
δ_k	Multivariate between-site residual for station k	4
Σ_{event}	Between-event covariance matrix	4
Σ_{site}	Between-site covariance matrix	4
$\Sigma_{residual}$	Within-event (record-to-record) covariance matrix	4
Σ_{total}	Total covariance matrix (sum of all three components)	4
Neural Additive Model (NAM)		
$f_i(x_i)$	Isolated subnetwork output for the i-th predictor in the NAM	4
β_0	Global bias term of the NAM	4
μ_{NAM}	Median predictive vector from the NAM (fixed effects)	4
Y_{sim}	Sampled synthetic response vector	4
$\mu_{a\|IM}$	Conditional mean of simulation parameters given target IMs	4
$\Sigma_{a\|IM}$	Conditional covariance after conditioning on target IMs	4
Performance and Goodness-Of-Fit Metrics		
GoF	Goodness-of-fit score (Olsen and Mayhew, 2010)	2
CDF	Empirical cumulative distribution function	2
R_2	Coefficient of determination	3, 4
R	Pearson correlation coefficient	3, 4
MAE	Mean absolute error	3, 4
RMSE	Root mean squared error	3, 4
SHAP	Shapley additive explanations (feature importance)	3
ε_M	Normalized error for validation metric M	2
Ground Motion Databases and Record Identifiers		
NGA-West2	PEER Next Generation Attenuation for Western US database	2, 3, 4
ESM	Engineering Strong Motion (pan-European) database	2
RSN	Record sequence number (NGA-West2)	2
NR	Northridge 1994 example accelerogram identifier	2
IV	Imperial Valley 1979 example accelerogram identifier	2
LA	L'Aquila 2009 example accelerogram identifier	2
KM	Kahramanmaraş 2023 example accelerogram identifier	2
Abbreviations		
PBEE	Performance-based earthquake engineering	1, 4, 5
PSHA	Probabilistic seismic hazard analysis	3, 4
NRHA	Nonlinear response history analysis	1, 4
GMM	Ground motion model (also: ground motion prediction equation)	1, 3, 4
MMER	Multivariate mixed-effects regression (framework and Python package)	3, 4, 5
NAM	Neural additive model	4, 5
MLP	Multi-layer perceptron (feedforward neural network)	3, 4
ANN	Artificial neural network	3
ML	Machine learning	1, 3, 4

Symbol / Abbreviation	Definition	Chapters
MLE	Maximum likelihood estimation	3, 4
EM	Expectation-maximization algorithm	3
BLUP	Best linear unbiased predictor	3
SDoF	Single degree of freedom (oscillator)	2
MDoF	Multi-degree of freedom (system)	2
IRF	Impulse response function	2
FRF	Frequency response function	2
LTV	Linear time-variant (filter)	2
STFT	Short-time Fourier transform	2
CWT	Continuous wavelet transform	2
LR	Linear regression model	3
MI	MLP with random intercepts only	3
MS	MLP with random intercepts and M_w slope	3
BSSA14	Boore et al. (2014) horizontal GMM reference model	4
BC16	Bozorgnia and Campbell (2016) vertical GMM reference model	4
SGSIM	Open-source Python package for stochastic ground motion simulation	2, 4, 5
PINAGMM	Open-source Python package implementing the hazard-compatible 3C simulation framework	4, 5

Chapter 1
Introduction

1.1. Engineering Motivation

A fundamental objective of modern performance-based earthquake engineering (PBEE) is the rigorous characterization of seismic hazard and the subsequent evaluation of structural performance under anticipated demands [1]. Within contemporary probabilistic frameworks, seismic hazard is typically quantified using discrete intensity measures (IMs), commonly peak ground acceleration (PGA), peak ground velocity (PGV), and the 5%-damped spectral acceleration (SA) at a structure's fundamental period, evaluated at specific annual probabilities of exceedance [2].

To accurately assess structural responses at these target hazard levels, modern engineering practice should rely on nonlinear response history analysis (NRHA) [3]. High-fidelity NRHA requires suites of ground motions that are consistent with the target hazard scenario. However, recorded ground motion databases remain sparse and unevenly distributed, particularly for high-magnitude, near-fault, or extreme intensity levels most relevant to engineering design [4]. At the same time, advances in computational capacity and numerical modeling capabilities have made NRHA increasingly feasible for routine assessment of structural systems, increasing the demand for realistic seismic input ground motions.

To capture realistic structural performance, these analyses must look beyond isolated horizontal axes. Comprehensive NRHA requires the simultaneous consideration of all three translational components of earthquake ground motion (two orthogonal horizontal components and one vertical component). This three-component (3C) evaluation is vital for spatial structural configurations, where multidirectional excitation governs global dynamic response, torsional coupling, and complex failure mechanisms [5]. While seismic design has traditionally emphasized horizontal shaking, the vertical component can be equally important, especially in near-fault regions where vertical accelerations may approach or even exceed horizontal levels at short spectral periods [6,7]. Strong vertical ground motions can significantly alter gravity-related axial forces, leading to structural instability, variations in column demands, and accelerated degradation in both vulnerable structural members and non-structural components.

These considerations highlight that realistic seismic assessment requires 3C ground motions that not only capture key seismological characteristics, such as amplitude, spectral content, temporal nonstationarity, and duration, but also preserve the physically consistent cross-correlation across all three orthogonal directions.

1.2. Scarcity of Ground Motion Data

Despite the explicit need for 3C ground motion time-series in NRHA, bridging the gap between empirical probabilistic seismic hazard assessment and physical waveform simulation remains an outstanding challenge. A primary constraint is the sparsity of recorded ground motion data. Despite the steady global expansion of strong motion networks, recorded databases remain critically sparse for site-specific analyses involving extreme, low-probability, or rare design scenarios [8,9]. To circumvent this data deficit, practitioners traditionally select real records from alternative geographic regions with different seismological characteristics, adjusting them via scaling or spectrum-matching techniques [10,11]. These methods may alter the correlation between important ground motion characteristics and their original physical conditions. Consequently, these operations may provide waveforms with unrealistic characteristics and energy distributions [12,13].

Therefore, a realistic estimation of structural demands requires ground motions that adequately represent earthquake source characteristics, wave-propagation effects, and local site conditions. For this reason, ground motion simulation has become an important tool in both seismology and earthquake engineering, and has been widely applied across a broad range of research and engineering applications worldwide (e.g., [14–20]). Yet, a major practical challenge remains. High-fidelity simulation frameworks typically require specialized seismological expertise and substantial computational resources. As a result, pre-validated and readily accessible synthetic ground motion suites are rarely available for engineering applications across diverse seismic regions [8].

1.3. Ground Motion Simulation Approaches

When generating synthetic motions, engineers must balance computational efficiency with physical realism. To address the data scarcity constraints inherent to empirical datasets, various ground motion simulation methodologies have been developed over the past several decades. In the existing literature, these approaches can be broadly categorized into three primary classes based on their underlying formulation: physics-based deterministic methods, stochastic methods, and hybrid frameworks [21]. Furthermore, as these methods have matured, the engineering community has placed a critical emphasis on the rigorous validation of these simulations to ensure their reliability in practical applications.

1.3.1. Physics-Based Deterministic Methods

Physics-based deterministic methods, or source-based deterministic formulations, simulate earthquake rupture on the fault and the subsequent propagation of seismic waves through a characterized three-dimensional (3D) crustal medium. These frameworks solve the elastodynamic equations governing seismic wave propagation across regional velocity structures using advanced numerical techniques, such as finite-difference or spectral-element methods [22]. Substantial research has refined these approaches, advancing the description of kinematically or dynamically complex source rupture processes [23–26] and wave propagation mechanics through heterogeneous media [27,28]. Characteristically, deterministic simulations excel at capturing low-frequency ground motion components, including long-period waveforms and coherent phase arrivals. Nonetheless, these methods require prohibitive computational resources and exhaustive, highly detailed knowledge of crustal geology and fault geometry. Because this level of deep seismological data is rarely available for specific engineering sites, pure deterministic simulations are seldom viable for routine structural design applications.

1.3.2. Stochastic Methods

Stochastic methods bypass explicit wave propagation modeling by treating ground motion time-series as random processes. The underlying statistical parameters of these processes are either theoretically derived from simplified physical models or empirically calibrated against databases of real recordings [29–31]. While deterministic methods accurately resolve low-frequency ranges, stochastic methods are highly regarded for their capacity to capture high-frequency content, which is driven by complex, scattering phenomena and directly governs the dynamic response of most common engineering structures [22]. Within the literature, stochastic approaches are further subdivided into two categories:

- **Source-Based Stochastic Approaches:** These methods analytically shape and scale a theoretical earthquake source spectrum by incorporating parametric path attenuation and local site effects [29,30,32]. However, these parameters are highly region specific and require calibration across distinct geological zones, restricting their immediate deployment in regions lacking extensive historical instrumentation [33,34].
- **Site-Based Stochastic Approaches:** These methods represent ground motions directly at a target site using a stochastic process calibrated to capture the evolutionary characteristics

(e.g., intensity and frequency nonstationarity) of recorded accelerograms. Because they demand fewer input parameters and require a fraction of the computational resources of source-based methods, they offer a highly practical alternative for engineering design applications [22].

Stochastic approaches, despite their advancements, still face limitations in capturing low-frequency content and modeling multiple strong motion phases without a deterministic component. This fundamental limitation was vividly highlighted during the 2023 Kahramanmaraş, Türkiye (M_w 7.8) earthquake sequence. Studies modeling this devastating event, even using a source-based stochastic finite-fault method, struggled to capture its diverse characteristics, including near-fault directivity pulses, low-frequency basin amplifications, and multi-phase shaking, without a deterministic component [35].

1.3.3. Hybrid Simulation Frameworks

Hybrid methods attempt to combine the advantages of both paradigms, leveraging physics-based deterministic formulations to model low-frequency wave content and stochastic formulations to generate high-frequency components. While capable of producing synthetic broadband ground motions across the entire frequency spectrum, these frameworks remain structurally complex. Furthermore, their efficacy is often constrained by systematic modeling artifacts and energy discontinuities at the transition frequency where the deterministic and stochastic components are numerically merged [36].

1.3.4. Validation of Simulated Ground Motions

Regardless of the simulation methodology employed, rigorous validation of simulated ground motions is necessary for hazard analysts, practicing engineers, and regulatory bodies to be confident in their use. Historically, validation exercises were primarily limited to basic comparisons of simulated-to-observed waveforms and median values of spectral accelerations for selected historical earthquakes. However, the concept of validation has evolved significantly into a broad field of active multidisciplinary research [8].

Modern validation frameworks recognize that testing must extend beyond simple waveform matching to account for the actual needs of the engineering community. Validation metrics are now broadly categorized into two main groups [8]:

- **Ground Motion Characteristics:** These metrics move beyond basic spectral acceleration to include scalar parameters (e.g., Arias intensity, significant duration), goodness-of-fit combined metrics, and non-scalar evolutionary parameters that track intensity and frequency content over time.
- **Structural Responses:** Simulated motions are applied to computational models of structures to evaluate engineering demand parameters (EDPs). These structural proxies act as validation tools for engineered systems, evaluating metrics such as the correlation of spectral acceleration across periods, the ratio of maximum-to-median spectral acceleration across horizontal orientations, and the ratio of inelastic-to-elastic displacement [8,37].

Contemporary validation approaches generally rely on two comparative baselines: directly comparing simulations to historical records or comparing simulated metrics against established empirical ground motion models (GMMs). Furthermore, recent frameworks propose a multi-level validation hierarchy [8,38]:

1. Historical Validation: Site-by-site comparisons of simulations against available ground motion records.

2. Scenario Validation: Checking probability distributions of ground motion IMs across a broad frequency range and analyzing residuals with respect to empirical GMMs.

3. Code-Based Engineering Validation: Using spectrum-compatible accelerograms for the seismic design and inelastic assessment of realistic structures.

Ultimately, a key lesson from recent validation research is that validation is highly application specific. A simulation method may produce acceptable median spectral accelerations for GMM development but remain deficient for NRHA, if it fails to capture appropriate durations or inter-period correlations. Consequently, the development of end-to-end simulation frameworks must inherently account for these complex multivariate parameters to produce truly hazard-compatible and physically consistent ground motions.

Given the constraints of computational resources and the lack of deep seismological fault data for routine engineering projects, site-based (also known as site-compatible) stochastic approaches represent the most practical path forward for this research. Therefore, the following section provides a detailed classification and review specifically focused on site-based stochastic methods.

1.4. Site-Based Stochastic Methods

Due to their engineering practicality, site-based stochastic methods remain a vital tool. The defining feature of these methods is the mathematical formulation used to generate, modulate, and filter an underlying random process so that the simulated motions reproduce the engineering characteristics of target ground motion recordings. Existing site-based methods can be broadly classified into five primary categories [22]:

- **Time-Modulated Filtered White Noise:** These formulations pass a stationary white noise process through a time-invariant or time-varying filter, subsequently applying time-modulating envelopes to capture the temporal build-up and decay of earthquake energy [31,39–41].
- **Filtered Poisson Pulse Trains:** These methods construct synthetic time-series by superimposing a sequence of distinct, randomly arriving Poisson pulses passed through a linear filter to match specific amplitude trends [42].
- **Auto-Regressive Moving Average (ARMA) Models:** These methods are based on discrete-time stochastic processes that capture nonstationarity by systematically varying ARMA coefficients over successive time windows [43].
- **Direct Spectral Representations:** These methods deploy short-time Fourier transforms (STFT) or continuous wavelet transforms (CWT) to decompose real records into the time-frequency domain and subsequently reconstruct synthetic energy densities [9,44,45].
- **Data-Driven Machine Learning Methods:** These methods encompass recently developed frameworks based on nonparametric algorithms, such as Gaussian process regression, to learn evolutionary ground motion characteristics directly from strong motion datasets [46,47].

Most existing site-based methods rely predominantly on mathematical or statistical indicators rather than parameters with meaningful physical interpretations. Some studies have incorporated physically meaningful parameters [31] or mapped them to seismological explanatory variables (e.g., magnitude, distance) via empirical regression relationships [43,48]. However, explicitly accommodating complex physical phenomena, such as near-fault directivity pulses, long-period basin amplifications, or multiple strong phase shaking, within these frameworks has traditionally required increasing model complexity. For instance, to simulate directivity-induced velocity pulses, researchers have typically superimposed independent, deterministic directivity pulse models onto the stochastic background motion [40,49]. Similarly, to capture multiple peak frequencies within the evolutionary power spectral density (PSD), various models have integrated sequential high-pass and low-pass filtering schemes [45,49].

Nonetheless, additional post-simulation high-pass filtering is still required in most site-based stochastic methods to remove undesired low frequencies. Filtering the low-frequency content after generating synthetics can lead to an implicit average bias that tends to underestimate the total energy of the synthetic record. Consequently, studies have resorted to correction factors as a post-simulation solution for addressing energy bias in simulations (e.g., [40]).

1.5. Challenges in Ground Motion Modeling

To effectively deploy stochastic simulations for a prescribed seismic hazard scenario, the underlying simulation parameters must be accurately predicted using GMMs. GMMs, also known as ground motion prediction equations, are a fundamental component of modern probabilistic seismic hazard analysis (PSHA). These models are often empirical relationships that predict the distribution of ground motion IMs, such as PGA, PGV, and SA at different periods, as a function of key parameters describing the earthquake source, wave travel path, and local site conditions. The development of robust GMMs has been the focus of many research efforts over the past decades (e.g., [50–58]).

A central requirement of modern PSHA is accounting for the statistical dependence observed between aleatory residuals of SA across neighboring spectral periods [59,60]. This dependence structure is critical for correctly propagating uncertainty in hazard analysis and in downstream NRHA.

1.5.1. Univariate Constraints and Multivariate Dependencies

Conventionally, GMMs are developed by first fitting separate mixed-effects models for each IM (e.g., SA at a given period) to estimate median trends and variance components (e.g., between-event and within-event terms). In a subsequent step, the correlations between IMs are then constructed, either through empirical estimation of residual dependence or through predefined correlation models (e.g., [50,53,59–61]), rather than being integrated during the regression process. While computationally convenient, this approach treats marginal variance estimation and covariance construction as independent processes. By failing to solve these parameters within a unified mathematical framework, it prevents the joint exploitation of shared statistical information across response variables.

It is noteworthy that multivariate mixed-effects implementations have been explored in previous research (e.g., [62–65]), demonstrating the theoretical benefits of joint estimation. Similarly, recent advances in functional data analysis (e.g., [66]) have proposed modeling the full response spectrum as a continuous function.

Furthermore, an ongoing issue in modern GMM development is heteroscedasticity, where aleatory variabilities may depend on moment magnitude. Recent studies have shown that both the variance and the overall correlation of many IMs are magnitude dependent. However, due to numerical instabilities in modeling magnitude-dependent correlations, a simpler homoscedastic (magnitude-independent) assumption is often adopted for these components [53,56].

1.5.2. Trade-offs in Parametric and Data-Driven Frameworks

Traditional parametric GMMs rely on pre-defined, highly structured functional forms to capture seismological phenomena such as geometric spreading, magnitude saturation, and site amplification [50,51,53,54]. While these forms are grounded in seismological principles, they may not fully represent nonlinear dependencies and interactions in ground motion data. Although this epistemic uncertainty is typically addressed in hazard analysis via logic trees by weighting multiple models, the individual parametric models themselves may still be limited by their pre-defined functional structures, potentially introducing bias. This challenge is particularly relevant when characterizing complex nonlinear scaling effects that deviate from standard functional assumptions, for less-studied IMs, or when developing regression frameworks for indirect applications, such as jointly predicting the correlated input parameters required by stochastic ground motion simulation methods (e.g., [4,48,67]).

The expansion of global strong motion data and advances in machine learning (ML) provides a strong foundation for developing flexible, data-driven GMMs. ML methods, such as artificial neural networks (ANNs), have demonstrated strong predictive performance for a wide range of IMs, comparable to conventional GMMs [52,55,57,68,69].

However, these methods often require relatively larger datasets to learn robust patterns and avoid overfitting, a requirement that can be met using extensive recorded databases or simulated ground motions (e.g., [55,70]). When trained on sparse or highly scattered ground motion datasets, unconstrained networks may overfit and exhibit poor extrapolation outside the range of observed seismological conditions. Additionally, without physical or statistical constraints, such models may violate key scaling behaviors, including monotonic distance attenuation or failure to capture magnitude saturation.

Crucially, a simple black-box application of ML is insufficient. It can obscure physical interpretation and fail to properly handle the unique, hierarchical structure of ground motion data, where recordings from the same earthquake or station are not statistically independent. Standard ML frameworks do not explicitly represent the hierarchical variance structure (e.g., between-event variability) that is essential for accurately partitioning aleatory variability in modern GMM formulation.

To address this, a rigorous GMM must decompose total uncertainty into its constituent components, a task typically handled using mixed-effects regression. The one-stage maximum-likelihood algorithm, first applied to GMM development by Brillinger and Preisler [71] and subsequently refined by Abrahamson and Youngs [72], has been widely referenced in the GMM literature for iteratively estimating fixed-effects coefficients and variance components in univariate, parametric, linear mixed-effects formulation of GMMs. Jayaram and Baker [73] proposed extensions to account for the spatial correlation of within-event residuals, and Mohammadi et al. [74] proposed modifications to the likelihood formulation, resulting in an algebraic solution with improved computational efficiency.

While robust software packages such as lme4 [75] in R programming language are widely used for conventional generalized linear mixed-effects analyses, their design focuses on univariate responses with parametric fixed-effects structures. Some packages provide support for multivariate outcomes, but they generally do not natively allow the fixed-effects component to be replaced by a nonparametric machine learning algorithm (e.g., ANNs) within the mixed-effects estimation. Additionally, fully estimating correlations across many response variables in a single stage can be cumbersome or not directly supported.

The typical approach in developing parametric GMMs is to apply a separate univariate mixed-effects regression for each IM. While modern ML approaches often use multi-output architectures to predict vectors of IMs simultaneously (e.g., [76]), the rigorous joint estimation of the full inter-response covariance matrix for the random effects is rarely integrated directly into the training process. Using ML iteratively within the mixed-effects framework ensures proper accounting for latent random effects, as demonstrated in recent studies where the likelihood is maximized iteratively (e.g., [68,74,76,77]). In contrast to these rigorous approaches, a simple one-time fit using ML followed by residual analysis essentially behaves like a fixed-effects-only model and should be avoided. Notably, Campbell and Bozorgnia [53] demonstrated that variance components estimated directly from the point estimates of random effects are biased due to statistical shrinkage. Specifically, the empirical standard deviation of these shrunk estimates systematically understates the true between-event variability. Accurate variance partitioning requires a fully specified mixed-effects formulation to correctly recover the population variance parameters.

1.6. Bridging Empirical GMMs and Stochastic Simulation

Despite substantial advancements in empirical ground motion modeling, bridging the gap between the statistical prediction of discrete IMs and the simulation of continuous physical ground motions remains a fundamental challenge.

While crucial for PSHA, GMMs do not generate the ground motion time-series required for NRHA. To address this limitation, site-based stochastic ground motion simulation models have been widely adopted to generate synthetic acceleration waveforms for specified earthquake scenarios (e.g., [48,67]). However,

achieving strict compatibility with target hazard levels (e.g., conditional SA values) in the resulting motions remains challenging. When generating orthogonal horizontal ground motions in these models, inter-component correlation is often introduced through empirical residual-based post-processing rather than being natively enforced within a unified, covariance-based mathematical framework.

More recent studies have explored wavelet-based stochastic simulation approaches that achieve hazard consistency through spectrum-compatible ground motions, incorporating inter-component correlation for orthogonal horizontal components via empirical inter-period correlation models [78]. Although effective for generating spectrum-compatible motions, these approaches generally depend on the availability and selection of suitable historical seed records. This reliance on seed records and post-simulation corrections ultimately underscores a critical missing link, namely the need for a unified methodological approach that directly bridges multivariate IM prediction and stochastic simulation to natively generate hazard-compatible, 3C ground motions.

1.7. Research Objectives

The overall objective of this doctoral research is to develop an end-to-end generative framework for producing hazard-compatible, physically consistent, 3C synthetic ground motions for PBEE, entirely eliminating the reliance on historical seed records, empirical selection and scaling procedures, or spectral matching. To achieve this, the core philosophy of this research is fundamentally methodological, rather than an application-oriented study. Accordingly, the research is structured into four interrelated sub-objectives:

- **Enhancement of Site-Based Stochastic Formulation:** This objective focuses on improving traditional time-modulated filtered white-noise methods by changing the sequence of modulation and filtering operations to better preserve low-frequency content and avoid artificial loss of energy. A modular stochastic structure is developed in which frequency filtering, and time modulation can be treated as interchangeable components. This allows easier extension of the framework to address multiple strong phase ground motions and improves its applicability to complex real earthquake recordings.
- **Development of a Modular Multivariate Mixed-Effects Statistical Framework:** A unified statistical framework is established to jointly estimate the full inter-response covariance structure across multiple correlated variables. The framework allows the fixed-effects component to adopt either parametric representations or nonparametric ML models. It performs a single-stage joint estimation of random effects, avoiding the limitations of the "separate-then-correlate" approach and reducing biases associated with shrinkage effects in hierarchical estimation.
- **Integration of Physical Scaling Laws into ML Models:** Nonparametric neural networks are embedded within a mixed-effects statistical structure, with explicit enforcement of structural monotonicity and physics-based constraints. This integration is intended to improve generalization performance on unseen data, mitigate overfitting on sparse datasets, and ensure strict consistency with established seismological scaling relationships governing ground motion attenuation and magnitude saturation.
- **Development of a Conditional Ground Motion Simulation Framework:** The statistical framework is mapped directly onto the parameters of the enhanced stochastic formulation to enable exact multivariate normal conditioning using key IMs. This final objective facilitates the direct generation of full 3C ground motions that are explicitly conditioned on a specified hazard level, preserving physically consistent inter-component cross-correlations without requiring historical seed motions.

1.8. Thesis Overview

This doctoral thesis is organized into five chapters. The core research chapters (Chapters 2, 3, and 4) form a coherent methodological progression, from foundational simulation methods to advanced statistical inference, and finally to conditional waveform simulation within a unified framework integrating physical modeling, statistical learning, and data-driven components.

- **Chapter 2** presents an enhanced nonstationary stochastic simulation method, establishing the physical basis for generating realistic ground motion waveforms.
- **Chapter 3** introduces a modular multivariate mixed-effects regression (MMER) framework for statistical modeling, providing a rigorous method to quantify joint covariance structures across multiple IMs.
- **Chapter 4** integrates these physical and statistical components into a conditional generative framework, enabling the simulation of 3C ground motions that satisfy vector-valued hazard constraints.
- **Chapter 5** concludes the thesis by summarizing the primary findings, highlighting the broader impacts on PBEE, and proposing future research directions.

Chapter 2
Broadband Stochastic Ground Motion Simulation

The contents of this chapter have been published in Earthquake Spectra. Minor formatting and structural modifications have been made to align with the overarching thesis narrative. The original article may be cited as:
Hussaini SMS, Karimzadeh S, Rezaeian S, Lourenço PB. Broadband stochastic simulation of earthquake ground motions with multiple strong phases with an application to the 2023 Kahramanmaraş, Türkiye (Türkiye), earthquake. Earthquake Spectra 2025: 87552930251331981. DOI: 10.1177/87552930251331981

2.1. Introduction

Site-based stochastic simulation methods provide a practical and computationally efficient approach for generating realistic ground motion time-series for nonlinear response history analysis (NRHA). Among the available formulations, the fully nonstationary stochastic model proposed by Rezaeian and Der Kiureghian [31], hereafter referred to as the reference model, offers a simple mathematical formulation based on the time modulation of a filtered Gaussian white noise process. The model requires only a small number of physically meaningful parameters and can efficiently reproduce key characteristics of recorded earthquake motions. For a given seismic event, model parameters are calibrated by matching observed cumulative energy, cumulative counts of zero-crossing, and positive-minima and negative-maxima of recordings, which also serve as validation metrics for the simulated records [8].

The parameterization of the reference model was originally designed to represent far-field ground motions characterized by a single dominant phase of energy arrival. Consequently, the model has limited ability to reproduce the low-frequency content associated with pulse-like and deep-basin ground motions, as well as temporal nonstationarities arising from multiple strong motion phases, without additional post-processing or combining with deterministic models. These shortcomings were recognized in previous studies, where the adoption of alternative filters and parameterizations was suggested as a potential avenue for future development.

This chapter presents an enhanced stochastic simulation framework that extends the applicability of the reference model while preserving its simplicity and computational efficiency. The proposed developments consist of four principal modifications:

1. Reordering the filtering operation relative to time modulation to avoid distortion of very low-frequency content.
2. Eliminating the need for post-simulation filtering and the associated correction factors used to compensate for energy bias.
3. Introducing a new broadband filtering formulation capable of representing very low-frequency energy, thereby implicitly accounting for features commonly associated with rupture directivity pulses and long-period basin amplification within a purely stochastic framework.
4. Introducing a new time-modulating function capable of representing the arrival of seismic energy through multiple strong motion phases.

The proposed framework is evaluated using a diverse set of recordings from the 6 February 2023 Kahramanmaraş, Türkiye earthquake sequence together with a pulse-like subset of the NGA-West2 database. Model performance is assessed using goodness-of-fit measures [79], empirical cumulative distributions of validation-metric errors [8], and inter-period correlations [37].

While deterministic forward-directivity pulse models remain more suitable when detailed rupture and site information are available, the proposed stochastic framework provides a simpler alternative for simulating a broad range of ground motion characteristics when seismological information is limited or when representing record-to-record variability is a primary objective. The resulting framework extends the applicability of site-based stochastic simulation to a wider types of earthquake ground motions while preserving the computational efficiency required for routine engineering applications.

2.2. Selected Datasets

To simulate strong ground motions from the February 6, 2023, Kahramanmaraş, Türkiye, earthquake (M_w = 7.8), hereafter referred to as the Kahramanmaraş earthquake, a dataset of recorded motions is selected with Joyner-Boore distances (R_{JB}) less than 80 km from the pan-European strong motion (ESM) database [80]. Figure 2.1 shows the frequency distribution of the 41 selected recording pairs (82 components in the as-recorded directions) with respect to R_{JB} and the averaged shear wave velocity at the top 30 m of soil (V_{S30}). The selected records encompass a wide range of source-to-site distances and soil conditions. Wu et al. [81] identified 18 pairs of these recordings as pulse-like motions, using the pulse index value at the orientation of the largest pulse determined through Baker's algorithm [82]. Figure 2.2 shows a scatter plot of V_{S30} versus R_{JB}, distinguishing pulse-like and non-pulse-like motions, along with the period of the largest pulse for the identified pulse-like motions. Four sample time-series in the north-south (NS) and east-west (EW) directions are shown in Figure 2.3, showing a diverse set of characteristics, including pulse-like, non-pulse-like, single, and double strong phase motions at different source-to-site rupture distances (R_{rup}). R_{rup} is used to properly distinguish the spatial proximity of near-field stations, thereby avoiding the identical zero-distance values that R_{JB} would assign to sites located directly above the fault.

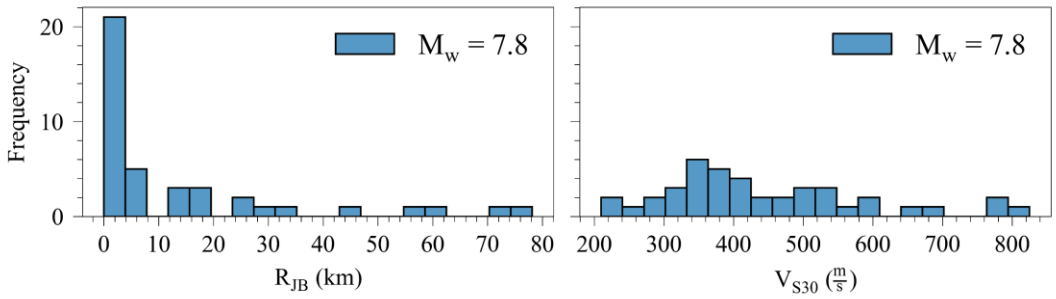


Figure 2.1. Frequency distribution of the selected ground motions from Kahramanmaraş, Türkiye, earthquake with moment magnitude (M_w) 7.8, with respect to Joyner-Boore distance (R_{JB}) and averaged shear wave velocity at the top 30 m of soil (V_{S30}).

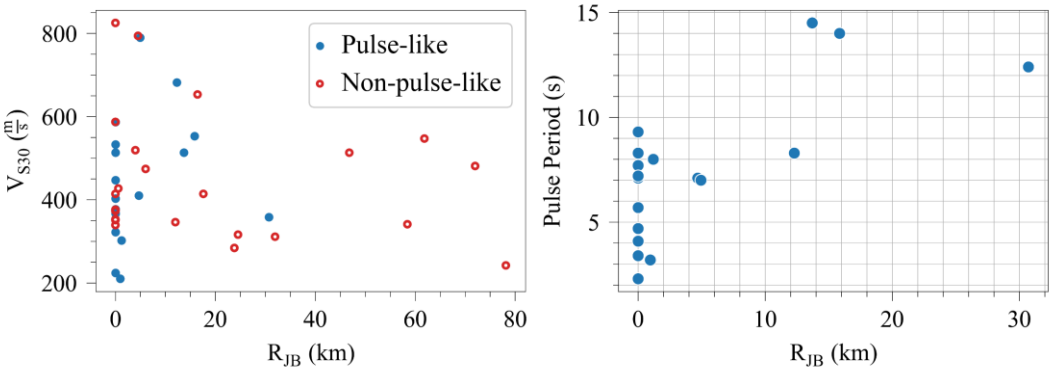


Figure 2.2. Scatter plot of V_{S30} versus R_{JB} for the Kahramanmaraş, Türkiye, earthquake dataset [80], distinguishing pulse-like and non-pulse-like motions, along with the pulse period values for the identified pulse-like motions.

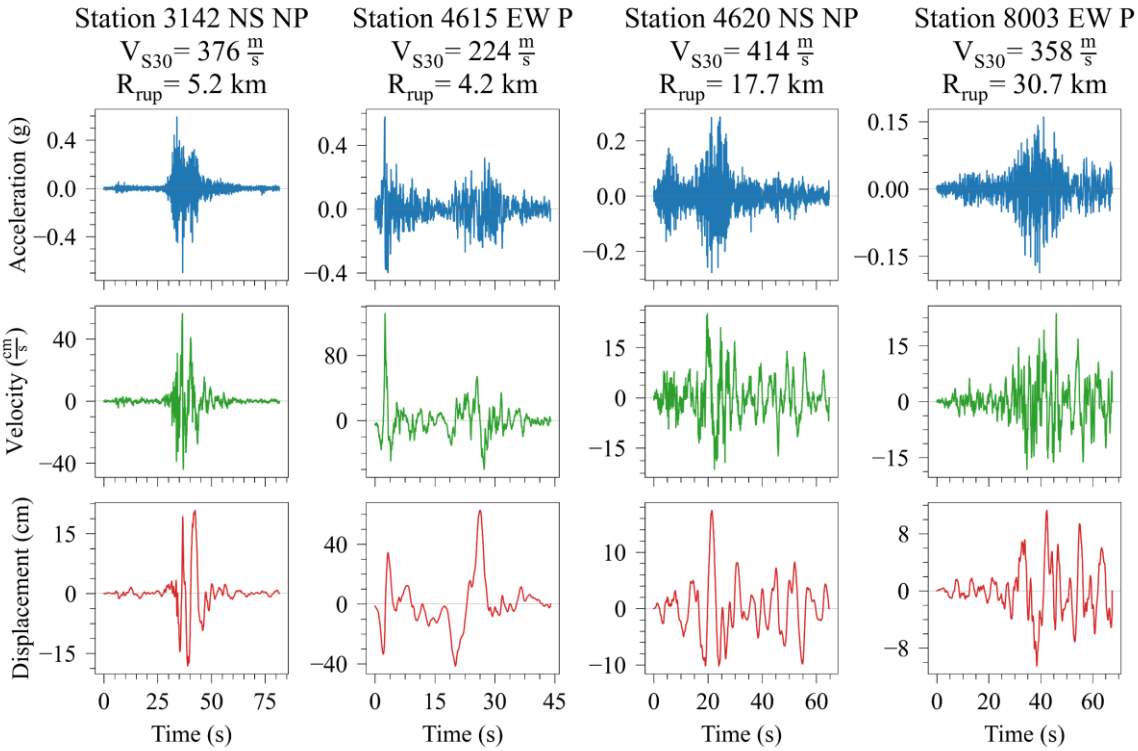


Figure 2.3. Sample ground motion time-series from the Kahramanmaraş, Türkiye, earthquake dataset, at various V_{S30}, source-to-site rupture distances (R_{rup}), showing pulse-like (P), non-pulse-like (NP), single (left and right panels), and double strong phase motions (mid panels).

To assess the ability of the improved model to accurately represent low-frequency pulse-like ground motions for a range of earthquake magnitudes, a subset of the NGA-West2 database [83] is also selected. This subset includes 97 recording pairs (194 components) of pulse-like motions with R_{JB} less than 10 km, selected without additional assumptions. Figure 2.4 shows the frequency distribution of the selected motions across R_{JB}, V_{S30}, and M_w, and Figure 2.5 shows a scatter plot of V_{S30} versus R_{JB}, along with estimated values of pulse periods for each motion as calculated by Shahi and Baker [84] and reported in the NGA-West2 database.

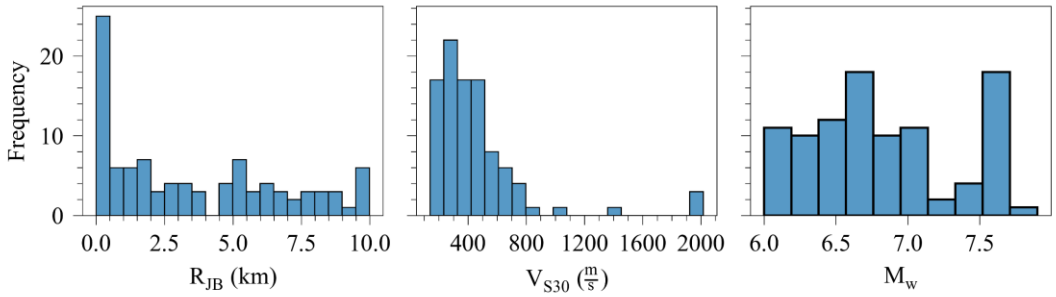


Figure 2.4. Frequency distribution of the selected ground motions from the NGA-West2 dataset [83], with respect to R_{JB}, V_{S30}, and M_w.

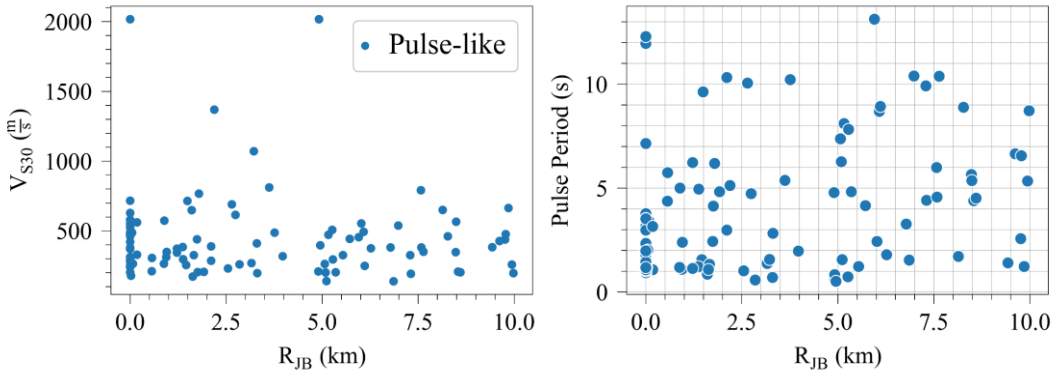


Figure 2.5. Scatter plot of V_{S30} versus R_{JB} for the selected pulse-like NGA-West2 dataset [83], along with the pulse period values of the motions.

The combined Kahramanmaraş earthquake and NGA-West2 datasets result in a total of 276 representative pairs of horizontal ground motion components, sourced from various regions and earthquakes. Information on the selected records from the ESM (https://esm-db.eu) and NGA-West2 (https://ngawest2.berkeley.edu/site) databases is summarized in Tables A1 and A2 of the Appendix, respectively.

The four accelerograms, shown in Table 2.1, are selected for illustrative purposes and discussions in this chapter. These example accelerograms include the non-pulse-like component 90 of the Northridge-01 1994 (United States) earthquake recorded at the 116th Street School station with record sequence number (RSN) of NGA RSN 984, the pulse-like component 0 of the Imperial Valley-06 1979 (United States) earthquake recorded at El Centro-Meloland Geotechnical Array station (NGA RSN 171), the pulse-like horizontal east-west component of the L'Aquila 2009 (Italy) earthquake recorded at station L'Aquila-V.Aterno-F.Aterno (NGA RSN 4482), and the pulse-like horizontal east-west component of the Kahramanmaraş 2023 (Türkiye) earthquake recorded at station 4615 (ESM ID INT-20230206-0000008). The latter two accelerograms exhibit double strong motion phases. In this chapter, an identifier (ID) is assigned to each target recorded ground motion for ease of reference, as shown in Table 2.1.

Table 2.1. Seismological characteristics of example target accelerograms, including moment magnitude (M_w), Joyner-Boore distance (R_{JB}), Rupture distance (R_{rup}), and averaged shear wave velocity at the top 30 m of soil (V_{S30}).

ID	NGA RSN / ESM ID	Event	M_w	Mechanism	R_{JB} (km)	R_{rup} (km)	V_{S30} ($\frac{m}{s}$)
NR	984	Northridge	6.69	Reverse	36.39	41.17	301
IV	171	Imperial Valley	6.53	Strike-slip	0.07	0.07	264
LA	4482	L'Aquila	6.30	Normal	0.00	6.55	552
KM	INT-20230206-0000008	Kahramanmaraş	7.80	Strike-slip	0.00	4.20	224

2.3. The Stochastic Ground Motion Model

2.3.1. The Reference Model

This chapter builds upon the site-based stochastic model developed by Rezaeian and Der Kiureghian [31]. This reference model accounts for both the temporal and spectral nonstationarities of earthquake ground motion time-series. One of the key benefits of this model is the ease of parameter estimation, achieved by separating the temporal and spectral nonstationary features of the stochastic process. The ground acceleration process $\ddot{x}(t)$ is obtained by time-modulating a normalized filtered white noise process using an evolutionary (i.e., time-varying) filter. In the continuous form, the model is defined as:

$$\ddot{x}(t) = q(t,\alpha)\left\{\frac{1}{\sigma_h(t)}\int_{-\infty}^{t} h\big(t-\tau,\lambda(\tau)\big)w(\tau)d\tau\right\} \quad 2.1$$

where $q(t,\alpha)$ is the time-modulating function with parameters in vector α, $w(\tau)$ is the white noise process, $h\big(t-\tau,\lambda(\tau)\big)$ is the shifted filter with time-varying parameters in vector $\lambda(\tau)$, and $\sigma_h^2(t) = \int_{-\infty}^{t} h^2\big(t-\tau,\lambda(\tau)\big)d\tau$ is the variance of the integral process. Normalization by $\sigma_h(t)$ results in a unit variance process denoted by the term inside the curved brackets. Thus, $q(t,\alpha)$ equals the standard deviation of the resulting process $\ddot{x}(t)$. In this formulation, the modulating function $q(t,\alpha)$ describes the temporal characteristics of the process, whereas the evolutionary filter defines the spectral characteristics. Rezaeian and Der Kiureghian [31,85] used modified versions of the piecewise and Gamma modulating functions, capable of considering a single strong motion phase [86,87]. For the evolutionary filter, the impulse response function (IRF) of the pseudo-acceleration response of an underdamped single degree of freedom (SDoF) linear system was used, which is characterized by a linearly time-varying predominant frequency and a damping ratio. This approach assumes that the bandwidth is centered around the predominant frequency, which is adopted by most site-based stochastic models for simplicity (e.g., [40,85]). Additionally, a critically damped second-order oscillator was used as a high-pass filter to post-process the time-series and ensure zero residual velocity and displacement. The post-processed acceleration record, denoted by $\ddot{z}(t)$, was obtained from the solution of the differential equation:

$$\ddot{z}(t) + 2\omega_c\dot{z}(t) + \omega_c^2 z(t) = \ddot{x}(t) \quad 2.2$$

where ω_c is the low-cut frequency of the filter, and $\ddot{x}(t)$ is the acceleration process defined in Equation 2.1.

The model formulation in Equation 2.1 and the corresponding high-pass filter in Equation 2.2 have served as the basis for the development of several improved nonstationary site-based stochastic models in the literature. These models have primarily aimed to broaden the applicability range of the model by enhancing its low-frequency content representation either by incorporating a deterministic forward directivity velocity pulse model or by refining the filter through sequential filtering techniques (e.g., [40,41,49]). Moreover, the evolutionary frequency content of a ground motion time-series is affected by several factors, including the characteristics of the earthquake source, path, and site. These intricate nonstationary processes demonstrate multiple peak frequencies in their evolutionary PSDs. To better characterize this spectral nonstationarity, several studies have assumed two or three peak frequencies and corresponding bandwidths at the expense of additional parameters and complexity [41,45,49]. However, direct identification of multiple evolutionary peak frequencies is not straightforward and often requires nonstationary spectral estimation techniques such as short-time Fourier transform.

2.3.2. The Limitations

The reference model in Equation 2.1, with the application of the high-pass filter in Equation 2.2, exhibits two main limitations. First, there could be a total energy deficit in the final process due to the high-pass filtering, and although this bias was negligible for the applicability range of the original records considered by Rezaeian and Der Kiureghian [31], it could be noticeable for records that are near-fault or on deep basins and exhibit lower-frequency contents. Although the residual velocity and displacement are removed through a stationary high-pass filter, this post-processing step can eliminate a part of the low-frequency contents and the corresponding energy from the simulations. Thus, the final process can systematically underestimate the total energy with respect to the initial process. In the validation studies done by Rezaeian and Der Kiureghian [48], such underestimations were considered nonsignificant for the selected set of strong far-field recorded ground motions. However, they may be of considerable interest in ground motions where a substantial portion of the energy comes from low-frequency contents, such as those observed in some of the records in the Kahramanmaraş earthquake.

Several studies have incorporated a stationary high-pass filter as a part of the main filter function within the reference model [41,49] or an evolutionary power spectral-based model [45]. Although this inclusion may alleviate excessive low-frequency content in the final process, several challenges persist. Firstly, determining the optimal high-pass frequency parameter remains ambiguous, often requiring iterative adjustments to the parameter to achieve realistic velocity and displacement time-series [31,45], which has some degree of subjectivity. In a recent study [88], this stationary high-pass corner frequency was optimized by matching the long-period ($T \geq 1$ s) linear acceleration response spectrum of synthetic ground motions to that of each target record. Secondly, the implementation of a stationary high-pass filter is susceptible to generating undesired response amplitudes near its frequency parameter due to the cumulative effect of response contributions in the integral term in Equation 2.1. Consequently, a high-pass filter that attenuates frequencies below a stationary corner frequency, uniformly across all time instances, may be inadequate for simulating ground motions in which an important part of the nonstationary frequency content lies within the low-frequency range, such as in near-fault pulse-like motions and motions with deep basin effects.

As the second limitation, time-modulating after filtering a process, as highlighted by Safak and Boore [89], distorts the low-frequency content in the Fourier amplitude spectrum (FAS) of the process. This latter limitation indicates that models based on Equation 2.1, despite incorporating a stationary high-pass filter, could still require an additional post-simulation high-pass filtering. Consequently, this results in an inherent bias in the total energy, requiring a post-simulation energy correction factor to address the induced bias as described in [40]. Similarly, site-based stochastic models are typically fitted to target records based on criteria such as the rates of zero-level crossings and counts of local extrema. However, post-simulation high-pass filtering can introduce bias, causing the simulations to deviate from the original fitting criteria.

The aforementioned limitations restrict the application of the reference model to only far-field ground motions and motions without the presence of deep basin effects, in which low-frequency contents do not contribute to a substantial portion of the total energy. To broaden the applicability range of the reference model to near-fault pulse-like motions, previous studies have used a deterministic forward directivity velocity pulse model [40,49]. This approach involves several steps to first identify and extract the largest pulse using a wavelet-based method, as outlined in Baker's algorithm [82], and then a forward directivity velocity pulse model would be fitted to the extracted pulse in the velocity domain. The derivative of this model is then combined with a stochastic model of the residual motion, tailoring it to cases of forward directivity velocity pulses.

2.3.3. The Proposed Improved Stochastic Model

The formulation of the reference model is modified by changing the order of time-modulation and filtering. The proposed modification is based on band-pass filtering of a time-modulated Gaussian white noise process. The band-pass filter is selected based on the response of a linear time-variant (LTV) SDoF system. Following the same terminology as the reference model, the IRF of the LTV filter is defined as $\mathrm{h}(\mathrm{t},\lambda(\tau))$, where $\lambda(\tau)$ indicates the vector of time-varying parameters. The filter is assumed to be causal: $\mathrm{h}\big(\mathrm{t},\lambda(\tau)\big)=0\ \text{for}\ \mathrm{t}<0$, stable: $\int_{-\infty}^{\infty}\mathrm{h}\big(\mathrm{t},\lambda(\tau)\big)\mathrm{dt}<\infty$, and at least twice differentiable. The time domain representation of the improved site-based stochastic model in the continuous form is as follows:

$$\ddot{\mathrm{x}}(\mathrm{t})=\int_{-\infty}^{\infty}\mathrm{q}(\tau,\alpha)\mathrm{w}(\tau)\frac{\delta(\mathrm{t}-\tau)*\mathrm{h}\big(\mathrm{t},\lambda(\tau)\big)}{\gamma_{\mathrm{h}}(\tau)}\mathrm{d}\tau \qquad 2.3$$

where $\ddot{\mathrm{x}}(\mathrm{t})$, $\mathrm{q}(\tau,\alpha)$, and $\mathrm{w}(\tau)$ are the same as those in the reference model, $\delta(\mathrm{t}-\tau)$ is a shifted Dirac delta function convolved with $\mathrm{h}(\mathrm{t},\lambda(\tau))$ which represents a band-pass filter as a function of time (t), and $\gamma_{\mathrm{h}}^{2}(\tau)=\int_{-\infty}^{\infty}\mathrm{h}^{2}\big(\mathrm{t}-\tau,\lambda(\tau)\big)\mathrm{dt}$ is the energy normalization function of the filter. This normalization ensures that for each instance of τ, the response of the normalized filter has a unit of energy over time. Therefore, the modulating function solely controls the distribution of energy over time, controlling the temporal nonstationarity of the stochastic model (refer to Equations A1 and A2 in the Appendix). Meanwhile, the normalized filter function at each instance of τ adjusts the distribution of energy across frequencies, controlling the spectral nonstationarity of the process. Therefore, the nonstationarity terms continue to be defined separately, preserving the convenient identification and interpretation of the model parameters. The evolutionary band-pass filter will account for a broad frequency bandwidth and eliminate the need for post-simulation high-pass filtering. In other words, the frequency content is characterized by an evolutionary bandwidth, delimited by a lower and an upper dominant frequency, which is anticipated to encompass the primary frequencies of interest. Therefore, the total energy of the model is always controlled by $\mathrm{q}(\mathrm{t},\alpha)$ without any systematic bias in the total energy of the simulated process, eliminating the need for further correction factors.

It is important to note that the term inside the integral in Equation 2.3 is a stationary Gaussian process at each instance of τ and uncorrelated from other instances. Thus, the convolution operation in time can be transformed into a simple multiplication in the frequency domain using the corresponding frequency response function (FRF) of the filter. Based on the linearity property of the Fourier transform and Parseval's theorem (refer to Equations A1 and A2 in the Appendix), one can show that:

$$\ddot{\mathrm{x}}(\mathrm{t})=\mathcal{F}^{-1}(\ddot{\mathrm{x}}(\bar{\omega}))=\mathcal{F}^{-1}\left(\int_{-\infty}^{\infty}\mathrm{q}(\tau,\alpha)\mathrm{w}(\tau)\frac{e^{-\mathrm{i}\bar{\omega}\tau}\mathrm{H}(\bar{\omega},\lambda(\tau))}{\gamma_{\mathrm{H}}(\tau)}\,\mathrm{d}\tau\right) \qquad 2.4$$

where $\mathrm{H}(\bar{\omega},\lambda(\tau))$ is the FRF of the filter as a function of frequency ($\bar{\omega}$), $\gamma_{\mathrm{H}}^{2}(\tau)=\int_{-\infty}^{+\infty}\left|\mathrm{H}\big(\bar{\omega},\lambda(\tau)\big)\right|^{2}\mathrm{d}\bar{\omega}$ is the equivalent energy normalization function of the filter in the frequency domain, and $\ddot{\mathrm{x}}(\bar{\omega})$, defined by the term inside parentheses, is the model representation in the frequency domain. It is noteworthy that the term inside the integral in Equation 2.4 can be considered as the time-frequency representation of the model at each instance of τ. Figure 2.6 illustrates a schematic representation of the improved site-based stochastic model in both time and frequency domains.

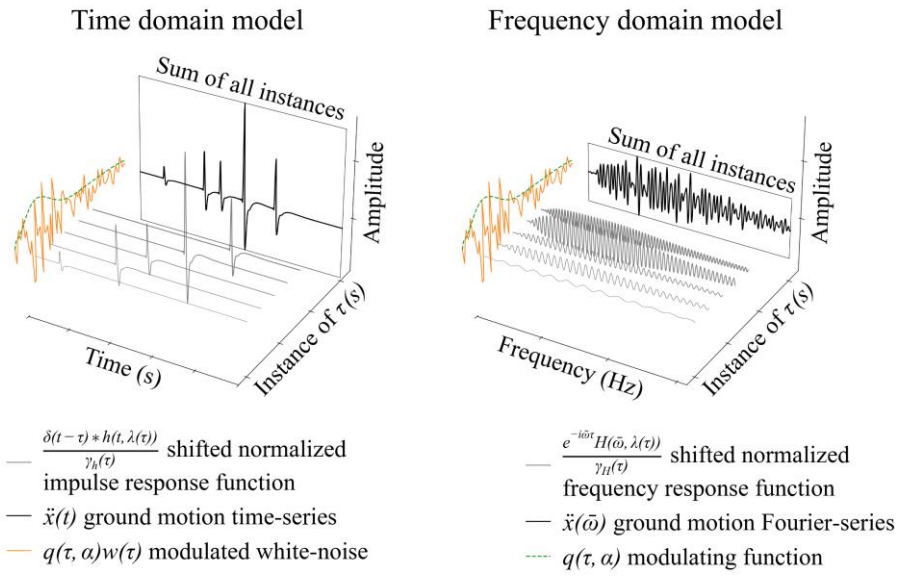


Figure 2.6. Schematic representation of the improved stochastic model in the time and frequency domains.

2.3.3.1. The Proposed Filter Function

For the filter function, the FRF of the filter $\mathrm{H}\left(\bar{\omega},\lambda(\tau)\right)$ is used instead of its IRF $\mathrm{h}(\mathrm{t},\lambda(\tau))$ to leverage the benefits of the frequency domain over the time domain for two reasons. Firstly, the time domain convolutions are simplified to mere multiplications in the frequency domain, making the computations more straightforward. Secondly, the form of the IRF of an SDoF system can vary depending on whether it is under-, over-, or critically-damped. This requires modification of the IRF's form to account for the appropriate damping ratio. In contrast, the FRF of an SDoF system maintains the same fundamental form regardless of the damping ratio, resulting in a stable formulation for determining its response. The proposed band-pass filter is constructed by cascading the displacement and acceleration IRFs of an LTV SDoF system. The resulting filter in the time domain is expressed as follows:

$$\mathrm{h}(\mathrm{t},\lambda(\tau)) = \mathrm{h_l}(\mathrm{t},\lambda_\mathrm{l}(\tau)) * \mathrm{h_u}(\mathrm{t},\lambda_\mathrm{u}(\tau)) \tag{2.5}$$

$$\mathrm{h_l}(\mathrm{t},\lambda_\mathrm{l}(\tau)) = \frac{\mathrm{d}^2}{\mathrm{dt}^2}\left[\mathrm{h_u}\left(\mathrm{t},\lambda_\mathrm{l}(\tau)\right)\right] \tag{2.6}$$

where subscripts l and u indicate association with the lower and upper dominant frequencies, respectively. Here $\mathrm{h_u}(\mathrm{t},\lambda(\tau))$ is the displacement IRF, expressed as follows:

$$\mathrm{h_u}(\mathrm{t},\lambda(\tau)) = \frac{1}{\omega(\tau)\sqrt{1-\zeta^2(\tau)}}\, e^{-\zeta(\tau)\omega(\tau)\mathrm{t}} \sin\left(\omega(\tau)\sqrt{1-\zeta^2(\tau)}\,\mathrm{t}\right) \tag{2.7}$$

where $\lambda(\tau) = [\omega(\tau), \zeta(\tau)]$ is the set of filter parameters corresponding to its natural frequency and damping ratio, respectively. In the frequency domain, the corresponding FRF can be expressed as:

$$\mathrm{H}\left(\bar{\omega},\lambda(\tau)\right) = \mathrm{H_l}\left(\bar{\omega},\lambda_\mathrm{l}(\tau)\right)\mathrm{H_u}\left(\bar{\omega},\lambda_\mathrm{u}(\tau)\right) \tag{2.8}$$

$$\mathrm{H_l}\left(\bar{\omega},\lambda_\mathrm{l}(\tau)\right) = \frac{-\bar{\omega}^2}{\omega_\mathrm{l}^2(\tau) - \bar{\omega}^2 + \mathrm{i}2\zeta_\mathrm{l}(\tau)\omega_\mathrm{l}(\tau)\bar{\omega}} \tag{2.9}$$

$$\mathrm{H_u}\left(\bar{\omega},\lambda_\mathrm{u}(\tau)\right) = \frac{1}{\omega_\mathrm{u}^2(\tau) - \bar{\omega}^2 + \mathrm{i}2\zeta_\mathrm{u}(\tau)\omega_\mathrm{u}(\tau)\bar{\omega}} \tag{2.10}$$

Here, $\mathrm{H_l}\left(\bar{\omega},\lambda_\mathrm{l}(\tau)\right)$ and $\mathrm{H_u}\left(\bar{\omega},\lambda_\mathrm{u}(\tau)\right)$ control low to intermediate and intermediate to high frequency content, respectively, and eliminate the zero-frequency amplitude. The proposed filter offers a simpler functional form and requires fewer parameters than existing filters [45,49]. Moreover, it ensures consistent behavior for ζ_l and ζ_u such that identical values for these parameters yield equal filter response

amplitudes at ω_l and ω_u. This feature is important because ζ_l and ζ_u are expected to respectively control the bandwidth from low to intermediate and intermediate to high frequencies, thereby associating filter parameters to characteristics of a ground motion time-series.

The functional forms of the filter parameters $\omega_l(\tau), \omega_u(\tau), \zeta_l(\tau), \zeta_u(\tau)$ depend on the time variation of the frequency content of an earthquake ground motion record. For simplicity, a linear function is considered in this chapter as below:

$$p(\tau) = p_0 - \frac{p_0 - p_n}{D}\tau \qquad 2.11$$

where $p(\tau)$ represents each of the filter parameters (i.e., $\omega_l(\tau), \omega_u(\tau), \zeta_l(\tau), \zeta_u(\tau)$), D is the total duration of motion, p_0 and p_n are the initial and final filter parameters, respectively.

2.3.3.2. The Proposed Time-Modulating Function

Existing time-modulating functions include the piecewise function [86,90], the double-exponential function [91], and the Gamma function [87]. Stafford [34] proposed a modulating function based on the Lognormal distribution, which models the energy build-up in ground motion time-series. These parameterized time-modulating functions describe the arrival of energy in a single strong phase, preceded by an energy build-up and followed by a decay, which may not necessarily reach zero at the end of the acceleration process. Consequently, for accelerograms characterized by the arrival of energy in multiple strong phases, these functions require adjustments. Figure 2.7 illustrates an example of such ground motions, featuring the Kahramanmaraş (KM) accelerogram (refer to Table 2.1) along with a corresponding fitted Gamma function as used in [85]. Notably, the fitted Gamma function is unable to capture the realistic arrival of energy.

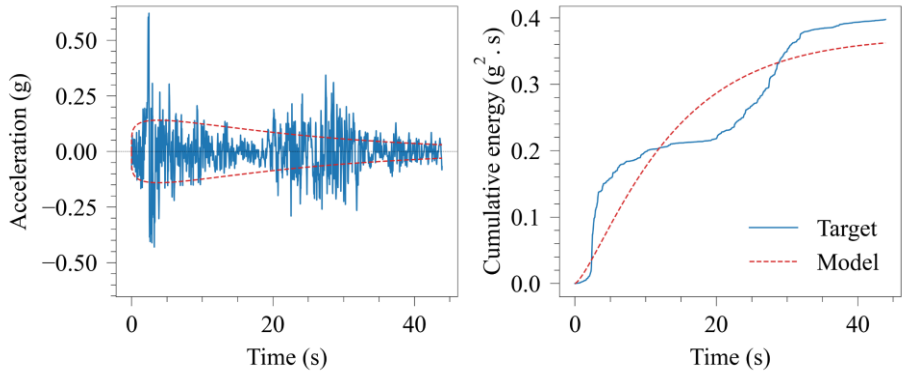


Figure 2.7. The Kahramanmaraş accelerogram with multiple strong phases, along with the fitted Gamma function and their cumulative energy.

Moreover, existing time-modulating functions rely on mathematical parameters that often lack physical interpretation. One way to relate these parameters to the seismological characteristics of a scenario earthquake is through empirically developed predictive models [34,43,85]. Modulating functions often require adjustments to account for various shapes of ground motion time-series, such as near-fault pulse-like accelerograms, by introducing additional parameters in the function (e.g., [40]). Numerical interpolation methods like monotonic cubic Hermite splines can require a varying number of input parameters depending on the target motion and desired accuracy. Broccardo and Dabaghi [92] recommended using seven interpolation points to model the modulating function. These numerical methods may necessitate supplementary post-processing to achieve a smooth modulating function and circumvent issues like overshooting (e.g., a local abrupt jump), particularly when neighboring interpolation points are spaced very closely. This can be challenging for recorded motions with rapid energy arrivals, requiring a choice of interpolation points based on the specific characteristics of the motion.

To overcome the limitations of existing time-modulating functions, concave Beta distributions are used to describe the energy build-up in ground motions. Let $a(t)$ be an accelerogram with its total expected energy defined as $E_t = \int_0^D a^2(t)dt$, arriving in a single strong phase with a total recorded duration of D. A basic Beta time-modulating function can be proposed as below:

$$q(t, E_t, D, c, p) = \sqrt{E_t . \frac{t^{cp}\ (D-t)^{c(1-p)}}{\beta\big(1+cp, 1+c(1-p)\big)\ D^{1+c}}} \qquad 2.12$$

where p is the ratio of the time of peak amplitude to the total duration (i.e., $p = \frac{\text{peak time}}{D}$), c is a dimensionless parameter that describes the distribution of energy around the peak time, and β is the Beta function. Figure 2.8 illustrates the total duration (D), total energy (E_t), and peak time (i.e., $p.D$) using an example application of the basic Beta modulating function as the model on the Northridge (NR) accelerogram (refer to Table 2.1), featuring a single strong motion phase.

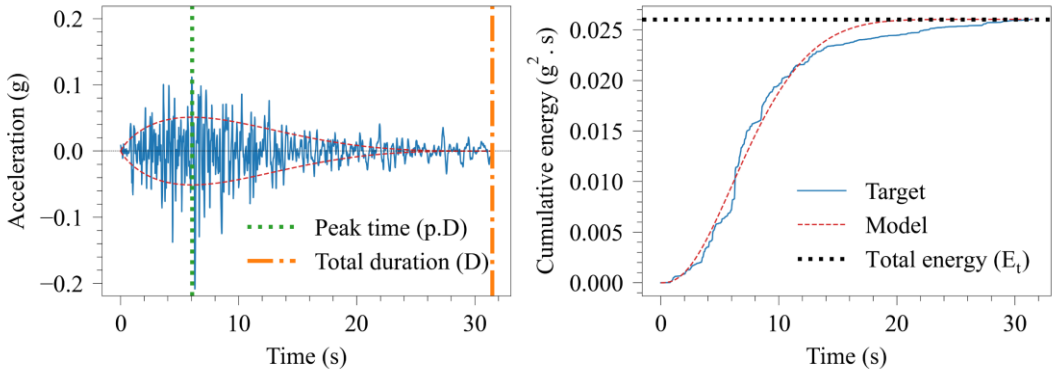


Figure 2.8. Parameters of the basic Beta function fitted to the Northridge accelerogram. E_t = 0.026037 g²s, D=31.48 s, p.D=6.04 s, c=8.65.

The arrival of energy in multiple strong phases can be replicated by a weighted sum of basic Beta time-modulating functions. The proposed Beta modulating function, which explicitly starts from and ends in zero amplitude, can be expressed as follows:

$$q(t, E_t, D, \vec{\alpha}, \vec{c}, \vec{p}) = \sqrt{E_t . \sum_{i=0}^{n} \left(\alpha_i \frac{t^{c_i p_i}\ (D-t)^{c_i(1-p_i)}}{\beta\big(1+c_i p_i, 1+c_i(1-p_i)\big)\ D^{1+c_i}} \right)} \qquad 2.13$$

where $\vec{\alpha}, \vec{c}, \vec{p}$ are vectors of size n+1, with p_i representing the i^{th} strong phase peak-time ratio, α_i denoting the ratio of energy contributed by the i^{th} strong phase to the total energy, and c_i quantifying the energy concentration around the peak time within that i^{th} strong phase. The term corresponding to $i = 0$ is considered as a baseline energy level, to capture the very low-amplitude tails of a ground motion. Therefore, 5% of the total energy (α_0= 5%) is distributed over the total duration with parameters c_0 = 2.0 and p_0 = 0.5. Setting $n = 1$ allows the modulating function to account for a single strong phase using four parameters (E_t, D, p_1, c_1). By setting $n = 2$, the proposed modulating function accounts for up to two strong phases ($i = 1, 2$) with seven parameters (E_t, D, α_1, p_1, c_1, p_2, c_2). Note that α_2 can be determined by specifying α_1 (i.e., $\alpha_2 = 1 - 0.05 - \alpha_1$). With this modulating function, adding more strong phases only requires dividing the total energy and specifying the corresponding parameters (i.e., α_i, p_i, c_i).

Therefore, the improved stochastic model is fully defined by eight parameters (ω_{l_0}, ω_{l_n}, ω_{u_0}, ω_{u_n}, ζ_{l_0}, ζ_{l_n}, ζ_{u_0}, ζ_{u_n}) that specify the filter function, and seven parameters (E_t, D, α_1, p_1, c_1, p_2, c_2) that specify the time-modulating function for up to two strong phases.

2.4. Ground Motion Frequency and Energy Evolution

2.4.1. Time-Varying Frequency Content

To characterize the predominant frequency and bandwidth, many site-based stochastic models have used the rate of zero-level up-crossings and positive-minima and negative-maxima of the acceleration process, respectively (e.g., [31,40,41,87,93]). To explore the characteristics of a ground motion time-series, mean zero crossing (MZC), mean local extrema (MLE), and mean positive-minima and negative-maxima (MPMNM) are defined as follows. MZC represents the average number of zero-level up-crossings and down-crossings, MLE denotes the average number of local minima and maxima, and MPMNM indicates the average number of local positive-minima and negative-maxima. Analysis of these three features within recorded ground motions demonstrates that the MZC of acceleration equals the MLE of velocity, and the MZC of velocity equals the MLE of displacement, which is supported by the theoretical definitions of acceleration, velocity, and displacement processes. Similarly supported by their definitions, the MPMNM of velocity is half of the difference between its MLE and MZC. Likewise, the MPMNM of displacement is half of the difference between its MLE and MZC. Figure 2.9 illustrates these relationships for the example NR ground motion (refer to Table 2.1).

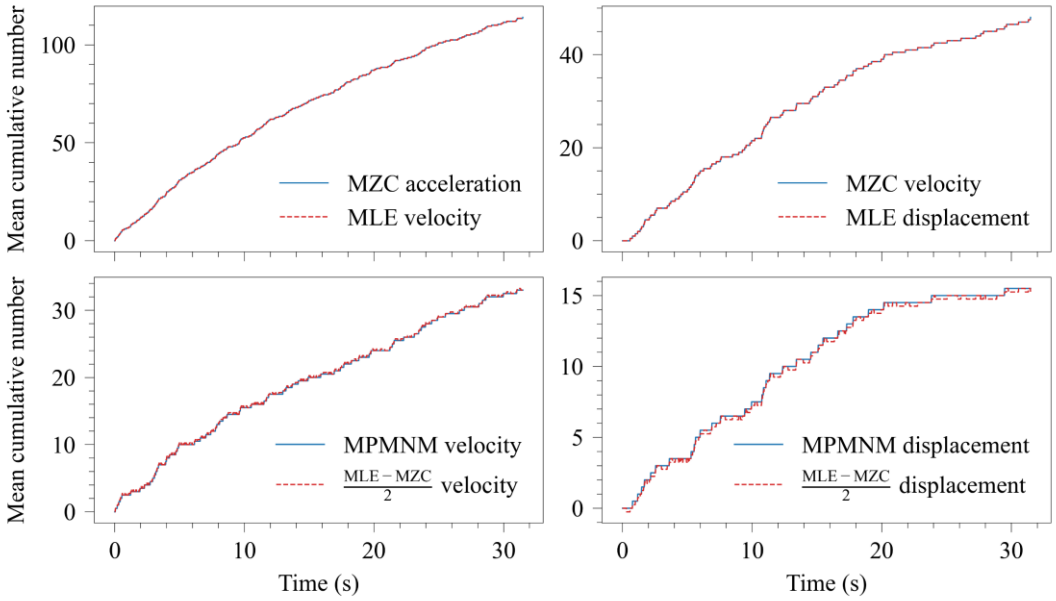


Figure 2.9. Relationships between time-series characteristics of recorded ground motions, using the Northridge accelerogram. Characteristics include mean zero crossing (MZC), mean local extrema (MLE), and mean positive-minima and negative-maxima (MPMNM).

As such, the MPMNM of a process can be replaced with the difference between the MZC of that process and its time-derivative. In other words, given that the MZC of a process (i.e., acceleration, velocity, or displacement) is related to its dominant frequencies, the MPMNM of the process is associated with the bandwidth between the dominant frequencies of that process and its time-derivative. Therefore, the MZC of acceleration, velocity, and displacement processes can be used as proxies for high, intermediate, and low dominant frequencies, respectively. Similarly, the MPMNM of the displacement and velocity processes can be used as proxies for the bandwidth between low to intermediate and intermediate to high dominant frequencies. As the MPMNM of the acceleration process acts as a proxy for the bandwidth between the acceleration and its time-derivative, it may not provide any advantages for modeling the acceleration, velocity, and displacement time-series. Consequently, it is not used as a fitting criterion. Subsequently, these features are formulated for the acceleration, velocity, and displacement processes of the stochastic model.

Let $g(t,\tau)$ be the term inside the integral in Equation 2.3. Because $g(t,\tau)$ represents a stationary Gaussian process at each instance of τ and is uncorrelated from other instances, its first time-derivative $\frac{d}{dt}g(t,\tau)$ is independent of both the process $g(t,\tau)$ and its second time-derivative $\frac{d^2}{dt^2}g(t,\tau)$ at each instance of τ [94]. However, the process and the second time-derivative are not mutually independent. Therefore, the MZC rate of acceleration ($\nu_a(\tau)$), velocity ($\nu_v(\tau)$), and displacement ($\nu_d(\tau)$) processes can be respectively simplified as [94]:

$$\nu_a(\tau) = \frac{1}{2\pi}\frac{\sigma_{\dot{g}}(\tau)}{\sigma_g(\tau)} \quad 2.14$$

$$\nu_v(\tau) = \frac{1}{2\pi}\frac{\sigma_g(\tau)}{\sigma_{\bar{g}}(\tau)} \quad 2.15$$

$$\nu_d(\tau) = \frac{1}{2\pi}\frac{\sigma_{\bar{g}}(\tau)}{\sigma_{\bar{\bar{g}}}(\tau)} \quad 2.16$$

where $\sigma_g(\tau)$, $\sigma_{\dot{g}}(\tau)$ are the standard deviation of $g(t,\tau)$ and its first time-derivative at the instance of τ, respectively. $\sigma_{\bar{g}}(\tau)$ and $\sigma_{\bar{\bar{g}}}(\tau)$ are the standard deviation of the first and second integrals of $g(t,\tau)$, respectively. Furthermore, the analytical expression for the MLE rate of acceleration ($\eta_a(\tau)$), velocity ($\eta_v(\tau)$), and displacement ($\eta_d(\tau)$) processes can be described as [94]:

$$\eta_a(\tau) = \frac{1}{2\pi}\frac{\sigma_{\ddot{g}}(\tau)}{\sigma_{\dot{g}}(\tau)} \quad 2.17$$

$$\eta_v(\tau) = \frac{1}{2\pi}\frac{\sigma_{\dot{g}}(\tau)}{\sigma_g(\tau)} \quad 2.18$$

$$\eta_d(\tau) = \frac{1}{2\pi}\frac{\sigma_g(\tau)}{\sigma_{\bar{g}}(\tau)} \quad 2.19$$

where $\sigma_{\ddot{g}}(\tau)$ is the standard deviation of the second time-derivative of the process $g(t,\tau)$. It is noteworthy that the MPMNM rate of a process (i.e., acceleration, velocity, or displacement) is also formulated as half of the difference between the MLE and MZC rate of the process using Equations 2.14 to 2.19. In the above expressions, $\nu_a(\tau) = \eta_v(\tau)$ and $\nu_v(\tau) = \eta_d(\tau)$, which are also observed numerically in recorded ground motions (refer to the example in Figure 2.9). Moreover, $\eta_a(\tau)$ is related to the first and second time-derivatives of the process $g(t,\tau)$. As discussed earlier, the inclusion of this relationship provides no benefits to the model. Therefore, it is omitted from the fitting procedures.

Equations 2.14 to 2.16 are used as the fitting criterion to describe the time-varying frequency content of the target recorded motion. As a result, the MZC of acceleration and displacement processes serve as proxies for the upper and lower dominant frequencies, respectively. To avoid redundancy, the MZC of the velocity process (alongside acceleration and displacement MZC) adequately accounts for the bandwidth of the process, implicitly capturing the MPMNM of the velocity and displacement processes.

In Equation 2.3, the term $q(\tau,\alpha)w(\tau)$ at each instance of τ has the same value for $\sigma_g(\tau)$, $\sigma_{\dot{g}}(\tau)$, $\sigma_{\ddot{g}}(\tau)$, $\sigma_{\bar{g}}(\tau)$ and $\sigma_{\bar{\bar{g}}}(\tau)$, and can be ignored while using Equations 2.14 to 2.16. This can also be interpreted physically, as scaling a process is not expected to affect the count of its zero crossings or local extrema. A simple alternative for determining the standard deviations of the process $g(t,\tau)$, its derivatives, and integrals in Equations 2.14 to 2.16 is to use the expected evolutionary PSD of the process $g(t,\tau)$. Because $g(t,\tau)$ is equivalent to the term inside the integral in Equation 2.4, the expected PSD (ϕ_E) can be expressed as follows:

$$\phi_E\left(\bar{\omega},\tau,\alpha,\lambda(\tau)\right) = q(\tau,\alpha)^2 \frac{\left|H\left(\bar{\omega},\lambda(\tau)\right)\right|^2}{\int_{-\infty}^{+\infty}\left|H\left(\bar{\omega},\lambda(\tau)\right)\right|^2 d\omega} \quad 2.20$$

Therefore, the variance of the process $g(t,\tau)$, its time-derivatives, and integrals can be expressed as follows:

$$\sigma_g^2(\tau) = \int_{-\infty}^{\infty} \phi_E(\bar{\omega},\tau,\lambda(\tau))d\bar{\omega} \quad 2.21$$

$$\sigma_{\dot{g}}^2(\tau) = \int_{-\infty}^{\infty} \bar{\omega}^{\,2}\phi_E(\bar{\omega},\tau,\lambda(\tau))d\bar{\omega} \quad 2.22$$

$$\sigma_{\int g}^2(\tau) = \int_{-\infty}^{\infty} \bar{\omega}^{\,-2}\phi_E(\bar{\omega},\tau,\lambda(\tau))d\bar{\omega} \quad 2.23$$

$$\sigma_{\iint g}^2(\tau) = \int_{-\infty}^{\infty} \bar{\omega}^{\,-4}\phi_E(\bar{\omega},\tau,\lambda(\tau))d\bar{\omega} \quad 2.24$$

Because τ is a dummy variable of time, the MZC rate of the acceleration process $\ddot{x}(t)$ and its corresponding velocity and displacement processes are essentially the same as in Equations 2.14 to 2.16 by substituting τ with t. Note that when using Equations 2.21 to 2.24 for a discrete system corresponding to a recorded accelerogram, the bound of the integral is limited to the corresponding Nyquist frequency to avoid aliasing [95].

2.4.2. Time-Varying Energy Content

Fitting to the time-varying energy content follows the same procedure used by Rezaeian and Der Kiureghian [31] but with an added number of parameters for the time-modulating function. For a ground motion time-series $a(t)$, cumulative energy (CE) can directly represent the time-varying energy content and is expressed as follows:

$$CE_a(t) = \int_0^t a^2(\tau)\, d\tau \quad 2.25$$

Similarly, the expected CE of the process $\ddot{x}(t)$ defined in Equation 2.3 or 2.4 can be formulated as follows:

$$CE_{\ddot{x}}(t) = E\left[\int_0^t \ddot{x}(\tau)^2 d\tau\right] = \int_0^t q^2(\tau, E_t, D, \vec{\alpha}, \vec{c}, \vec{p})\, d\tau \quad 2.26$$

This means the modulating function can fully and independently describe the energy content of the process.

2.5. Parameter Identification

Similar to Rezaeian and Der Kiureghian [31], the parameters of both the filter and the time-modulating function can be independently identified by matching the characteristics outlined in the previous section with those of a target accelerogram. Unlike [31], in which filter parameters were identified by matching to the MZC and MPMNM of the acceleration process, the parameters are identified here by matching to the MZC of the acceleration, velocity, and displacement processes. This adjustment to the objective functions is necessary to converge to an optimized set of model parameters given their increased number

and is more intuitive given their segregation into lower and upper limits of the dominant frequency in Equations 2.9 and 2.10.

2.5.1. Parameter Identification for the Filter Function

The filter parameters (ω_{l_0}, ω_{l_n}, ω_{u_0}, ω_{u_n}, ζ_{l_0}, ζ_{l_n}, ζ_{u_0}, ζ_{u_n}) have interrelated effects. For instance, lower damping ratios enable oscillation with specific dominant frequencies to persist in time, leading to dominant frequencies with higher amplitude and a narrower bandwidth in the proposed filter. Hence, it is reasonable to concurrently identify the filter frequencies and damping ratios. This is achieved by matching the cumulative expected MZC of the acceleration, velocity, and displacement processes of the model with those of the corresponding target motion. The squared differences between the corresponding terms are minimized as expressed below:

$$\begin{aligned}\left[\omega_{l_0}, \omega_{l_n}, \omega_{u_0}, \omega_{u_n}, \zeta_{l_0}, \zeta_{l_n}, \zeta_{u_0}, \zeta_{u_n}\right] \\ = \arg\min \left[\int_0^D \left[\int_0^t \nu_a(\tau)d\tau - N_{\nu_a}(t)\right]^2 dt + \int_0^D \left[\int_0^t \nu_v(\tau)d\tau - N_{\nu_v}(t)\right]^2 dt \right. \\ \left. + \int_0^D \left[\int_0^t \nu_d(\tau)d\tau - N_{\nu_d}(t)\right]^2 dt\right]\end{aligned} \quad 2.27$$

where $N_{\nu_a}(t)$, $N_{\nu_v}(t)$, and $N_{\nu_d}(t)$ are the cumulative MZC of the acceleration, velocity, and displacement time-series of the target motion, respectively. The SciPy library in Python is used to identify model parameters. One advantage of the proposed filter over existing filters (e.g., [41,45]) is that $\omega_u(\tau)$ and $\omega_l(\tau)$ are primarily influenced by the rate of MZC of the target acceleration and displacement time-series, respectively. This underlying relation facilitates understanding the variation of these parameters from the corresponding MZC curves.

Figure 2.10 illustrates the cumulative MZC of the example target accelerograms, their velocity and displacement time-series, and the corresponding fitted models. Identified filter parameters are shown in Table 2.2. The MZC rate of the target motions (i.e., acceleration, velocity, and displacement), which is the slope of the corresponding curves in Figure 2.10, fluctuates over time for all selected accelerograms. This means that the dominant frequencies in the target motions vary with time. In the case of the Imperial Valley (IV) (refer to Table 2.1) accelerogram with a shorter rupture distance (R_{rup} = 0.07 km) and a soft soil (V_{S30} = 264 $\frac{m}{s}$), the fluctuations are more apparent than in other cases. The value of the upper dominant frequency (ω_u), which follows the acceleration MZC rate, generally exhibits a downward trend. However, it shows an upward trend in the IV case. The higher MZC in the acceleration time-series signifies the prevalence of higher frequencies. On the other hand, a reduced MZC in the displacement time-series indicates the predominance of lower frequencies. Thus, the MZC rate in each acceleration or displacement time-series is related to the corresponding upper or lower dominant frequencies, respectively. The L'Aquila (LA) accelerogram shows an elevated rate of MZC in the acceleration time-series compared to other cases. Consequently, its upper dominant frequency value surpasses that of other cases, as shown in Table 2.2. The lower dominant frequency (ω_l) corresponds to a decrease in rate. It is noteworthy that damping ratios (i.e., ζ_u, ζ_l) regulate the bandwidth to accurately capture the intermediate frequencies, as shown by the rate of MZC for velocity. To verify the adequacy of the considered MZC rates as criteria, Figure 2.11 compares the MPMNM of the target velocity and displacement time-series to those of the corresponding models. Figure 2.11 shows that the MPMNM of displacement as a proxy for low to intermediate frequencies and the MPMNM of velocity as a proxy for intermediate to high frequencies are effectively incorporated in the fitted model. Errors for various validation metrics (e.g., MZC of acceleration) can be calculated using the following expression:

$$\epsilon_M = \frac{\int_0^D |M_{Target}(t) - E[M_{Model}(t)]|dt}{\int_0^D M_{Target}(t)dt} \quad 2.28$$

where M refers to the relevant validation metric for both the target and expected model processes, and ϵ_M is the error value for that specified validation metric M. Therefore, to quantify the errors associated with the cumulative MZC of the acceleration (ϵ_{MZC_a}), velocity (ϵ_{MZC_v}), and displacement (ϵ_{MZC_d}), as well as MPMNM of the velocity (ϵ_{MPMNM_v}) and displacement (ϵ_{MPMNM_d}), Equation 2.28 is used by substituting these respective metrics for the variable M for both target and model processes. These error measures are reported in Table 2.2 for each of the example target motions. The increased error values associated with the MZC of displacement time-series stem from the staggered shape of their curves. These curves are not as smooth as those for acceleration time-series due to the reduced count of MZC, resulting in increased relative errors.

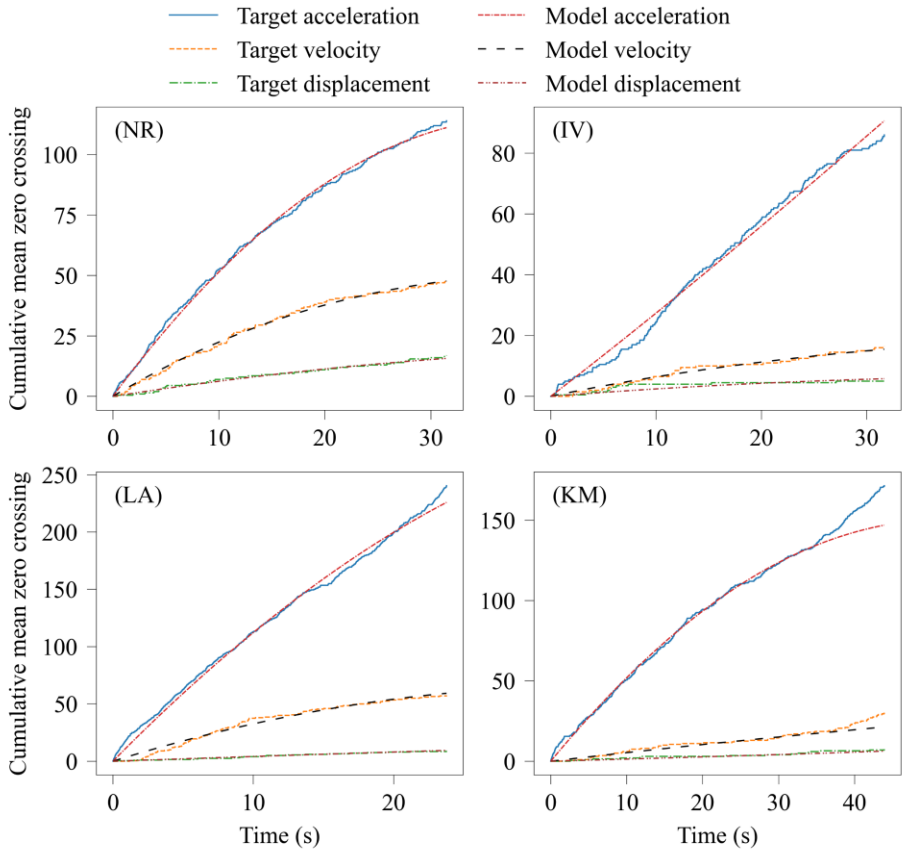


Figure 2.10. Cumulative mean zero crossings of the target acceleration, velocity, and displacement time-series, along with their corresponding fitted models. The panels correspond to Northridge (NR), Imperial Valley (IV), L'Aquila (LA), and Kahramanmaraş (KM) ground motions.

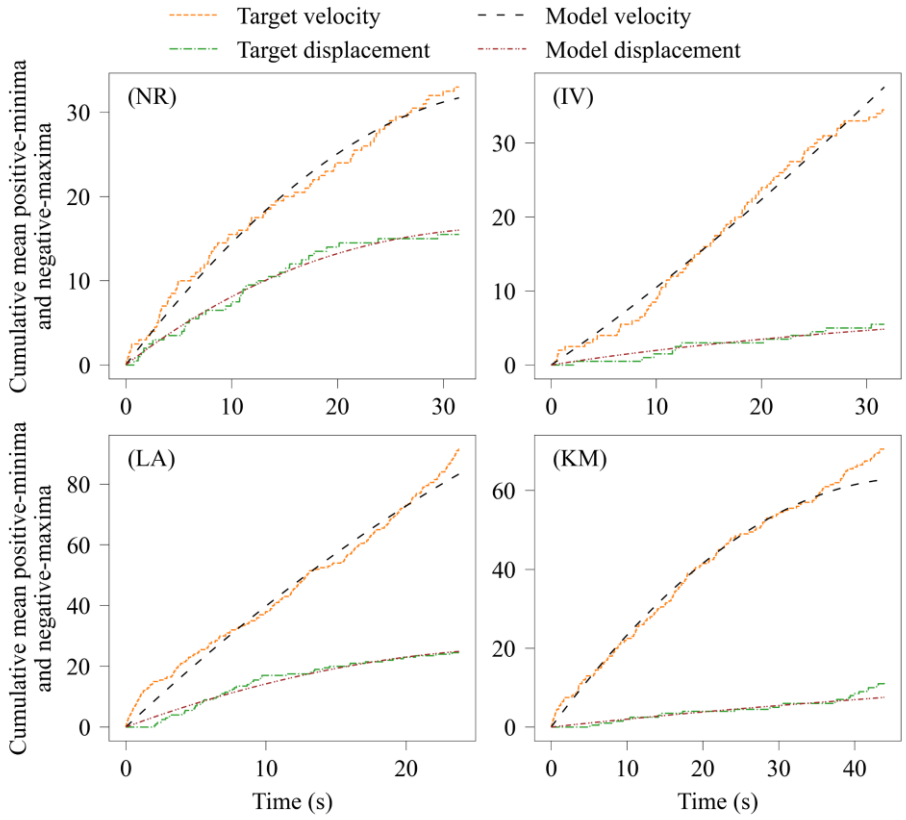


Figure 2.11. Cumulative mean positive-minima and negative-maxima of the target velocity and displacement time-series, along with their corresponding fitted models. The panels correspond to Northridge (NR), Imperial Valley (IV), L'Aquila (LA), and Kahramanmaraş (KM) ground motions.

Table 2.2. Parameters of the filter function fitted to target accelerograms.

ID	Frequency parameters (Hz)				Damping ratio parameters				Errors				
	ω_{u_0}	ω_{u_n}	ω_{l_0}	ω_{l_n}	ζ_{u_0}	ζ_{u_n}	ζ_{l_0}	ζ_{l_n}	ϵ_{MZC_a}	ϵ_{MZC_v}	ϵ_{MZC_d}	ϵ_{MPMNM_v}	ϵ_{MPMNM_d}
NR	5.88	1.21	0.69	0.32	0.50	0.52	1.00	0.36	0.02	0.03	0.05	0.04	0.04
IV	2.70	3.01	0.29	0.10	0.70	2.43	0.47	0.64	0.05	0.06	0.19	0.06	0.16
LA	12.35	6.78	0.41	0.37	0.53	0.58	1.70	0.27	0.03	0.06	0.06	0.06	0.06
KM	5.77	0.94	0.14	0.16	2.88	0.10	1.03	0.26	0.04	0.12	0.16	0.04	0.13

2.5.2. Parameter Identification for the Time-Modulating Function

The parameters of the time-modulating function (E_t, D, α_1, p_1, c_1, p_2, c_2) are identified by matching the expected cumulative energy of the process with that of the target accelerogram over the total duration. This can be done by minimizing the squared difference between the two cumulative energy terms, expressed as follows:

$$(\alpha_1, p_1, c_1, p_2, c_2) = \operatorname{argmin} \int_0^D [CE_{\ddot{x}}(t) - CE_a(t)]^2 dt \qquad 2.29$$

To ensure a unique solution for cases with two strong phases, it is assumed that the first phase precedes the second, imposing the constraint $p_1 \leq p_2$ on the parameters. For $p_1 = p_2$, a single strong phase can be selected by setting $n = 1$ in Equation 2.13. However, in simulating our selected datasets, $n = 2$ is used to maintain consistency in the results.

Recorded ground motions often exhibit leading or trailing zeros or negligible amplitudes, resulting in different durations. To avoid these tails that have a negligible contribution to the total energy, the target

motion is defined as that corresponding to 0.1% to 99.9% of the total energy of the input recorded accelerogram. Figure 2.12 illustrates the target motion and the corresponding duration for LA as an example (refer to Table 2.1).

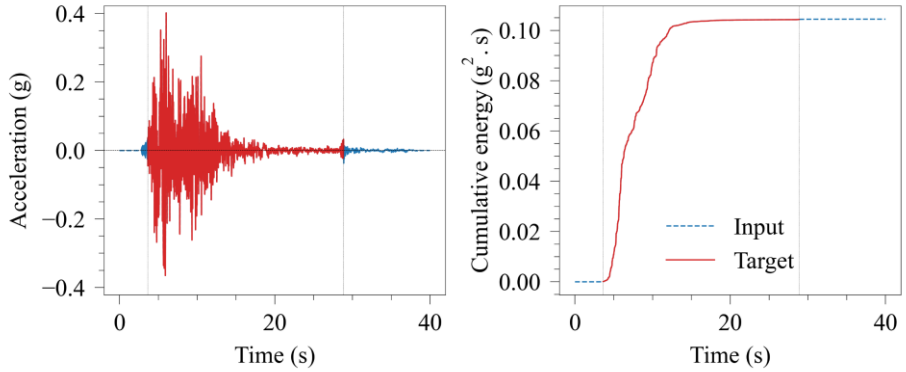


Figure 2.12. L'Aquila target motion corresponding to 0.1%–99.9% of the total energy of the input accelerogram.

Errors associated with cumulative energy are determined by substituting CE for the variable M in Equation 2.28. The identified parameters of the modulating function and the corresponding errors are shown in Table 2.3. Figure 2.13 illustrates the modulating function and cumulative energy of the model when fitting to the corresponding target accelerograms. The fit with slight error demonstrates the capability of the time-modulating function in modeling various shapes of ground motions, including pulse-like and double strong phase motions. The arrival of energy in a single strong phase is observable in NR and IV, with a more abrupt arrival in the latter (refer to Table 2.1). In NR, 76.6% of the total energy is smoothly distributed around the first peak time ($D.\,p_1 = 6.1$ s), featuring a low value for the energy concentration ($c_1 = 22.8$). In contrast, IV exhibits a higher energy concentration ($c_1 = 182.5$) around the first peak time ($D.\,p_1 = 2.3$ s) that carries 75.4% of the total energy. In the cases of LA and KM, two distinct strong phases are evident. The first phase in LA carries 60.2% of the total energy with a peak time of $D.\,p_1 = 1.9$ s. In KM, the first phase carries 49.7% of the total energy with a peak time of $D.\,p_1 = 2.6$ s and the energy concentration of $c_1 = 49.5$. As can be observed, the second strong phase with a peak time of $D.\,p_2 = 27.4$ s is less concentrated ($c_2 = 19.0$).

Table 2.3. Parameters of the modulating function fitted to target accelerograms.

ID	Modulating function parameters							Errors
	$E_t\ (g^2.s)$	$D\ (s)$	α_1	p_1	c_1	p_2	c_2	ϵ_{CE}
NR	0.026037	31.48	0.766	0.193	22.8	0.193	0.7	0.013
IV	0.056155	31.67	0.754	0.074	182.5	0.178	41.9	0.008
LA	0.104165	23.76	0.602	0.079	74.6	0.247	69.3	0.011
KM	0.341184	43.90	0.497	0.060	49.5	0.625	19.0	0.022

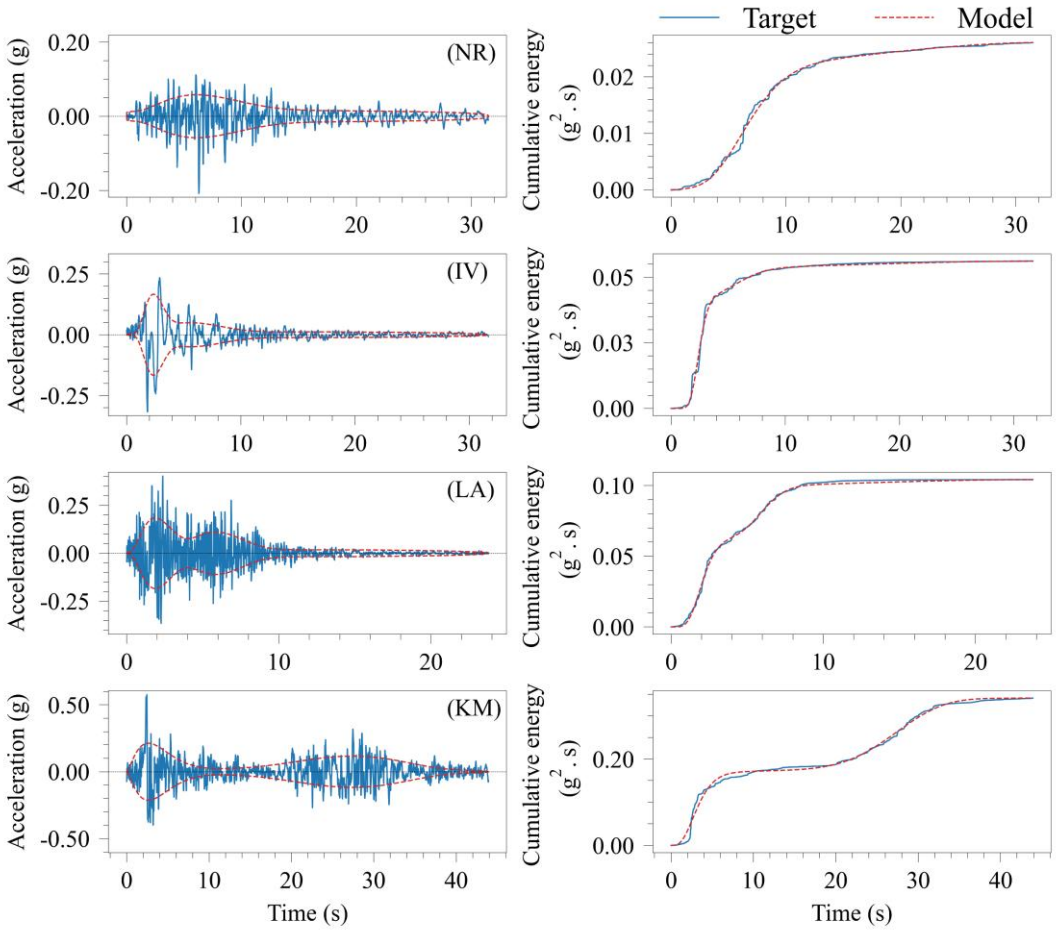


Figure 2.13. Fitted modulating function to target accelerograms and their respective cumulative energy. The panels correspond to Northridge (NR), Imperial Valley (IV), L'Aquila (LA), and Kahramanmaraş (KM) motions.

2.6. Validation

Before simulations can be used in engineering applications, it is crucial to thoroughly validate the simulation methodologies and their outcomes by assessing their effectiveness in predicting both seismological and engineering demand parameters [8,38,96]. Such validation ensures that the model accurately represents the main characteristics of recorded ground motions, thus demonstrating the reliability of the synthetic motions for engineering applications. Validation procedures in the literature are often based on characteristics that are expected to affect engineering systems, such as elastic response spectra or other ground motion validation metrics [18,37,79,97]. In this chapter, a visual comparison is first performed between the ground motion time-series, cumulative energy, Fourier amplitude, and elastic response spectra of the four example target accelerograms and those of simulations generated from the fitted stochastic model parameters described in previous sections. Next, the efficiency of the improved stochastic model is quantitatively assessed using 276 horizontal components from the selected datasets.

2.6.1. Visual Qualitative Comparisons of Target and Simulated Motions

Given the identified model parameters in the previous section, the improved stochastic model can directly simulate ground motion time-series without added deterministic components or any additional post-processing. Figure 2.14 to Figure 2.16 show the acceleration, velocity, and displacement time-series for the four example target motions listed in Table 2.1, along with two realizations for each, obtained from stochastic simulations as described in previous sections. In Figure 2.14, the stochastic simulations

resemble target accelerograms in terms of the overall waveforms, intensity levels, durations, and frequency contents. In particular, simulations of LA and KM exhibit multiple strong phases like their respective target motions. This illustrates the effectiveness of the proposed modulating function in accurately accounting for the arrival of energy in multiple strong phases. The simulated velocity time-series in Figure 2.15 are also like those of target motions, capturing the overall waveforms, pulse timings, and pulse intensities without considering additional explicit constraints on these features. For example, in IV, a velocity pulse is observed at t=2.73s with a peak ground velocity (PGV) of 72.96 $\frac{\text{cm}}{\text{s}}$. Consequently, the stochastic simulations that aim to provide possible realizations of the target motion exhibit a velocity pulse with comparable timing and intensity. Thus, the proposed filter has adequately captured the low-frequency contents, successfully representing near-fault pulse-like ground motions. The displacement time-series, illustrated in Figure 2.16, further underscores these observations, revealing analogous waveforms and intensity characteristics.

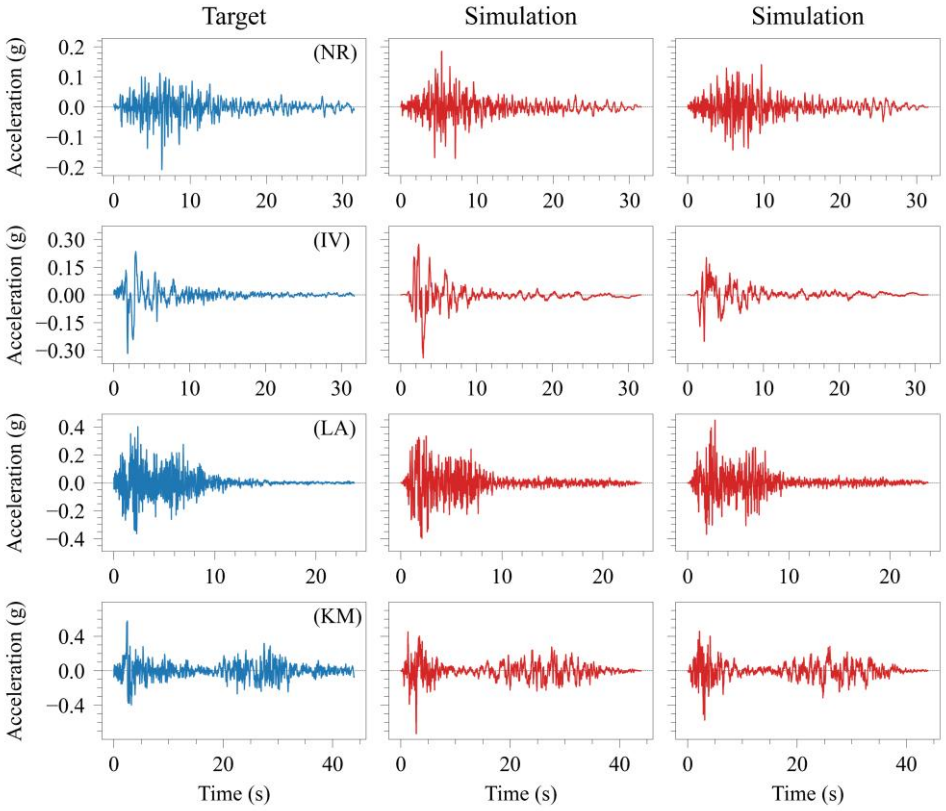


Figure 2.14. Target accelerograms and two alternative simulations using the corresponding fitted models. The panels correspond to Northridge (NR), Imperial Valley (IV), L'Aquila (LA), and Kahramanmaraş (KM) motions.

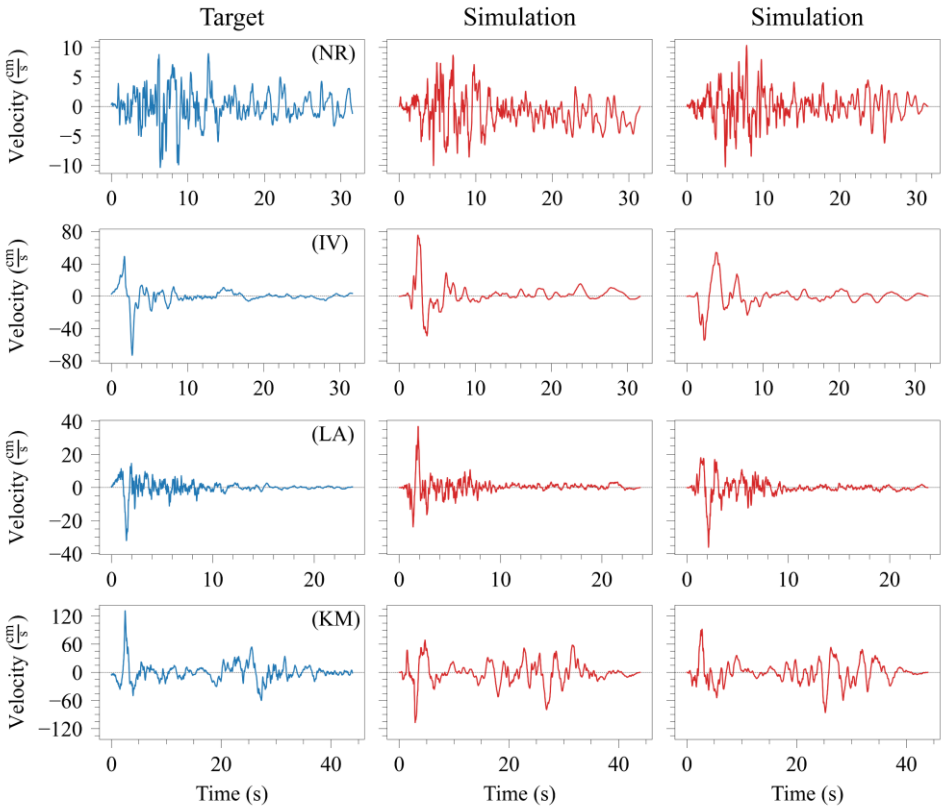


Figure 2.15. Velocity time-series and two alternative simulations using the corresponding fitted models. The panels correspond to Northridge (NR), Imperial Valley (IV), L'Aquila (LA), and Kahramanmaraş (KM) motions.

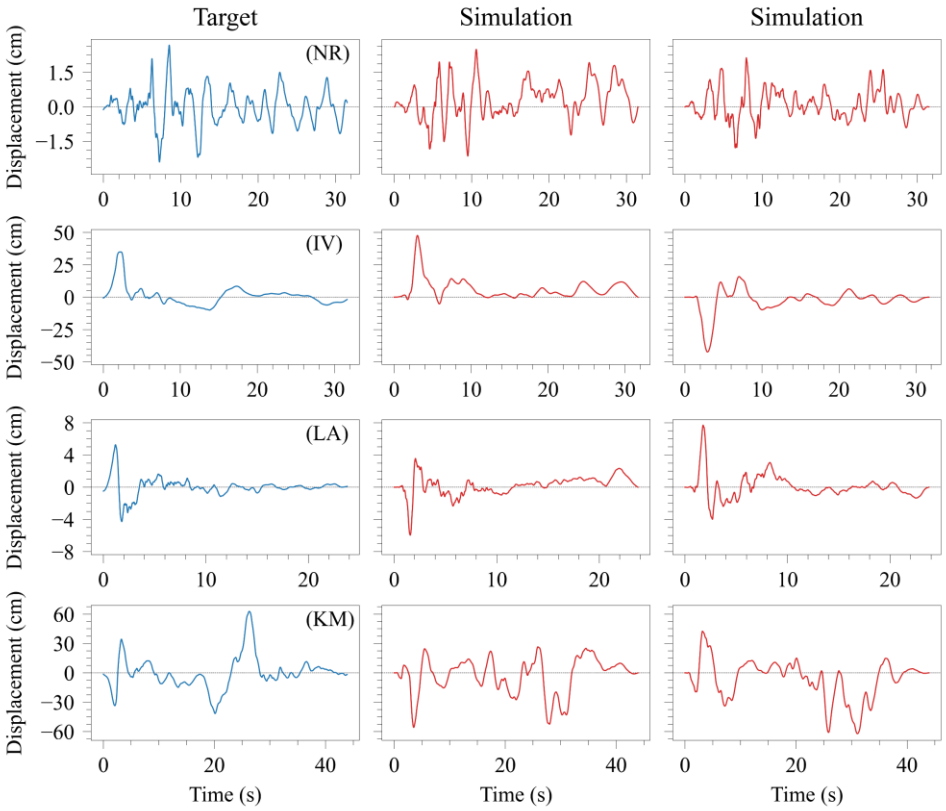


Figure 2.16. Displacement time-series and two alternative simulations using the corresponding fitted models. The panels correspond to Northridge (NR), Imperial Valley (IV), L'Aquila (LA), and Kahramanmaraş (KM) motions.

Figure 2.17 shows the cumulative energy of the target accelerograms and 20 random realizations from simulations. Cumulative energies of the target accelerograms lie within one standard deviation of the corresponding simulated motions. This indicates that the target accelerogram can be regarded as one reasonable realization of the stochastic model. It is noteworthy that cumulative energy is nonlinear with respect to the amplitude of each simulation, and the amplitude is influenced by the random component of modulated white noise, $q(\tau,\alpha)w(\tau)$, as shown in Equations 2.3 and 2.4. This explains the varying levels of simulation variability across different target records. For instance, in the case of IV, where energy arrives rapidly, the modulating function exhibits a sharper and higher peak amplitude. This causes $q(\tau,\alpha)w(\tau)$ to vary more widely, leading to an increased variability in the total energy. If a closer match between the total energy of each synthetic motion and the target is desired, simulations with total energy less than half or greater than twice (or any other threshold) of the target can be discarded [40]. Although the model provides variability, the average of simulations matches the target motion. The slight mismatch between the mean cumulative energy of the simulations (Figure 2.17) and the fitted modulating functions (Figure 2.13) is attributed to the underlying white noise, which diminishes by considering a higher number of simulations. This indicates the absence of average bias, achieved by omitting the post-processing required in other studies (e.g., [31,40,49]).

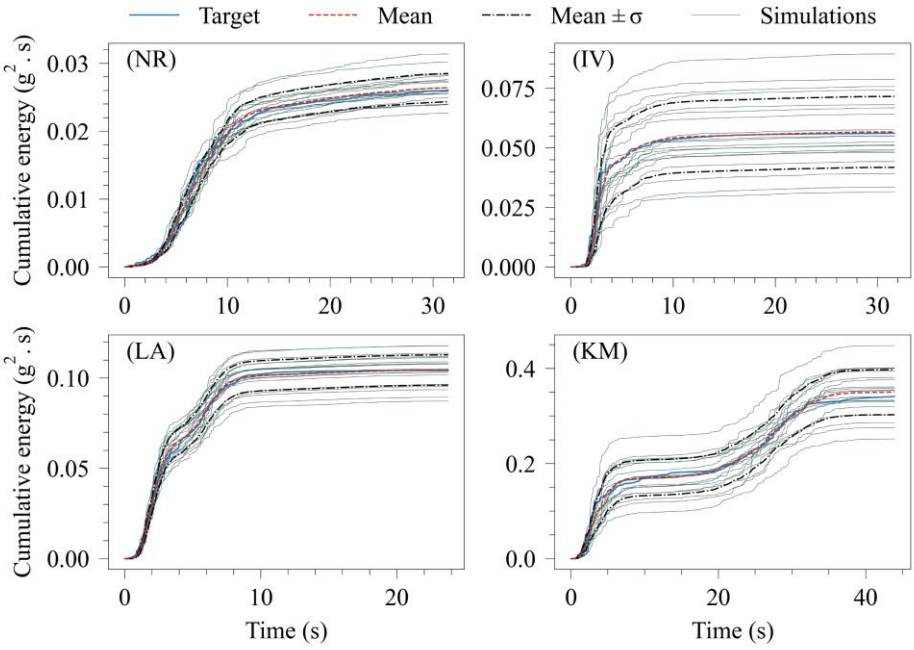


Figure 2.17. Cumulative energy of the target accelerograms and 20 random simulations using the corresponding fitted models. The panels correspond to Northridge (NR), Imperial Valley (IV), L'Aquila (LA), and Kahramanmaraş (KM) motions. The standard deviation is denoted as σ.

For further comparison, the FAS and 5%-damped response spectral acceleration (SA) for the target accelerograms and 20 random realizations from their simulations are shown in Figure 2.18 and Figure 2.19, respectively. The FAS is smoothed using a simple moving average with a window size of 9 points solely for visual comparison. FAS for simulations can be represented directly using Equation 2.4. The FAS and SA of the target motions fall within the ranges spanned by those of the simulated motions nearly across all frequency and period ranges. Therefore, the target motions can be considered reasonable realizations of the stochastic model for the given parameters. The rather smooth shape of the mean FAS and SA is attributed to the linear functional form of filter parameters, aiming to capture evolutionary dominant frequencies and bandwidth parameters in an average manner. Consequently, the linear functions do not capture all local fluctuations of these parameters. For instance, in the IV, a local peak in SA is evident around the period of 0.7 s, and the mean SA does not exhibit this distinct peak. Although

such peaks arise within the simulation range due to inherent variability, more complex functional forms could be used to capture local variations in the filter parameters. This extension is not pursued, as it would introduce additional parameters and increase model complexity.

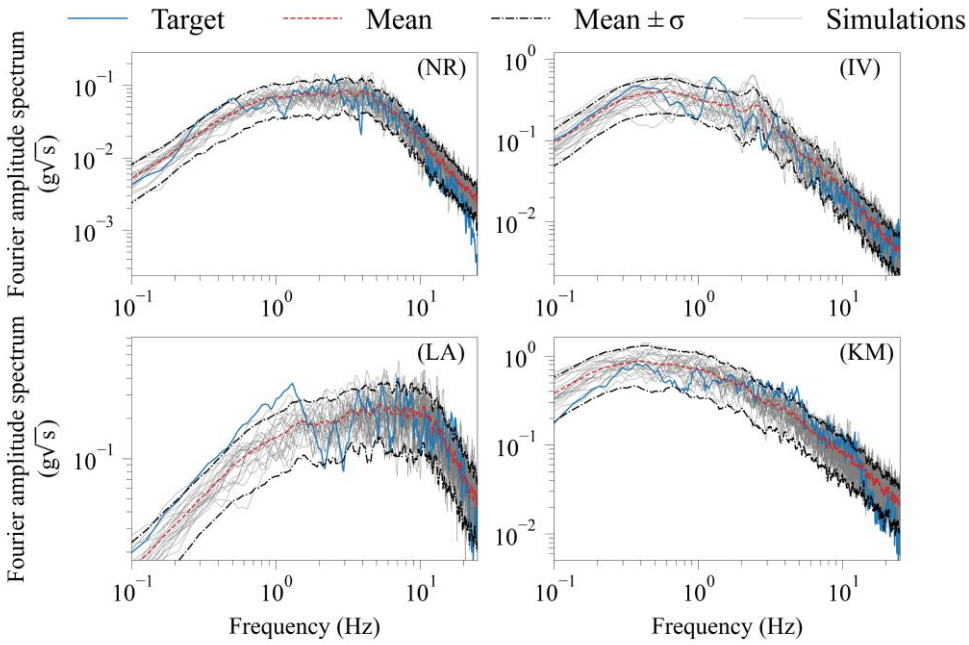


Figure 2.18. Fourier amplitude spectrum of the target accelerograms and 20 alternative simulations using the corresponding fitted models. The panels correspond to Northridge (NR), Imperial Valley (IV), L'Aquila (LA), and Kahramanmaraş (KM) motions. The standard deviation is denoted as σ.

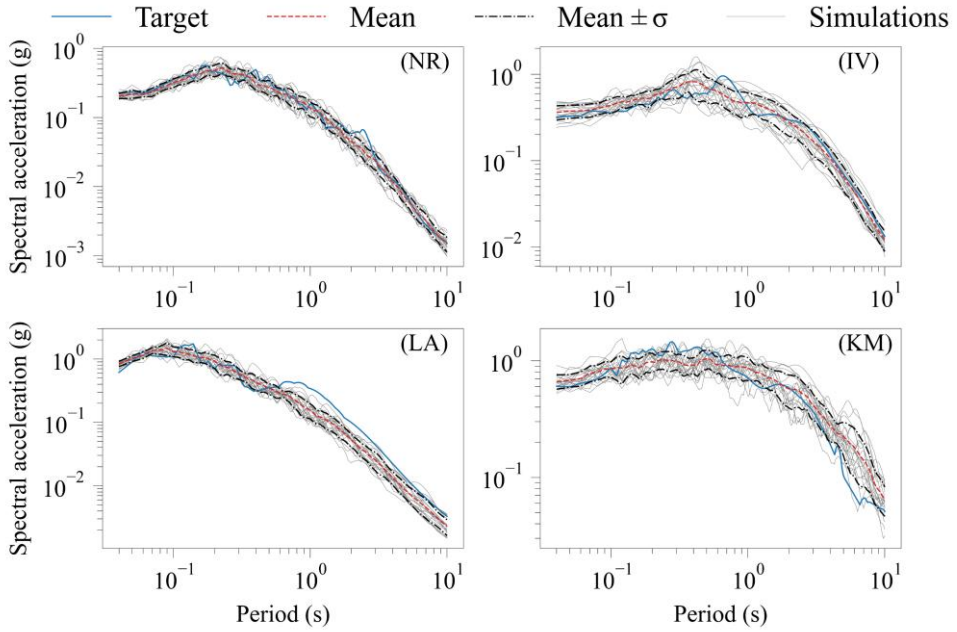


Figure 2.19. Spectral acceleration of the target accelerograms and 20 alternative simulations using the corresponding fitted models. The panels correspond to Northridge (NR), Imperial Valley (IV), L'Aquila (LA), and Kahramanmaraş (KM) motions. The standard deviation is denoted as σ.

Next, quantitative error measures for the FAS (ϵ_{FAS}) and SA (ϵ_{SA}) are respectively determined using the following formulas:

$$\epsilon_{\mathrm{FAS}} = \frac{\int_{0.1}^{25\ \mathrm{Hz}} |\mathrm{FAS}_{\mathrm{Target}}(\bar{f}) - \mathrm{E}[\mathrm{FAS}_{\mathrm{Model}}(\bar{f})]| \mathrm{d}\bar{f}}{\int_{0.1}^{25\ \mathrm{Hz}} \mathrm{FAS}_{\mathrm{Target}}(\bar{f}) \mathrm{d}\bar{f}} \quad 2.30$$

$$\epsilon_{\mathrm{SA}} = \frac{\int_{0.04}^{10\ \mathrm{s}} |\mathrm{SA}_{\mathrm{Target}}(\mathrm{T}) - \mathrm{E}[\mathrm{SA}_{\mathrm{Model}}(\mathrm{T})]| \mathrm{dT}}{\int_{0.04}^{10\ \mathrm{s}} \mathrm{SA}_{\mathrm{Target}}(\mathrm{T}) \mathrm{dT}} \quad 2.31$$

These errors are reported in Table 2.4, and alongside error measures in previous sections, they can provide an understanding of the relationship between the quantitative errors and visual assessments. These errors exhibit increased values due to the abrupt amplitude variations in the target FAS and SA. Nonetheless, based on visual assessment, the simulation model effectively captures the overall behavior.

Table 2.4. Errors associated with Fourier amplitude spectrum (FAS) and spectral acceleration (SA) for Northridge (NR), Imperial Valley (IV), L'Aquila (LA), and Kahramanmaraş (KM) ground motions.

Error metric	Identifier			
	NR	IV	LA	KM
ϵ_{FAS}	0.53	0.48	0.46	0.49
ϵ_{SA}	0.17	0.15	0.33	0.29

2.6.2. Quantitative Model Evaluation for the Selected Datasets

2.6.2.1. Empirical Cumulative Distribution Function of Errors

Quantitative evaluation of the proposed stochastic model is performed separately for the Kahramanmaraş earthquake (M_w=7.8) and pulse-like NGA-West2 datasets by comparing the characteristics of time-series, Fourier amplitude, elastic response spectra, and peak ground motion parameters of 20 random simulations with those of recorded motions. Equation 2.28 is used for the comparisons in terms of cumulative energy, MZC of acceleration, velocity, and displacement, as well as MPMNM of velocity and displacement. Equations 2.30 and 2.31 are used to compare the FAS (0.1-25 Hz) and SA (0.04-10 s), respectively. Similarly, Equation 2.31 is used for the elastic response spectra of velocity (SV) and displacement (SD) by substituting them for SA, respectively. Additionally, PGA, PGV, and peak ground displacement (PGD) are compared using Equation 2.32 by substituting each for the variable K:

$$\epsilon_{\mathrm{K}} = \frac{|\mathrm{K}_{\mathrm{target}} - \mathrm{E}[\mathrm{K}_{\mathrm{sim}}]|}{\mathrm{K}_{\mathrm{target}}} \quad 2.32$$

Figure 2.20 and Figure 2.21 illustrate the empirical cumulative distribution function (CDF) of the error values for these 13 metrics, corresponding to the Kahramanmaraş earthquake and NGA-West2 datasets, respectively. These figures illustrate the percentage of simulations (vertical axis) that fall below each error value (horizontal axis), providing an overview of the model's performance across the two datasets. Based on the previous assessments of the four example target motions, several observations are noteworthy. The very low error value based on cumulative energy indicates the accuracy of the modulating function in capturing the energy build-up in recorded motions of various earthquake scenarios within the datasets. Similarly, the low error values associated with the MZC of acceleration, velocity, and displacement for a large percentage of simulations indicate that the high, intermediate, and low-frequency content of the simulations aligns well with the target records in both datasets. Nonetheless, the error is higher for displacement MZC. This may be attributed to the more staggered curves caused by a reduced count of zero crossings or the nonlinear variation of lower dominant frequencies in a small subset of the recordings. The empirical CDF of MPMNM curves indicates that the bandwidth of the simulations aligns with the recorded datasets. For SA and SV, 90% of simulations have errors below 0.5, and SD errors are higher, consistent with the corresponding MZC errors. A similar observation is made for errors associated with PGA and PGV, with higher errors observed in PGD. For FAS, 90% of simulations have errors below 0.6,

reflecting consistently higher error values due to abrupt amplitude variations, as noted in the previous section (e.g., Table 2.4 and Figure 2.18). The results indicate that the proposed stochastic simulation model performs consistently and effectively for both selected datasets.

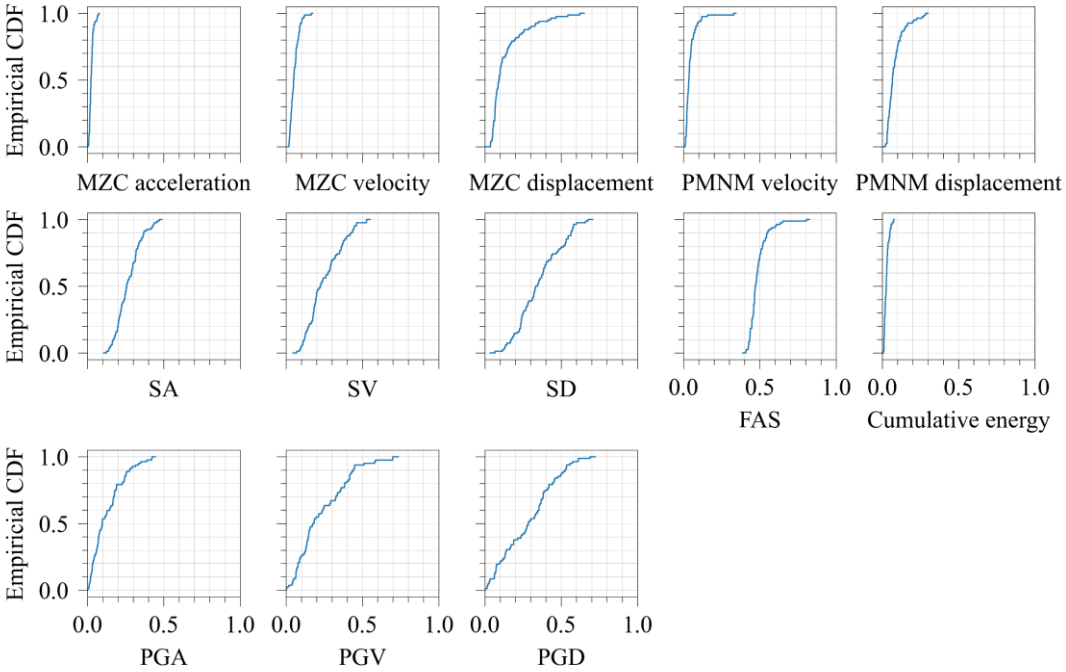


Figure 2.20. Empirical cumulative distribution function (CDF) of metrics errors for the Kahramanmaraş, Türkiye, earthquake (M_w=7.8) dataset.

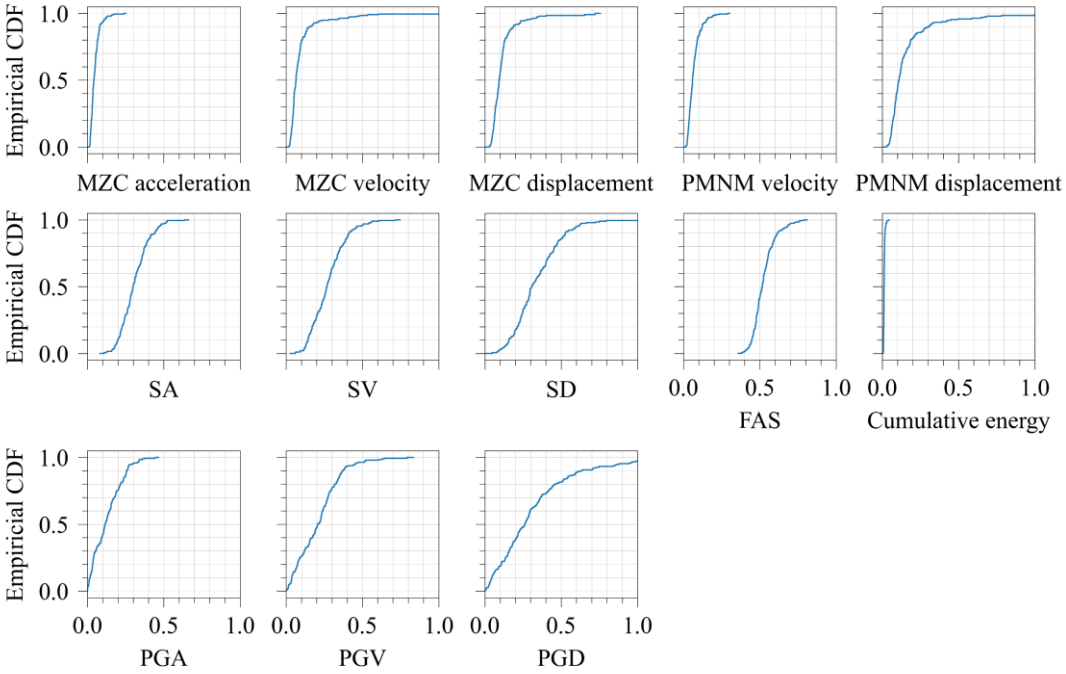


Figure 2.21. Empirical cumulative distribution function (CDF) of metrics errors for the NGA-West2 dataset.

2.6.2.2. Goodness-of-Fit Score

For further evaluation, the goodness-of-fit (GoF) score [79] is used to quantitatively compare a random simulation with its corresponding target record from the selected datasets. GoF scores are computed for the 13 considered metrics in the previous section. Figure 2.22 shows the mean GoF scores of the 13

metrics for each component at each station for the Kahramanmaraş earthquake dataset. The GoF scores are consistently above 65, indicating a very good fit for each target record [79]. The consistent GoF scores across different R_{JB} values, as well as for pulse-like and non-pulse-like motions of this event, indicate that the proposed stochastic model performs efficiently and consistently across the dataset, from near-fault pulse-like to far-field non-pulse-like motions. Figure 2.23 shows similar consistent performance for the NGA-West2 dataset, indicating that the proposed model effectively captures ground motions with notable low-frequency content, typical of pulse-like motions.

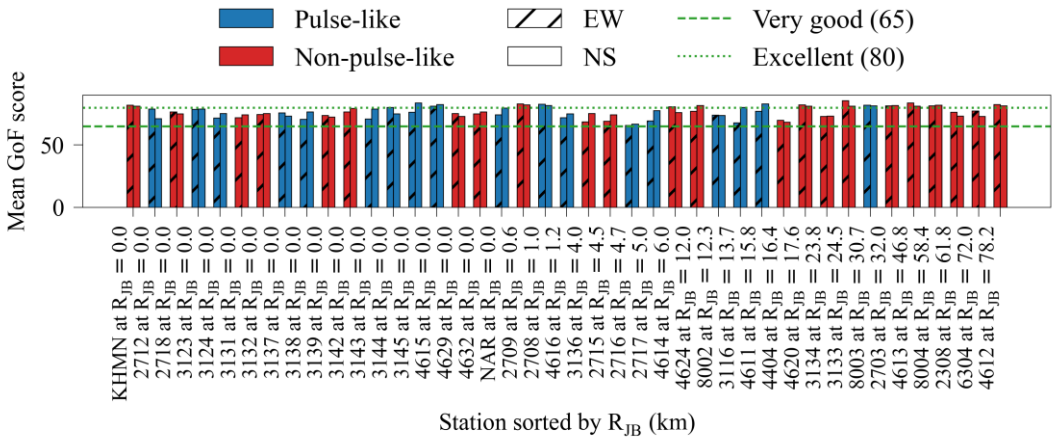


Figure 2.22. Mean goodness-of-fit (GoF) scores for the east-west (EW) and north-south (NS) components across stations for the Kahramanmaraş, Türkiye, earthquake dataset.

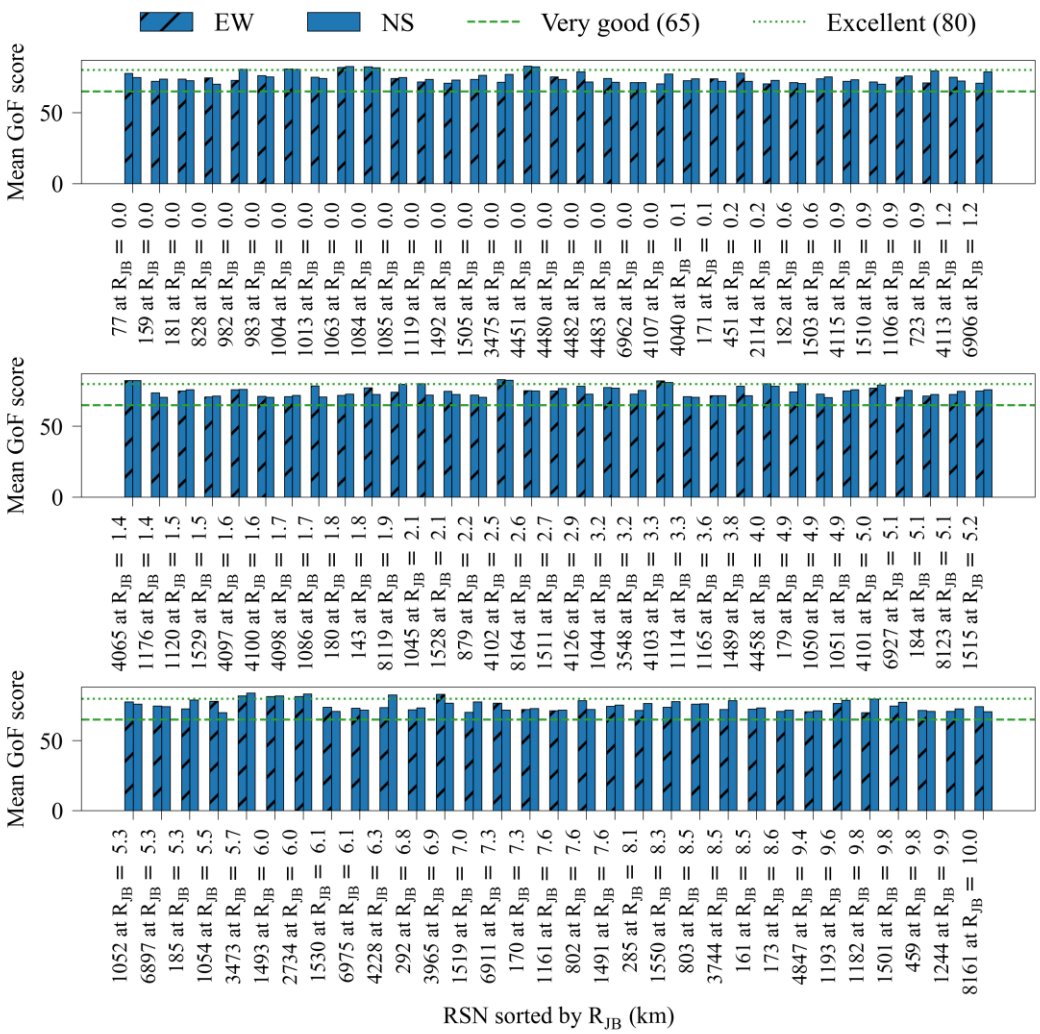


Figure 2.23. Mean goodness-of-fit (GoF) scores for the east-west (EW) and north-south (NS) components across record sequence number (RSN) for the NGA-West2 dataset.

To evaluate the performance of the proposed stochastic model for each metric individually, the mean GoF score for each metric is calculated within each dataset. Figure 2.24 and Figure 2.25 show the mean GoF scores of each metric, averaged across all stations for the Kahramanmaraş earthquake and pulse-like NGA-West2 datasets, respectively. The results show that the simulations achieve a very good fit for all metrics, except for FAS, which shows a fair fit (GoF > 45), mostly due to the abrupt amplitude variations discussed previously.

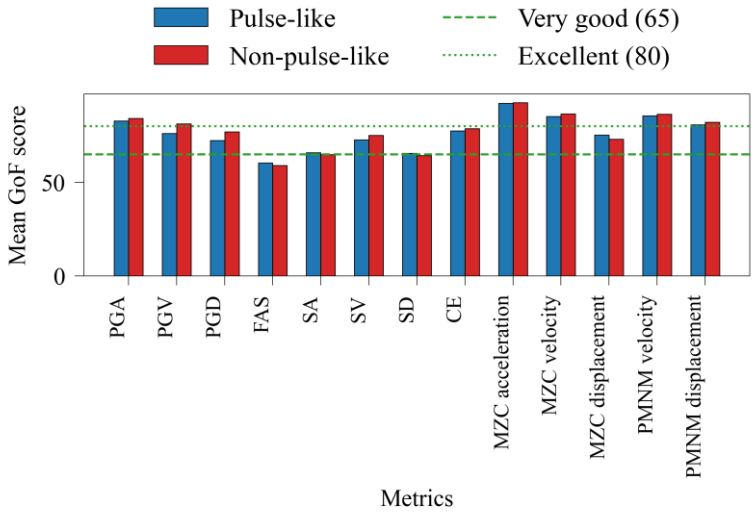


Figure 2.24. Mean goodness-of-fit (GoF) scores for each metric averaged across all stations, for pulse-like and non-pulse-like motions from the Kahramanmaraş, Türkiye, earthquake dataset.

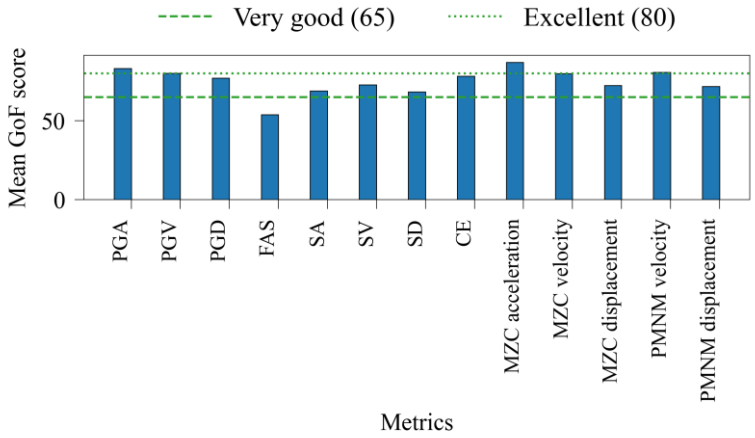


Figure 2.25. Mean goodness-of-fit (GoF) scores for each metric, averaged across all stations, for pulse-like motions from the NGA-West2 dataset.

2.6.2.3. Inter-Period Correlation of Spectral Acceleration Ordinates

Furthermore, the correlations between the spectral acceleration ordinates of the recorded motions and the corresponding simulated motions within periods of 0.04 to 10 s are compared. These correlations can be an important indicator of the seismic demand in multi-degree-of-freedom (MDoF) systems that are excited at various vibration periods [37]. Figure 2.26 illustrates these correlations separately for the Kahramanmaraş earthquake and NGA-West2 datasets. It includes recorded motions and individual simulated motions (one random simulation per target record). It is noteworthy that considering a specific set of model parameters corresponding to a station (a recorded motion), a set of simulations at that station does not show a significant correlation due to the stochasticity introduced by underlying white noise. However, when different stations (different sets of parameters) are considered, even with a single random simulation, correlations emerge that align with those observed in real records.

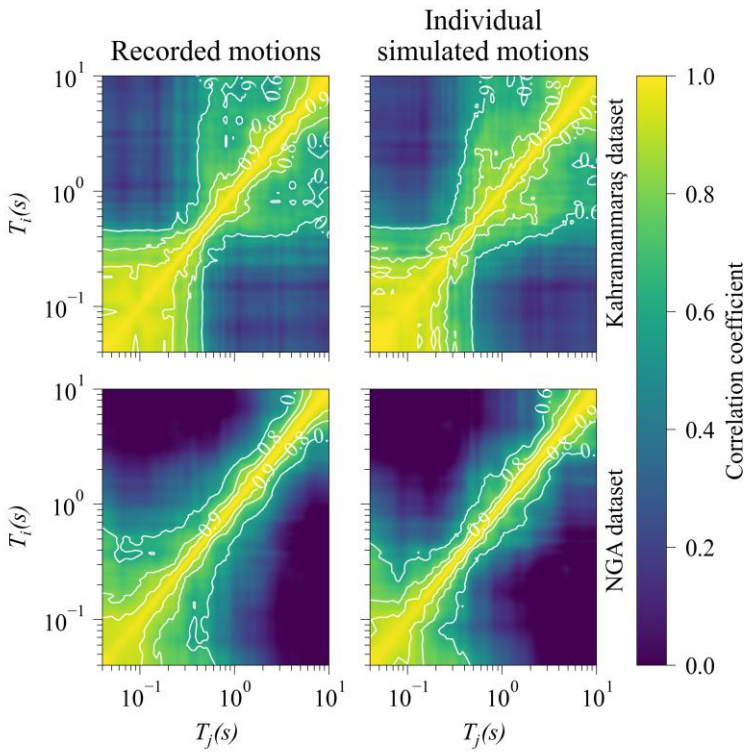


Figure 2.26. Correlations between spectral acceleration ordinates of recorded and individual simulated motions for the pulse-like and non-pulse-like Kahramanmaraş earthquake dataset and pulse-like NGA dataset.

Overall, the simulated and target ground motions exhibit similar evolutionary features. The identified model parameters implicitly consider the properties of the earthquake and site corresponding to a target motion. Thus, the proposed stochastic model can generate a set of ground motions suitable for designing and evaluating a structure for that specific earthquake and site characteristics. The developed framework has been implemented as an open-source Python package. Further details are provided in Chapter 5, Section 5.3.

2.7. Conclusions

This chapter presented an enhanced fully nonstationary site-based stochastic ground motion simulation framework. The proposed formulation extends its applicability to more complex ground motion characteristics, including multiple strong motion phases and low-frequency content associated with near-fault directivity and potential basin effects, without relying on deterministic directivity pulse models or post-processing corrections. The improvements are achieved through a revised formulation, the use of an enhanced frequency filter, and a new time-modulating function. As a result, the approach directly preserves the energy characteristics of simulated motions while maintaining a separable representation of temporal and spectral nonstationarities. Consequently, the overall framework remains parsimonious and physically interpretable.

Validation against a diverse set of earthquake records confirmed the capability of the proposed simulation framework in reproducing a wide range of ground motion features with good agreement in both time- and frequency-domain characteristics. Although the framework performs effectively when its parameters are known, its practical application to predictive, scenario-specific simulations depends on estimating these parameters from seismological and site descriptors. To address this requirement, Chapter 3 develops a unified multivariate mixed-effects regression framework for parameter prediction.

Chapter 3
Multivariate Mixed-Effects Framework

The contents of this chapter have been published in Earthquake Engineering & Structural Dynamics. Minor formatting and structural modifications have been made to align with the overarching thesis narrative. The original article may be cited as:
Hussaini SMS, Karimzadeh S, Lourenço PB. A Multivariate Mixed-Effects Regression Framework for Ground Motion Modeling: Integrating Parametric and Machine Learning Approaches. Earthquake Engineering & Structural Dynamics 2026: eqe.70168. DOI: 10.1002/eqe.70168

3.1. Introduction

Chapter 2 presented an enhanced broadband stochastic ground motion simulation methodology capable of reproducing a broad range of observed earthquake records through a compact set of physically interpretable simulation parameters. However, practical application within seismic hazard and engineering analyses requires a statistical framework capable of predicting the simulation parameters from earthquake source, path, and site characteristics. Furthermore, because the simulation parameters jointly govern waveform amplitude, frequency content, duration, and temporal evolution, they cannot be treated as independent quantities. Their statistical dependence must be represented explicitly to ensure physically realistic simulations and to preserve consistency with observed ground motion variability.

Building on the insights developed so far, this chapter presents a unified multivariate mixed-effects regression (MMER) framework for modeling multiple correlated outcomes and for developing ground motion models (GMMs). The primary objective is to introduce a regression framework that allows decomposing total uncertainty into multiple grouping factors (e.g., between-event, between-site, and other hierarchical sources of variability) and residual components while remaining flexible to accommodate either parametric functions or nonparametric machine learning (ML) methods for the fixed-effects component.

A central characteristic of the framework is its modular architecture. The formulation is intentionally designed to remain agnostic regarding the specification of the fixed-effects component. Consequently, conventional parametric functions, generalized linear formulations, and ML models can all be incorporated within the same mixed-effects structure without modification of the underlying variance decomposition. This flexibility is particularly important for applications in ground motion modeling, where both physically motivated parametric relationships and data-driven representations remain widely used.

To demonstrate the capabilities of the framework and verify its consistency, three illustrative ground motion models are developed using a subset of the NGA-West2 database [83]. These examples include a conventional linear fixed-effects model as a simple benchmark and two multi-layer perceptron (MLP) models that demonstrate the incorporation of data-driven predictive approaches within the proposed framework. The purpose of these examples is not to advocate a particular predictive methodology or to develop comprehensive, production-ready GMMs in this chapter. Rather, they are intended to demonstrate the generality, flexibility, and adaptability of the MMER framework across fundamentally different fixed-effects representations.

Although the framework is illustrated using seismic data applications throughout this chapter, its mathematical structure is fundamentally domain independent. The methodology is applicable to any multivariate hierarchical dataset in which multiple correlated responses must be jointly modeled while accounting for nested or crossed sources of variability. Within the broader context of this thesis, however,

the framework provides the statistical foundation required to transform the stochastic simulation methodology developed in Chapter 2 into a hazard-compatible predictive system capable of generating physically consistent ground motion simulations from earthquake source, path, and site information.

3.2. Multivariate Mixed-Effects Modeling Framework

This section presents the general mathematical formulation of the proposed framework. The notation introduced here is illustrated later in Section 3.4.1 (Data Processing).

3.2.1. General Formulation

The core of the proposed framework is a unified mixed-effects model, which treats the fixed-effects component in a modular way [98]. The model accommodates k independent grouping factors, with each factor contributing linear random effects (e.g., random intercept and slopes), along with a flexible fixed-effects component. The multivariate mixed-effects model for m response variables is expressed as:

$$y = f(x) + \sum_{i=1}^{k} (I_m \otimes Z_i) b_i + \epsilon \quad 3.1$$

where $y = [y_1^T\ y_2^T\ \dots\ y_m^T]^T$, $f(x) = [f_1^T(x)\ f_2^T(x)\ \dots\ f_m^T(x)]^T$, and $\epsilon = [\epsilon_1^T\ \epsilon_2^T\ \dots\ \epsilon_m^T]^T$ are the $mn \times 1$ vectors of response variables, fixed-effects estimates, and unexplained residuals, respectively. x is an $n \times p$ covariate design matrix of predictors, where n and p denote the number of observations and predictors, respectively. I_m is an $m \times m$ identity matrix, and Z_i with shape $n \times q_i o_i$ is the random-effects design matrix for the i^{th} grouping factor that maps each observation to its corresponding grouping level and effect type (e.g., random intercept and random slope). Finally, b_i is the $mq_i o_i \times 1$ vector of random-effects estimates, where o_i and q_i denote the number of grouping levels and effect types for the i^{th} grouping factor, respectively (Refer to Section 3.4.1 for illustration).

It is assumed that $\epsilon \sim N(0, R)$, where R denotes the full residual covariance matrix, defined as:

$$R = \phi \otimes I_n \quad 3.2$$

where I_n is an $n \times n$ identity matrix, assuming ϵ values are independent across observations, and ϕ is an $m \times m$ matrix, modeling the between-response covariance. Similarly, it is assumed that for each i^{th} grouping factor, $b_i \sim N(0, D_i)$, where D_i denotes the full random-effects covariance matrix, defined as:

$$D_i = \tau_i \otimes I_{o_i} \quad 3.3$$

where I_{o_i} is an $o_i \times o_i$ identity matrix, assuming b_i values are independent across grouping levels (e.g., independent earthquakes), and τ_i is an $mq_i \times mq_i$ matrix, modeling the between-response-effect covariance.

$f(x)$ is assumed to be a general (i.e., either parametric or nonparametric) function of the same covariate design matrix (x) across all responses. The set of unknown parameters is denoted as $\theta = \{f(x), \phi, \{\tau_i\}_{i=1}^k\}$ and the set of latent random effects estimates as $b = \{b_i\}_{i=1}^k$. Under the normality assumption of residuals and independence of the priors for the random effects (i.e., $p(b) = \prod_{i=1}^k p(b_i)$), the marginal probability distribution of observations is expressed as [98]:

$$y \sim N(f(x), V) \quad 3.4$$

where V is the marginal covariance matrix of the observations after integrating out the random effects. It is expressed as:

$$V = \sum_{i=1}^{k} (I_m \otimes Z_i) D_i (I_m \otimes Z_i)^T + R \quad 3.5$$

Ultimately, the marginal log-likelihood (L_m) follows the standard form used in previous studies [72,74]:

$$L_m(b,\theta \mid y) = \log p(y \mid b,\theta) = -\frac{1}{2}((y-f(x))^T V^{-1}(y-f(x) + mn\log(2\pi) + \log|V| \quad 3.6$$

3.2.2. Estimation of Unknown Parameters

To estimate the unknown parameters, the expectation-maximization (EM) algorithm based on maximum likelihood estimation (MLE) is used. The MLE approach estimates unknown parameters by maximizing the marginal log-likelihood of the observations, which is often analytically intractable. The EM algorithm instead finds the MLE of the model parameters by iteratively maximizing the expected value of the complete-data log-likelihood, given the observed data and current parameter estimates [98]. The complete-data log-likelihood, based on the joint distribution of the observed data and the assumed random-effects priors, is expressed as:

$$L_c(\theta \mid y,b) = \log p(y,b \mid \theta) = \log p(y \mid b,\theta) + \log p(b \mid \theta) \quad 3.7$$

$$L_c(\theta \mid y,b) = -\frac{1}{2}\left(\epsilon^T R^{-1}\epsilon + mn\log(2\pi) + \log|R| + \sum_{i=1}^{k}\left(b_i^T D_i^{-1} b_i + mq_i o_i \log(2\pi) + \log|D_i|\right)\right) \quad 3.8$$

If the current parameter estimates are denoted as $\hat{\theta}_{t-1} = \{\hat{f}(x), \hat{\phi}, \{\hat{\tau}_i\}_{i=1}^k\}$, then the expected value of $L_c(\theta \mid y,b)$ taken with respect to the distribution of b conditioned on y and $\hat{\theta}_{t-1}$, is given by the Q-function below:

$$Q(\theta \mid \hat{\theta}_{t-1}) = -\frac{1}{2}\left(E\left[\epsilon^T R^{-1}\epsilon \mid y,\hat{\theta}_{t-1}\right] + mn\log(2\pi) + \log|R| + \sum_{i=1}^{k}\left(E\left[b_i^T D_i^{-1} b_i \mid y,\hat{\theta}_{t-1}\right] + mq_i o_i \log(2\pi) + \log|D_i|\right)\right) \quad 3.9$$

The expected value and variance of residuals, given y and $\hat{\theta}_{t-1}$ are expressed as:

$$E\left[\epsilon \mid y,\hat{\theta}_{t-1}\right] = \hat{\epsilon} = y - f(x) - \sum_{i=1}^{k}(I_m \otimes Z_i)\mu_i \quad 3.10$$

$$Var\left[\epsilon \mid y,\hat{\theta}_{t-1}\right] = \sum_{i=1}^{k}(I_m \otimes Z_i)\Sigma_i(I_m \otimes Z_i)^T \quad 3.11$$

here μ_i and Σ_i denote the expected value and conditional covariance of random effects given y and $\hat{\theta}_{t-1}$, respectively. The full posterior $p(b \mid y)$ is a multivariate Gaussian, because the conditional distribution $p(y \mid b)$, prior $p(b)$, and joint distribution $p(y,b)$ are all Gaussian. While the observed data introduces dependencies among the posteriors, each b_i can still be represented through its marginal conditional distribution. Therefore:

$$\mu_i = D_i(I_m \otimes Z_i)^T V^{-1}(y - f(x)) \quad 3.12$$

$$\Sigma_i = D_i - D_i(I_m \otimes Z_i)^T V^{-1}(I_m \otimes Z_i)D_i \quad 3.13$$

The two expectation terms in Equation 3.9 can be expressed as:

$$E\left[\epsilon^T R^{-1}\epsilon \mid y,\hat{\theta}_{t-1}\right] = \hat{\epsilon}^T R^{-1}\hat{\epsilon} + \text{trace}\left(R^{-1}\sum_{i=1}^{k}(I_m \otimes Z_i)\Sigma_i(I_m \otimes Z_i)^T\right) \quad 3.14$$

$$\mathrm{E}\left[\, \mathrm{b}_\mathrm{i}^\mathrm{T} \mathrm{D}_\mathrm{i}^{-1} \mathrm{b}_\mathrm{i} \mid \mathrm{y}, \hat{\theta}_{t-1} \,\right] = \mu_\mathrm{i}^\mathrm{T} \mathrm{D}_\mathrm{i}^{-1} \mu_\mathrm{i} + \mathrm{trace}\left(\mathrm{D}_\mathrm{i}^{-1} \Sigma_\mathrm{i}\right) \tag{3.15}$$

Therefore, the Q-function can be expressed as:

$$\begin{aligned} \mathrm{Q}\left(\, \theta \mid \hat{\theta}_{t-1} \,\right) = -\frac{1}{2}\Bigg(& \hat{\epsilon}^\mathrm{T} \mathrm{R}^{-1} \hat{\epsilon} + \mathrm{trace}\left(\mathrm{R}^{-1} \sum_{\mathrm{i}=1}^{\mathrm{k}} (\mathrm{I}_\mathrm{m} \otimes \mathrm{Z}_\mathrm{i}) \Sigma_\mathrm{i} (\mathrm{I}_\mathrm{m} \otimes \mathrm{Z}_\mathrm{i})^\mathrm{T} \right) + \mathrm{mn} \log(2\pi) \\ & + \log|\mathrm{R}| + \sum_{\mathrm{i}=1}^{\mathrm{k}} \left(\mu_\mathrm{i}^\mathrm{T} \mathrm{D}_\mathrm{i}^{-1} \mu_\mathrm{i} + \mathrm{trace}\left(\mathrm{D}_\mathrm{i}^{-1} \Sigma_\mathrm{i}\right) + \mathrm{mq_i o_i} \log(2\pi) + \log|\mathrm{D_i}| \right) \Bigg) \end{aligned} \tag{3.16}$$

where only R depends on ϕ and $\mathrm{D_i}$ depends on τ_i, while all other terms are fixed at $\hat{\theta}_{t-1}$.

3.2.2.1. Estimation of Fixed Effects $f(x)$

The fixed effects are estimated by fitting $\mathrm{f(x)}$ to the adjusted data after updating all random effects estimates, using standard regression methods such as least squares. The adjusted data is expressed as:

$$\mathrm{y_{adj}} = \mathrm{y} - \sum_{\mathrm{i}=1}^{\mathrm{k}} (\mathrm{I_m} \otimes \mathrm{Z_i}) \mu_\mathrm{i} \tag{3.17}$$

3.2.2.2. Estimation of Core Residual Covariance ϕ

For the assumed structure of R, it is obtained that $\mathrm{R}^{-1} = \phi^{-1} \otimes \mathrm{I_n}$ and $\log|\mathrm{R}| = \mathrm{n} \log|\phi|$. Let $\hat{\epsilon} = \mathrm{vec}(\hat{\mathrm{E}})$, where $\hat{\mathrm{E}}$ is an $\mathrm{n} \times \mathrm{m}$ residual matrix, and let its empirical covariance matrix be $\mathrm{S} = \mathrm{E}^\mathrm{T}\mathrm{E}$. Applying standard properties of the trace and Kronecker product yields:

$$\hat{\epsilon}^\mathrm{T} \mathrm{R}^{-1} \hat{\epsilon} = \mathrm{trace}(\phi^{-1} \mathrm{S}) \tag{3.18}$$

For the $\mathrm{i^{th}}$ grouping factor, treating Σ_i as a block matrix and applying standard trace properties yields:

$$\begin{aligned} \mathrm{trace}\left(\mathrm{R}^{-1} (\mathrm{I_m} \otimes \mathrm{Z_i}) \Sigma_\mathrm{i} (\mathrm{I_m} \otimes \mathrm{Z_i})^\mathrm{T}\right) &= \mathrm{trace}\left(\left(\phi^{-1} \otimes \left(\mathrm{Z_i^T Z_i}\right) \right) \Sigma_\mathrm{i} \right) \\ &= \sum_{\mathrm{j}=1}^{\mathrm{m}} \sum_{\mathrm{g}=1}^{\mathrm{m}} \phi_{\mathrm{jg}}^{-1} \, \mathrm{trace}\left(\left(\mathrm{Z_i^T Z_i}\right) \Sigma_{\mathrm{i_{gj}}} \right) \end{aligned} \tag{3.19}$$

By considering all grouping factors, the second term in Equation 3.16 is expressed as:

$$\begin{aligned} \mathrm{trace}\left(\mathrm{R}^{-1} \sum_{\mathrm{i}=1}^{\mathrm{k}} (\mathrm{I_m} \otimes \mathrm{Z_i}) \Sigma_\mathrm{i} (\mathrm{I_m} \otimes \mathrm{Z_i})^\mathrm{T} \right) &= \sum_{\mathrm{i}=1}^{\mathrm{k}} \left(\sum_{\mathrm{j}=1}^{\mathrm{m}} \sum_{\mathrm{g}=1}^{\mathrm{m}} \phi_{\mathrm{jg}}^{-1} \, \mathrm{trace}\left(\left(\mathrm{Z_i^T Z_i}\right) \Sigma_{\mathrm{i_{gj}}} \right) \right) \\ &= \mathrm{trace}(\phi^{-1} \mathrm{T}) \end{aligned} \tag{3.20}$$

where T is an $\mathrm{m} \times \mathrm{m}$ covariance correction matrix that restores the variance absorbed by the uncertainty in the random effects, with $\mathrm{T_{gj}} = \sum_{\mathrm{i}=1}^{\mathrm{k}} \mathrm{trace}\left(\left(\mathrm{Z_i^T Z_i}\right) \Sigma_{\mathrm{i_{gj}}} \right)$. Substituting Equations 3.18 and 3.20 back into Equation 3.16 and maximizing it with respect to ϕ yields:

$$\phi = \frac{\mathrm{S} + \mathrm{T}}{\mathrm{n}} \tag{3.21}$$

3.2.2.3. Estimation of Core Random-Effects Covariance τ

The core covariance matrix τ_i is obtained for each $\mathrm{i^{th}}$ grouping factor, because the summation in Equation 3.16 is separable. Let $\mu_\mathrm{i} = \mathrm{vec}(\mathrm{B_i})$, where $\mathrm{B_i}$ is a $\mathrm{o_i} \times \mathrm{mq_i}$ random-effects matrix, and let its empirical covariance matrix be $\mathrm{U_i} = \mathrm{B_i^T B_i}$. It can be written that:

$$\mu_\mathrm{i}^\mathrm{T} \mathrm{D}_\mathrm{i}^{-1} \mu_\mathrm{i} = \mathrm{trace}(\tau_\mathrm{i}^{-1} \mathrm{U_i}) \tag{3.22}$$

$$\operatorname{trace}\left(D_i^{-1}\Sigma_i\right) = \sum_{j=1}^{mq_i}\sum_{g=1}^{mq_i} \tau_{i_{jg}}^{-1} \operatorname{trace}(\Sigma_{i_{gj}}) = \operatorname{trace}\left(\tau_i^{-1} W_i\right) \quad 3.23$$

where W_i is a $mq_i \times mq_i$ covariance correction matrix that restores the variance absorbed by the uncertainty in the random effects, with $W_{i_{gj}} = \operatorname{trace}\left(\Sigma_{i_{gj}}\right)$. Substituting Equations 3.22 and 3.23 back into Equation 3.16 and maximizing it with respect to τ_i yields:

$$\tau_i = \frac{U_i + W_i}{o_i} \quad 3.24$$

The iterative MLE-based EM algorithm for the mixed-effects model can be summarized as:

1. Initialize core variance matrices ϕ and τ_i for $i = 1, 2, \ldots, k$ as identity matrices.
2. An estimate of fixed effects is obtained by fitting $f(x)$ to the observed data.
3. Calculate μ_i and Σ_i for $i = 1, 2, \ldots, k$ according to Equations 3.12 and 3.13, respectively.
4. Update the fixed effects by fitting $f(x)$ to the adjusted data in Equation 3.17.
5. Update ϕ and τ_i for $i = 1, 2, \ldots, k$ according to Equations 3.21 and 3.24, respectively.
6. Repeat steps 3 to 5 until convergence using the marginal log-likelihood value in Equation 3.6.

Specifically, convergence is achieved when the relative change in the marginal log-likelihood between consecutive EM iterations falls below a predefined tolerance threshold (e.g., 10^{-6}), ensuring that the parameter estimates have stabilized. The developed framework has been implemented as an open-source Python package. Further details are provided in Chapter 5, Section 5.3.

3.3. Ground Motion Dataset and Variables

The illustrative GMMs are developed using the ground motion data from PEER NGA-West2 [83]. A subset of the NGA-West2 dataset was selected according to the following criteria:

- **Magnitude Range:** Events with moment magnitude $M_w \geq 4.0$ to ensure adequate signal-to-noise ratios.
- **Distance Range:** Recordings with the closest distance to the rupture plane $R_{rup} \leq 250$ km.
- **Usable Bandwidth:** Records were required to have a maximum usable period of at least 10 s (equivalently, minimum usable frequency ≤ 0.1 Hz) to ensure reliable long-period spectral ordinates across the full set of target periods.
- **Data Completeness:** Although mixed-effects models can theoretically handle unequal recordings per group, requiring a minimum number per event or station generally improves the interpretability of random-effects estimates. Such a limit was not imposed in this chapter for two reasons. First, the unconstrained ML component requires large datasets to effectively learn complex patterns, and enforcing strict grouping criteria (e.g., 3 to 5 recordings per station) would substantially reduce the available training data. Second, mixed-effects models naturally handle sparse groups through statistical shrinkage, pulling their estimates toward the global mean (Equation 3.12). By retaining these observations, the information available for estimating fixed effects is maximized while relying on shrinkage to maintain stability, thereby demonstrating the framework's robustness in handling unbalanced data. Crucially, because individual random-effect estimates are not interpreted as inferential quantities, the higher posterior uncertainty (Equation 3.13) for singleton groups does not compromise the validity of the fixed-effects estimates or the overall variance partitioning.

The resulting dataset includes 4217 recordings from 98 events and 2383 stations, with 76 events and 1005 stations having at least two recordings. Based on the filtered dataset, a concise set of five common predictor variables is selected: M_w, depth to the top of the rupture plane (Z_{tor}), R_{rup}, average shear wave velocity in the upper 30 m of soil (V_{S30}), and fault mechanism (F_m). The response variable is selected as

the RotD50 of SA, which represents the median 5%-damped SA computed from the two horizontal components of a ground motion rotated through all non-redundant angles [99]. Spectral ordinates are considered at 40 values over periods from 0.01 s to 10 s, approximately spaced at logarithmic intervals. Figure 3.1 shows the distribution of the selected dataset across M_w, R_{rup}, V_{S30}, and Z_{tor}. The dataset also includes five categories of F_m: Strike-slip, normal, reverse, reverse oblique, and normal oblique.

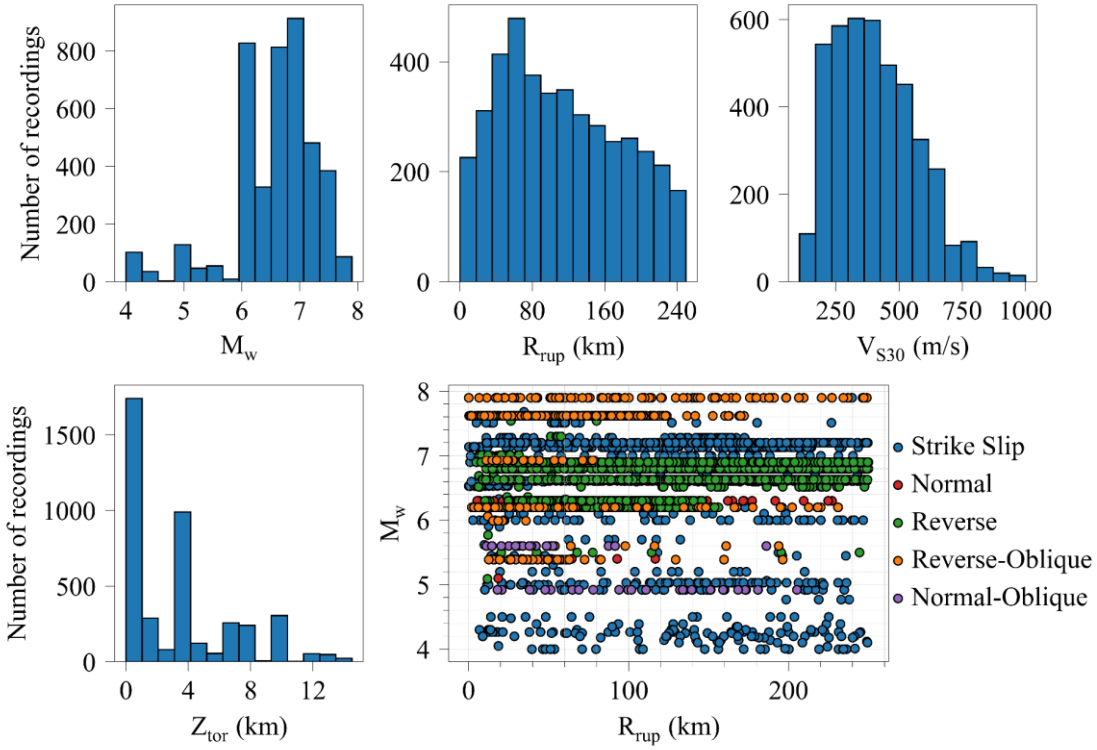


Figure 3.1. Distribution of different seismological parameters of the selected dataset.

3.4. Model Development Methodology

To demonstrate the flexibility of the proposed multivariate mixed-effects framework, three illustrative GMMs are considered. The first and second GMMs share the same random-effects structure but differ in the fixed-effects component, while the second and third GMMs share the same fixed effects but differ in the random-effects structure. In the first GMM, $f(x)$ is a simple linear function without any specific nonlinear terms, whereas in the second and third GMMs, it is represented by a nonparametric MLP neural network. Two crossed grouping factors are included: earthquake events and stations, each with a random intercept representing between-event and between-site variation. In the third GMM, a random slope for M_w is added to capture magnitude-dependent variation in the between-event term. These terms allow group-specific deviations from the fixed effects. The between-event and between-site intercepts capture systematic offsets for each earthquake and recording station, respectively, while the between-event slope allows the scaling relationship with M_w to vary across earthquakes. Although M_w is constant for any individual event, combining event-specific intercept and slope terms results in a single realized event deviation whose variance can vary as a quadratic function of M_w across the population of earthquakes. This flexibility introduces magnitude-dependent heteroscedasticity in the between-event term, enabling the model to capture complex uncertainty trends, such as the nonmonotonic variability across different M_w ranges.

3.4.1. Data Processing

To ensure consistency, all models were fitted and evaluated on the same dataset, enabling a direct and unbiased comparison. Ground motion records from the same seismic event are inherently correlated and cannot be treated as independent samples. To prevent data leakage and avoid overly optimistic performance estimates, a standard random split is inappropriate. Instead, the dataset was partitioned by earthquake events into a training set (75%) and a test set (25%), ensuring that all records from a given earthquake are entirely contained within either the training or test set. This guarantees that the test set consists of completely unseen seismic events, providing a robust and realistic assessment of the model's generalization capability. Because each recording corresponds to a unique event–station pair, splitting by both event and station would be effectively equivalent to a random split and would not meaningfully evaluate generalization to new seismic sources.

Following common practice, the natural logarithm of R_{rup}, V_{S30}, and SA is used to reduce right-skewness, which also helps stabilize variance and linearize their relationships. Additionally, for MLP models, scaling predictors is essential to prevent features with larger numeric ranges from dominating training. Therefore, all numeric predictors were standardized to have a zero mean and a unit variance. Although not strictly required for linear regression, standardization can improve numerical stability and ensure consistency across models. The categorical predictor F_m is nominal and has no intrinsic ordering; assigning ordinal values (e.g., 1, 2, etc.) would incorrectly imply ranking or distances between categories. Instead, F_m values were encoded as binary indicator variables, omitting one category as the reference to avoid collinearity in the linear model. Using the same processed data ensures that any observed differences in performance between the models can be attributed to their architectural differences or random-effects structure rather than variations in the input data representation.

Following the event-based data partitioning, the training set consists of n = 3199 observations used to develop the models. For each observation, there are m = 40 response variables (i.e., SA at different periods). The fixed-effects components use p = 5 predictor variables (i.e., M_w, R_{rup}, Z_{tor}, V_{S30}, F_m). The random-effects structure includes two grouping factors (k=2): (1) earthquake events, with $o_1 = 78$ unique events, and (2) recording stations, with $o_2 = 2126$ unique stations. For the models with only random intercepts (first and second GMMs), the number of random effects per grouping factor is $q_1 = 1$ and $q_2 = 1$. In the third model, which includes a random slope for the between-event term, $q_1 = 2$ (intercept and slope), while the between-site term remains $q_2 = 1$.

3.4.2. Fixed-Effects Models

For the linear model, each response (i.e., SA at a given period) is modeled as a linear function of the transformed predictors. Specifically, the functional form is defined as:

$$\ln(y) = c_0 + c_1 M_w + c_2 Z_{tor} + c_3 \ln(R_{rup}) + + c_4 \ln(V_{S30}) + c_5 F_m \quad 3.25$$

where c_0 through c_5 are the regression coefficients estimated iteratively within the framework. This simplified log-linear form was intentionally adopted to serve as a transparent and stable baseline. While established GMMs (e.g., [100]) employ more elaborate, nonlinear predictor transformations to represent effects such as magnitude saturation and anelastic attenuation, our objective here is not to refine existing empirical formulations. Rather, the flexibility of the proposed multivariate mixed-effects framework when paired with different fixed-effects estimators is demonstrated. Using a reduced parametric form allows the methodological behavior of the framework to be isolated and provides a clear reference against which the data-driven MLP models can be evaluated. While the framework is demonstrated here, its modular design allows for the seamless incorporation of more sophisticated models. Indeed, these capabilities are explored in Chapter 4, where physics-informed neural additive models (NAMs) are integrated into the MMER structure to enforce essential seismological scaling laws. In the linear implementation, a separate linear function is defined for each response, but these functions are not estimated independently. Instead,

within the multivariate framework, each function is iteratively fit to an adjusted response vector (Equation 3.17), so that the estimation is informed by the model's covariance structure.

The MLP function used in other models is a feedforward neural network that can learn complex, nonlinear relationships directly from the data [101]. A single MLP is used with shared hidden layers across all responses. Given the reduced size of the filtered dataset, this design improves data efficiency by enabling the joint learning of common scaling patterns across spectral periods, while period-specific variability is accommodated through the multivariate mixed-effects random effects. Compared to training separate networks for each response, this approach limits over-parameterization and provides a balanced trade-off between model flexibility and robustness under limited data conditions.

The performance of MLP depends strongly on its architecture and hyperparameters, which must be carefully chosen to avoid overfitting and achieve optimal performance. To determine the optimal architecture, a structured hyperparameter search was performed using Bayesian optimization, a sequential model-based strategy that efficiently explores the hyperparameter space. Specifically, the tree-structured Parzen estimator (TPE) sampler was used within the Optuna framework [102], which iteratively builds a probabilistic model of the objective function to guide the search toward promising hyperparameter regions. The search space included the number of hidden layers, neurons per layer, activation function, L2 regularization strength, and initial learning rate. Each candidate configuration was evaluated using 10-fold cross-validation grouped by earthquake events, ensuring that all records from the same event were contained within a single fold. This grouping prevents data leakage and provides a robust estimate of the model's generalization performance.

The optimized MLP architecture, chosen based on average performance across responses, consists of two hidden layers with 6 and 7 neurons, both using hyperbolic tangent (tanh) activation functions. Training was performed using the adaptive moment (Adam) optimizer with an initial learning rate of 2.0×10^{-3}. To prevent overfitting and ensure model generalization, L2 regularization (weight decay) was applied with a penalty parameter of 1.07×10^{-1}. Furthermore, an early stopping mechanism was employed to monitor the validation set and terminate the training process once the validation loss ceased to improve.

To verify the numerical stability of the EM algorithm, the MMER framework was benchmarked against the standard lme4 package in R [75]. The linear model was fitted using both the MMER and lme4 packages across representative spectral periods (0.1 s, 1.0 s, and 4.0 s). Table 3.1 presents this comparison, detailing the estimated fixed-effect coefficients, variance components, and marginal log-likelihood values obtained from both solvers. The absolute differences ("Diff") between the two approaches are negligible across all estimated parameters. This confirms that the proposed multivariate EM algorithm correctly and robustly converges to the standard Maximum Likelihood solution.

Table 3.1. Validation of the MMER numerical optimization against the standard lme4 package in R for representative spectral periods.

Parameters	$SA_{0.1s}$			$SA_{1.0s}$			$SA_{4.0s}$		
	lme4	MMER	Diff	lme4	MMER	Diff	lme4	MMER	Diff
Intercept	-3.208	-3.214	0.005	-3.636	-3.639	0.003	-5.310	-5.314	0.004
M_w	1.492	1.495	0.003	1.381	1.385	0.003	1.627	1.629	0.002
Z_{tor}	0.548	0.554	0.006	0.244	0.248	0.003	0.049	0.053	0.004
ln R_{rup}	-1.143	-1.143	0.001	-0.784	-0.785	0.001	-0.742	-0.744	0.001
ln V_{S30}	-0.161	-0.162	0.000	-0.414	-0.413	0.001	-0.387	-0.388	0.001
F_{m0}	0.286	0.288	0.002	0.594	0.599	0.005	0.203	0.206	0.003
F_{m1}	0.136	0.136	0.000	0.599	0.588	0.011	0.762	0.749	0.013
F_{m2}	-0.041	-0.064	0.023	0.410	0.400	0.010	0.348	0.334	0.013
F_{m3}	0.169	0.165	0.004	0.239	0.237	0.002	0.012	0.011	0.002
Between-event	0.565	0.570	0.006	0.302	0.303	0.001	0.235	0.233	0.002
Between-site	0.180	0.168	0.012	0.189	0.177	0.012	0.213	0.202	0.010
Residual	0.456	0.473	0.016	0.264	0.280	0.016	0.221	0.236	0.015
Log-Likelihood	-3845.246	-3844.590	0.656	-3226.632	-3226.440	0.192	-3099.941	-3100.060	0.119

3.5. Model Results and Physical Interpretation

3.5.1. Overall Model Performance

This section evaluates the predictive performance of the fixed-effects component across all models. For brevity, the following abbreviations are used: linear-based model (LR), MLP with random intercepts only (MI), and MLP with random intercepts and slope (MS). The test set includes earthquakes not seen during training due to the event-based data split, so the random effects for these new events are unknown. Consequently, the model's generalization capability depends entirely on its fixed-effects component, providing an unbiased assessment of predictive power.

Table 3.2 presents four performance metrics for each model, averaged over all SA values for both training and test sets. Figure 3.2 shows the same metrics for the 40 individual SA values, but only for the test set. The metrics are the coefficient of determination (R^2), Pearson correlation coefficient (r), mean absolute error (MAE), and root mean squared error (RMSE). Although probabilistic scoring rules (e.g., log-likelihood, Bayesian Information Criterion, etc.) are commonly used to rank production GMMs, the focus here is placed on median-based metrics to directly assess the generalization performance of the fixed-effects component. This choice allows the evaluation of mean predictive trends to be isolated from the variance and correlation structure, which are examined separately in subsequent sections. It should be noted, however, that all model parameters are estimated by maximizing the marginal log-likelihood (Equation 6), ensuring that the full predictive distribution is statistically optimized and internally consistent.

According to Table 3.2, the MI and MS approaches yield a test R^2 of approximately 0.70 and 0.69, respectively, compared to 0.58 for the LR model. The modest gap between training and testing performance is expected and can be attributed to two factors: (1) the reduced dataset resulting from filtering records based on maximum usable period criteria, which limits the information available for training, particularly for ML models that are not guided by explicit physical constraints; and (2) the intentionally simplified structure of the linear benchmark model, which omits nonlinear transformations commonly employed in GMMs.

However, each model's performance varies across spectral periods. In the low period range (0.09–0.2 s), all models show reduced R^2 and r values along with higher errors, reflecting the difficulty of predicting short-period (high-frequency) ground motions. This difficulty arises partly because high-frequency components are more affected by small-scale heterogeneities in the source and propagation path, leading to greater dispersion and noisier signals [100]. Performance improves at intermediate periods (0.2–2.0 s), where spectral acceleration patterns are more coherent and less sensitive to such heterogeneities. At long periods, the LR model's performance declines, likely because its simplified fixed functional form cannot fully capture complex attenuation and perhaps basin effects. In contrast, the MI and MS models maintain relatively stable performance up to 10 s. This reflects the flexibility of the nonparametric MLP, which can adjust to complex scaling behavior at long periods, rather than implying intrinsic superiority.

Table 3.2. Average model performance across all SA values.

	LR		MI		MS	
Metrics	Training	Test	Training	Test	Training	Test
R^2	0.766	0.582	0.835	0.704	0.808	0.694
r	0.914	0.860	0.940	0.896	0.932	0.892
MAE	0.667	0.788	0.577	0.672	0.615	0.669
RMSE	0.869	0.990	0.734	0.839	0.794	0.848

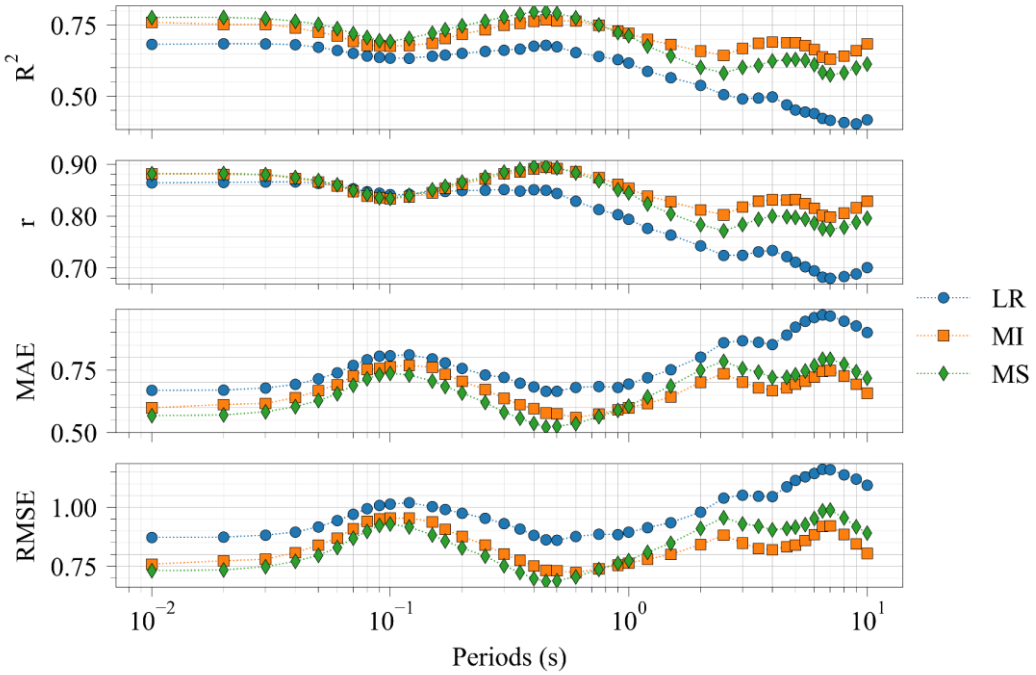


Figure 3.2. Performance metrics using the test set for SA values across spectral periods.

It is noteworthy that a comparison between the proposed joint multivariate estimation and separate univariate estimation is not presented for these performance metrics. Under the assumed mixed-effects model, when the design matrices are identical across all response variables (as is the case here), the fixed-effects estimates (medians) obtained from joint multivariate regression are asymptotically equivalent to those obtained from separate univariate regressions. Consequently, the joint estimation is not expected to materially change the median predictions reported in Table 3.2. Its primary advantage lies instead in the simultaneous estimation of the covariance structure (discussed in Section 3.5.2), which accounts for the correlation among model parameters and is not captured by separate univariate regressions.

Figure 3.3 further illustrates a direct visual comparison between predicted and actual values (in natural logarithms) for three representative SA values: $SA_{0.1}$ (short period), $SA_{1.0}$ (intermediate period), and $SA_{4.0}$

(long period). The data generally follows the 1:1 line, though some scatter is evident, reflecting the moderate predictive performance of the models. Under the current modeling choices and dataset limitations, the MI and MS models generally show higher R^2 and r values and lower errors than the simplified LR model across all periods, indicating comparatively better predictive performance.

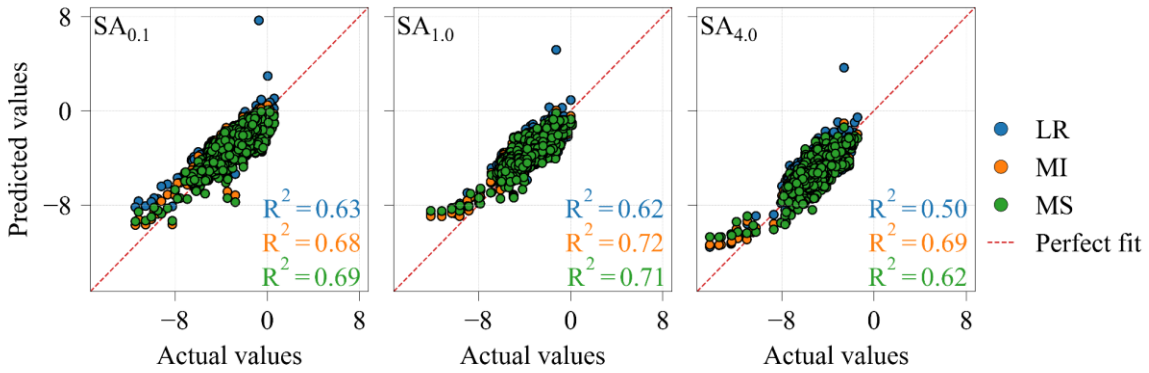


Figure 3.3. Predicted versus actual values for $SA_{0.1}$, $SA_{1.0}$, and $SA_{4.0}$ using the test set.

To verify that the MLP models learned physically meaningful relationships, the importance of each predictor is assessed using Shapley additive explanations (SHAP), a unified, model-agnostic framework from cooperative game theory [103]. Figure 3.4 presents the relative mean absolute SHAP values, which quantify the average impact of each feature on the model's response value. While the LR model identifies M_w as the dominant predictor, the MLP models (MI and MS) attribute the highest importance to R_{rup}, followed by M_w. Secondary parameters such as V_{S30}, Z_{tor}, and F_m show a smaller but consistent impact across all models. This shift in predictor importance is physically interpretable. In the LR model, the fixed functional form enforces constant magnitude scaling, even in ranges where magnitude saturation occurs. In contrast, the MLP models appear to capture saturation effects, increasing the relative weight of distance attenuation (R_{rup}). This ranking also reflects characteristics of the filtered dataset. Because enforcing long-period usability reduces the number of small-magnitude records, the remaining dataset is dominated by moderate-to-large events, where magnitude saturation naturally plays a more pronounced role.

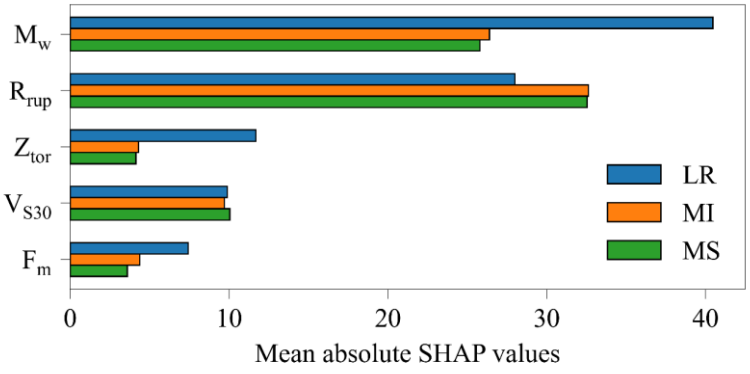


Figure 3.4. Feature importance using SHAP values.

Beyond feature importance, the statistical stability of these learned relationships is also assessed. Using a nonparametric cluster bootstrapping approach, in which earthquake events are repeatedly resampled 100 times with replacement (see the subsequent section for details), the epistemic uncertainty surrounding the fixed-effects estimation is quantified. Figure 3.5 presents the 95% confidence intervals for the median predicted spectral acceleration across a representative rupture scenario (M_w=7.0, Z_{tor}=1 km, R_{rup}=10 km, V_{S30}=760 m/s, and Strike-slip fault mechanism). The narrow confidence bands indicate that the non-linear scaling learned by the MLP components is robust and well-constrained by the data, even without a rigid functional form.

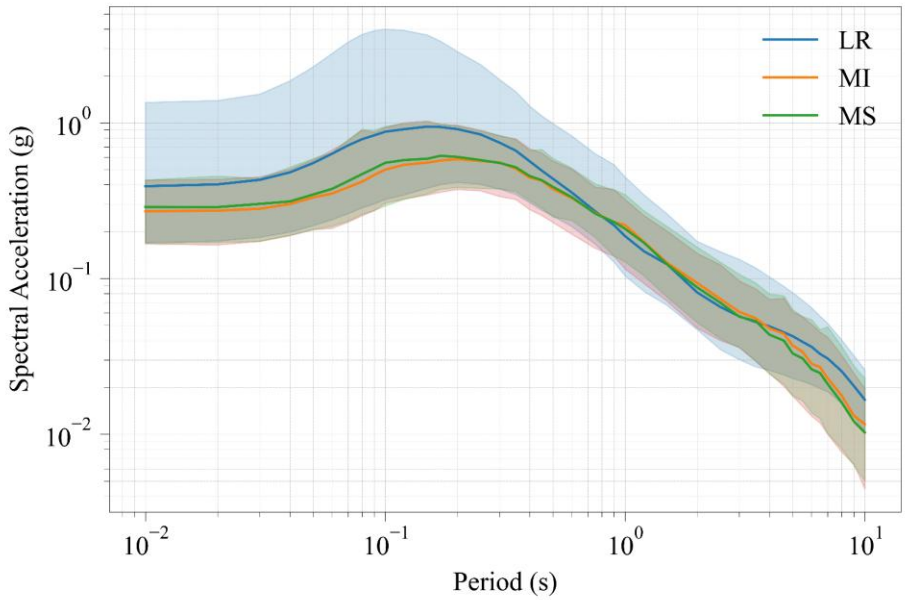


Figure 3.5. Epistemic uncertainty in the median predicted spectral acceleration for a scenario event (M_w=7.0, Z_{tor}=1 km, R_{rup}=10 km, V_{S30}=760 m/s, and Strike-slip fault mechanism) using the LR, MI, and MS models. Solid lines denote the median predictions, and shaded ribbons denote the corresponding 95% confidence intervals obtained from nonparametric cluster bootstrapping (100 iterations).

3.5.2. Analysis of Variance

To assess the uncertainty structure of models, Figure 3.6 shows the standard deviation (SD) of between-event, between-site, and residual components across spectral periods for all models. For clarity, uncertainty bounds are shown separately in Figure 3.7, which reports 95% confidence intervals for the between-event SD obtained via nonparametric cluster bootstrapping (resampling events). This uncertainty analysis is intentionally limited to the source-related variability. Event-level resampling provides a statistically reliable way to evaluate the stability of the event terms, but it does not preserve the station-level sampling needed for stable estimation of between-site variability. For this reason, confidence intervals are reported only for the between-event component, where the bootstrap procedure remains unbiased.

It is noteworthy that standard deviations in Figure 3.6 represent global variance components estimated by pooling information across the entire dataset. Although the dataset includes events or stations with single recordings (where separating random effects from residuals is not identifiable in isolation), the mixed-effects formulation leverages the well-sampled groups to robustly estimate these global variances. For singleton events or stations, the best linear unbiased predictor (BLUP) in Equation 3.12 uses the globally estimated variance components to apportion the total residual. Due to the shrinkage mechanism, which naturally exerts a stronger influence when data is sparse, the predicted random effects for the levels of such groups are pulled toward the global mean. Consequently, while the posterior uncertainty (Equation 3.13) for these specific estimates is naturally high, their presence does not destabilize the global variance partitioning shown in Figure 3.6. For applications that require reliable inferences of event- or station-specific random effects, it is recommended to impose a minimum number of recordings per group level (e.g., 3–5 recordings, as is standard in production GMMs). While this chapter focuses on estimating global variance components to demonstrate the robustness of the MMER framework, these group-specific inference requirements are addressed in the integrated generative framework presented in Chapter 4.

Although the LR and MI models share the same random-effects structure, they differ in how uncertainty is distributed. Because the MLP is a nonparametric model, it can automatically capture complex physical patterns (e.g., magnitude saturation) that were not explicitly formulated in the simplified LR model. As a

result, more variability is accounted for upfront, leaving less to be allocated to random effects or residuals. By contrast, the LR model, which does not include these non-linear scaling terms, leaves additional variability unmodeled, resulting in relatively larger between-event and between-site variance estimates. It is noteworthy that employing a more sophisticated parametric formulation (e.g., including magnitude-dependent geometric spreading as in [51,53,100]), could similarly reduce this unexplained variability. However, the purpose of this comparison is to illustrate the MMER framework's flexibility rather than to advocate for any particular modeling approach.

The between-site standard deviation (SD) exhibits period-dependent difference between the two modeling approaches. At short periods (<0.3 s), the LR model yields higher between-site SD than the MI model. This suggests that the simple linear formulation, which lacks explicit non-linear site amplification terms, cannot account for the local heterogeneities that influence high-frequency motions, whereas the data-driven MI model was able to approximate these behaviors automatically, leading to reduced variability. At longer periods (>0.3 s), both models yield similar between-site SDs, reflecting the dominance of source and path effects, where the MLP's advantage over the LR in reducing variability is less pronounced.

The MI and MS models share the same MLP fixed-effects component but differ in their random-effects structure, with the MS model including an additional random slope for M_w in the between-event term. While Figure 3.6 shows the MS model for M_w=7.0, analysis across all M_w values reveals a consistently lower between-site SD and a correspondingly higher residual SD compared to the MI model. This indicates that the more flexible random-effects structure in the MS model recognizes that not all variability attributed to the between-site term by the simpler MI model arises from persistent, systematic site effects. This behavior can be expected because certain source characteristics (e.g., high stress-drop asperity) may influence shaking only at a subset of stations. The simpler MI model, unable to account for such effects, may over-attribute this variability to the between-site term, inflating its variance. In contrast, the M_w-dependent between-event term in the MS model captures this source effect more effectively, and any variability that it cannot explain is subsequently reallocated to the residual term.

A notable feature in Figure 3.6 is the increase in total SD around a period of 0.1 s, primarily driven by the between-event term. This behavior has also been observed in previous studies [51,100]. While often attributed to source effects, Chiou and Youngs [51] suggest that this short-period peak may partly reflect between-site variability; in their analysis, explicitly modeling site-specific random effects shifted much of the observed peak to the between-site component of the within-event SD, particularly for California data and small-to-moderate magnitude events. This indicates that the peak occurs partly because high-frequency components are more affected by small-scale heterogeneities in the source and propagation path, leading to greater dispersion [100]. The observed increase in the between-event SD toward long periods can be physically expected as ground motion SA's variability becomes increasingly dominated by earthquake source characteristics, which naturally increases the between-event component of uncertainty.

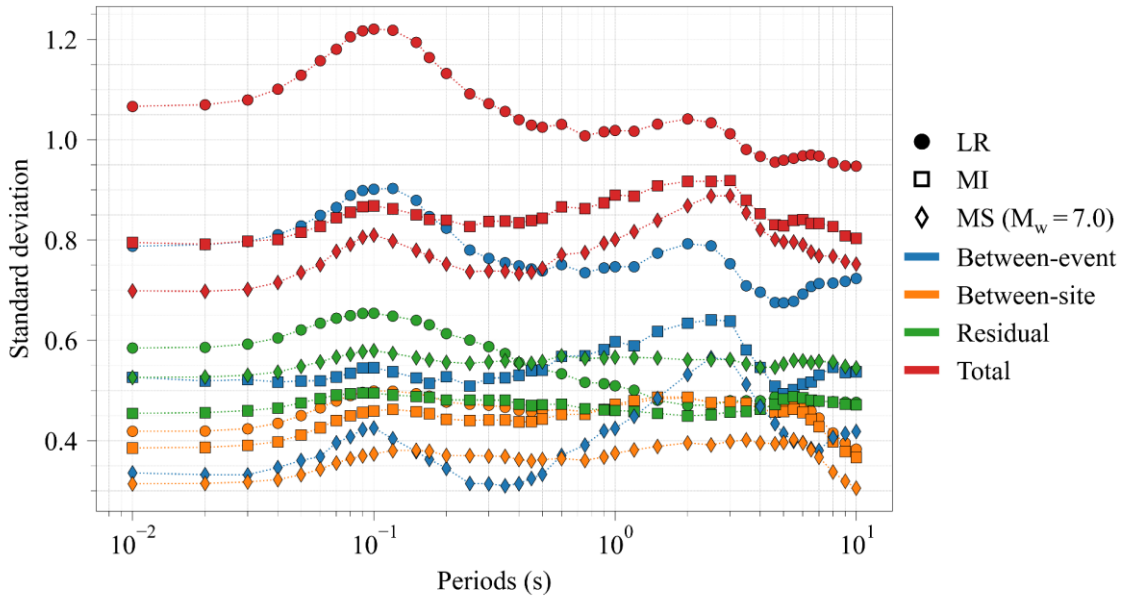


Figure 3.6. Maximum likelihood estimates of the standard deviation of different aleatory components across spectral periods.

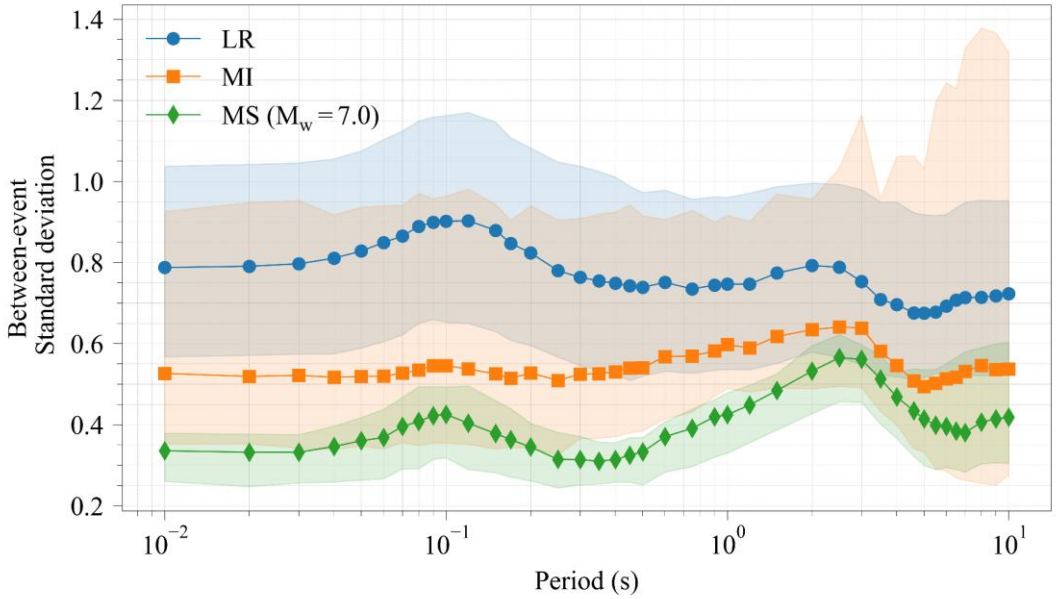


Figure 3.7. Between-event standard deviation along with 95% confidence intervals derived from non-parametric cluster bootstrapping (100 iterations).

Figure 3.8 illustrates the M_w-dependent between-event SD for only the three representative SA values. Analysis shows that this nonmonotonic trend occurs for all SA values. Consistent with conventional GMMs (e.g., [51,53,100]), the between-event SD initially decreases as M_w increases from small to moderate values (e.g., M_w <7.0). This decay is widely attributed to the variation in the source stress parameter, which is more pronounced in smaller earthquakes than in larger ones. However, in contrast to rigid parametric forms that typically assume a constant variability at large magnitudes, the data-driven MS model reveals that the SD increases again at larger magnitudes (e.g., M_w >7.0). This behavior may reflect the influence of complex rupture dynamics (such as slip heterogeneity and directivity) that become significant for large events. Unlike previous studies that assumed a monotonically decreasing function (e.g., [51,53,100]), the proposed framework imposes no pre-defined functional form, allowing the MS model to learn this nuanced, dual-regime dependency directly from the data. It is important to note that

while this trend is physically plausible, the specific shape is conditioned on the characteristics of the dataset used in this chapter. The nonmonotonic uncertainty trend reflects the behavior learned from the selected subset of the NGA-West2 database. The key finding, however, is that the inclusion of a random slope in the framework provided the necessary flexibility to capture this complex behavior, a feature that is often obscured in models constrained by rigid functional forms.

To assess the statistical significance of the observed trend, a nonparametric cluster bootstrap analysis was performed. 100 resampled datasets were generated by resampling earthquake events with replacement, preserving the within-event correlation structure. The MS mixed-effects model was re-trained on each resampled dataset. The shaded regions in Figure 3.8 represent the 95% confidence intervals derived from the 2.5th and 97.5th percentiles of the bootstrap distribution. The results confirm that the increase in between-event variability at large magnitudes ($M_w > 7.0$) is a robust feature of the dataset and not an artifact of sampling instability.

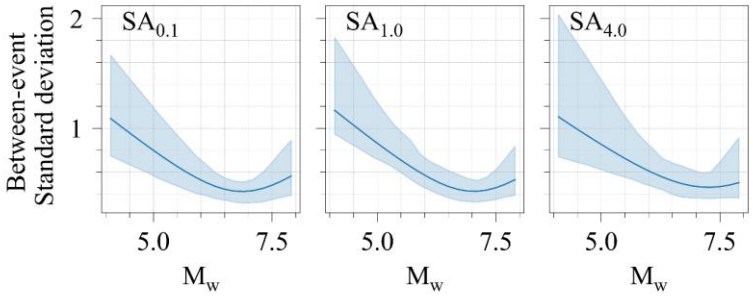


Figure 3.8. Variation of the between-event standard deviation with M_w. The solid line represents the final models estimate, and the shaded region indicates the 95% confidence interval from nonparametric cluster bootstrapping.

Next, residual analysis was performed to assess the models' assumptions and the existence of any potential systematic biases. Figure 3.9 shows the variation of residuals with R_{rup} for the three representative SA values. The binned means and their associated SD on top of the raw scatter data were overlaid. The random scatter of points, combined with the stability of the binned means around zero, indicate no systematic bias with distance attenuation. Likewise, the between-site random-effects variation with V_{S30}, as shown in Figure 3.10, reveals no discernible trend for the data, indicating that the site term of the fixed-effects sufficiently captures the average site response.

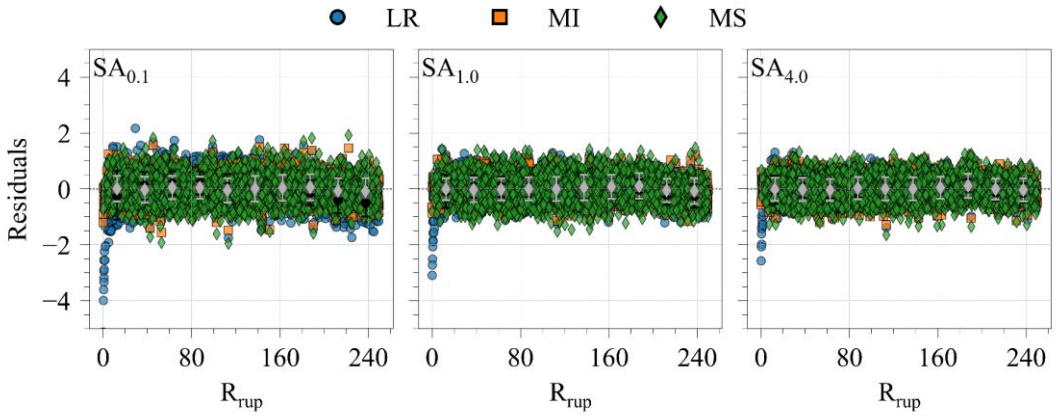


Figure 3.9. Variation of unexplained residuals with R_{rup}.

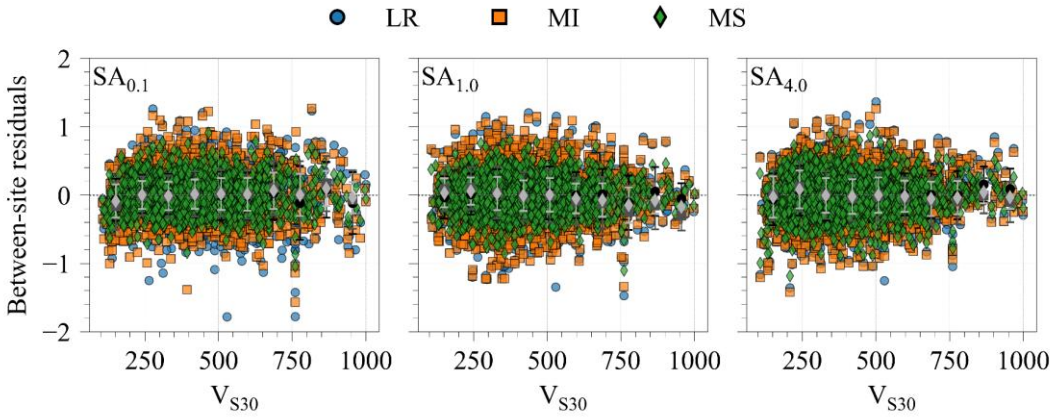


Figure 3.10. Variation of between-site residuals with V_{S30}.

The analysis of between-event terms against the source parameters reveals the progressive improvement of the modeling framework across LR, MI, and MS models, as shown in Figure 3.11 to Figure 3.13 for M_w, Z_{tor}, and F_m, respectively. In the LR and MI models, a discernible systematic trend is evident, particularly at the lower bound of the magnitude range (M_w < 5.0), where residuals show a negative bias and larger dispersion. This suggests that a fixed functional form (i.e., LR) or a simple random-intercept structure (i.e., MI) may be insufficient to fully capture the magnitude-scaling of source effects across the entire dataset. In contrast, the MS model, which incorporates an M_w-dependent random slope, substantially mitigates this systematic deviation. As shown in the green markers in Figure 3.11, the residuals for the MS model exhibit tighter clustering and a more centered distribution around zero compared to the LR and MI baselines. However, some scatter remains, preventing a perfect collapse of residuals to zero. This remaining spread likely reflects a combination of unmodeled source-related variability that is not fully explained by M_w and the limitations associated with the reduced dataset size. Because unconstrained ML models rely on high data density to resolve subtle non-linear interactions, the strict filtering applied to this dataset, while necessary for long-period validity, restricts the model's capacity to fully constrain the aleatory variability at the edges of the parameter space.

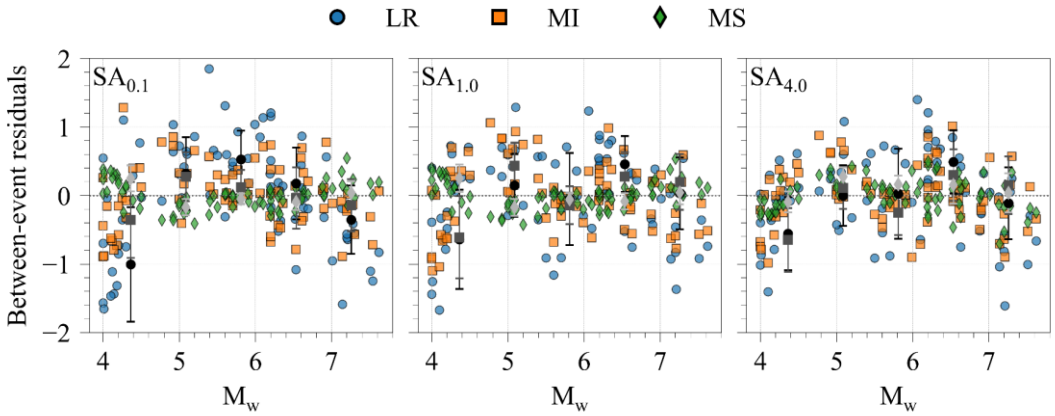


Figure 3.11. Variation of total effective between-event residuals with M_w. For the MS model, this includes the effective sum of the random intercept and the random slope components.

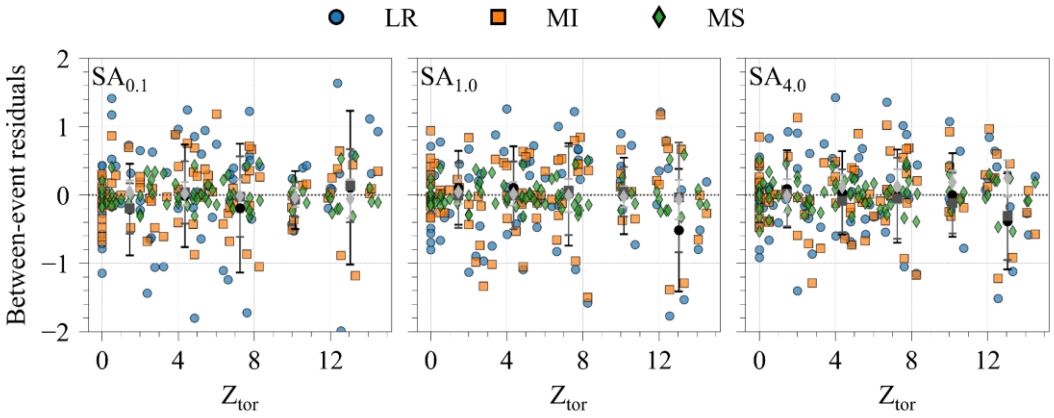


Figure 3.12. Variation of total effective between-event residuals with Z_{tor}. For the MS model, this includes the effective sum of the random intercept and the random slope components.

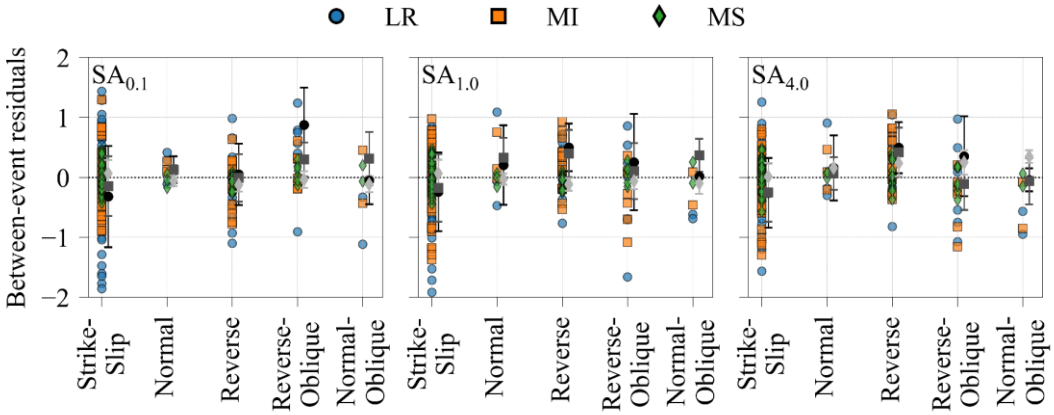


Figure 3.13. Variation of total effective between-event residuals with F_m. For the MS model, this includes the effective sum of the random intercept and the random slope components.

To validate the full multivariate structure of the framework, the model-implied total correlation matrix was derived by converting the covariance matrix (i.e., Equation 3.5) accordingly. Figure 3.14 compares the total correlation coefficient across all models for three representative SA values at periods 0.1, 1.0, and 4.0 s against the established empirical models (Baker and Jayaram, 2008; Baker and Bradley, 2017 [59,60]). The solid lines represent the final models, while the shaded region around the MS model indicates the 95% confidence interval derived from the nonparametric bootstrap analysis. For visual clarity, the corresponding uncertainty quantification for the MI and LR models is provided separately in Figure 3.15 and Figure 3.16, respectively. The analysis reveals a distinct stratification in model behavior. The MS model (evaluated at M_w=7.0) exhibits strong agreement with the empirical benchmarks. The MS model shows a M_w-dependent correlation that increases for M_w above or below seven. The MI model yields correlation estimates that fall between those of the MS and LR models. While it improves upon the LR model, it tends to overestimate correlations relative to empirical benchmarks, particularly at short periods. In contrast, the LR model consistently over-predicts the correlation across all periods. This is an expected consequence of its simple functional form, where unmodeled non-linear variability is aliased into the model's covariance structure.

Because the framework directly estimates the full covariance matrix, it produces inter-period correlations that are smooth and physically coherent, rather than treating each spectral period as an independent outcome. This consistency is crucial for applications such as vector-valued or conditional-spectrum PSHA, which require a reliable inter-period covariance structure. In contrast, univariate approaches typically rely on post-hoc correlation modeling. The practical value of this natively

extracted covariance structure is fully realized in Chapter 4, where it directly enables the conditional simulation of hazard-compatible, three-component ground motions.

Overall, this evaluation shows that the added flexibility in the MS model within the framework improves its ability to represent the uncertainty structure of SA across different periods.

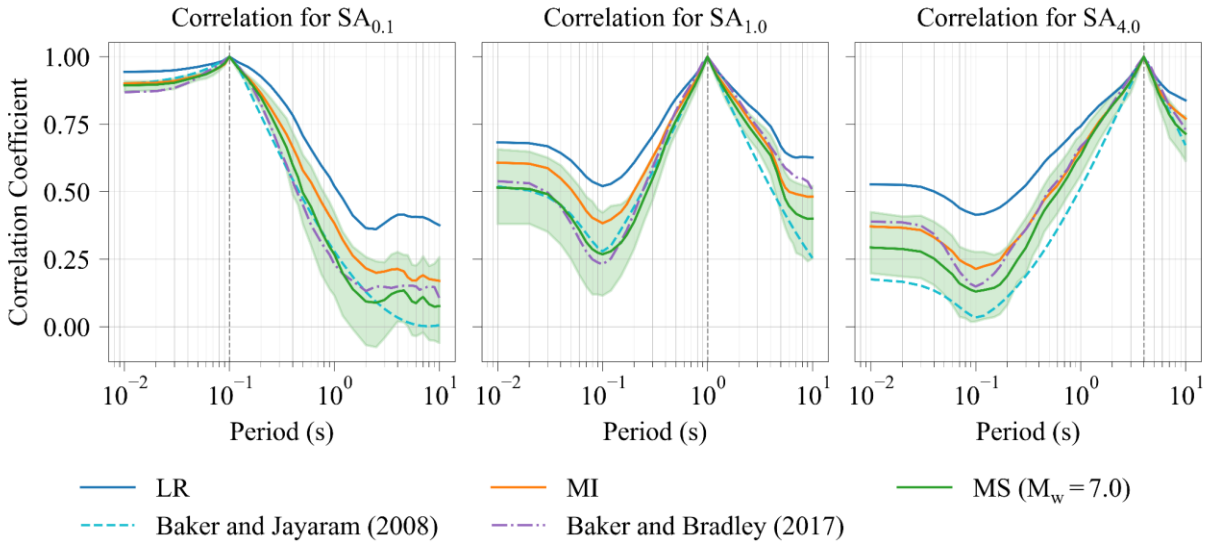


Figure 3.14. Variation of the maximum likelihood estimates of total correlation coefficients for $SA_{0.1}$, $SA_{1.0}$, and $SA_{4.0}$ across spectral periods. The solid line represents the final models estimate, and the shaded region indicates the 95% confidence interval derived from nonparametric cluster bootstrapping for the MS model.

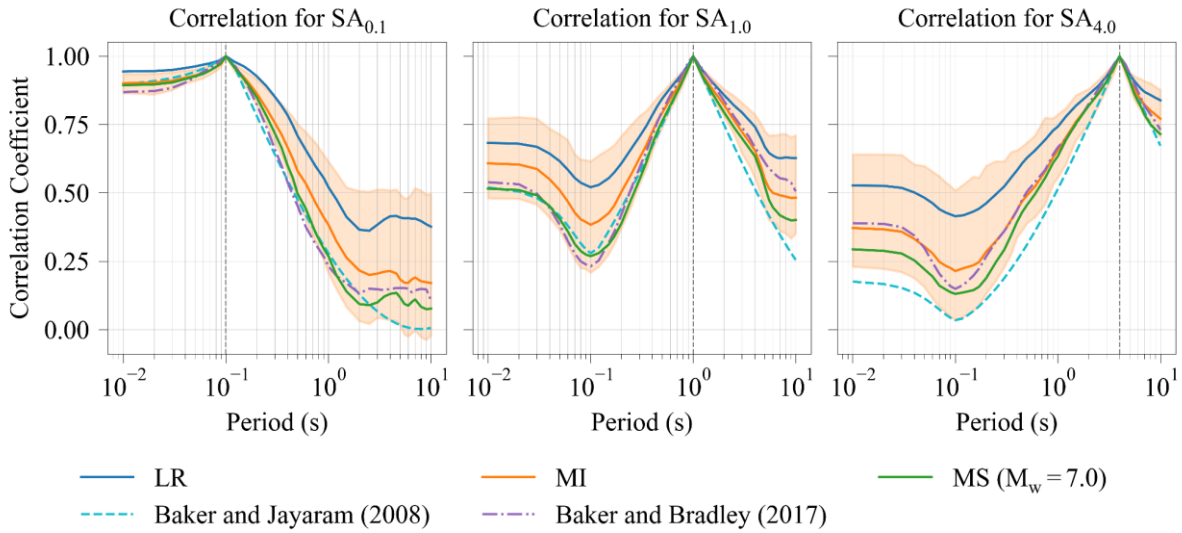


Figure 3.15. Variation of the maximum likelihood estimates of total correlation coefficients for $SA_{0.1}$, $SA_{1.0}$, and $SA_{4.0}$ across spectral periods. The solid line represents the final models estimate, and the shaded region indicates the 95% confidence interval derived from nonparametric cluster bootstrapping for the MI model.

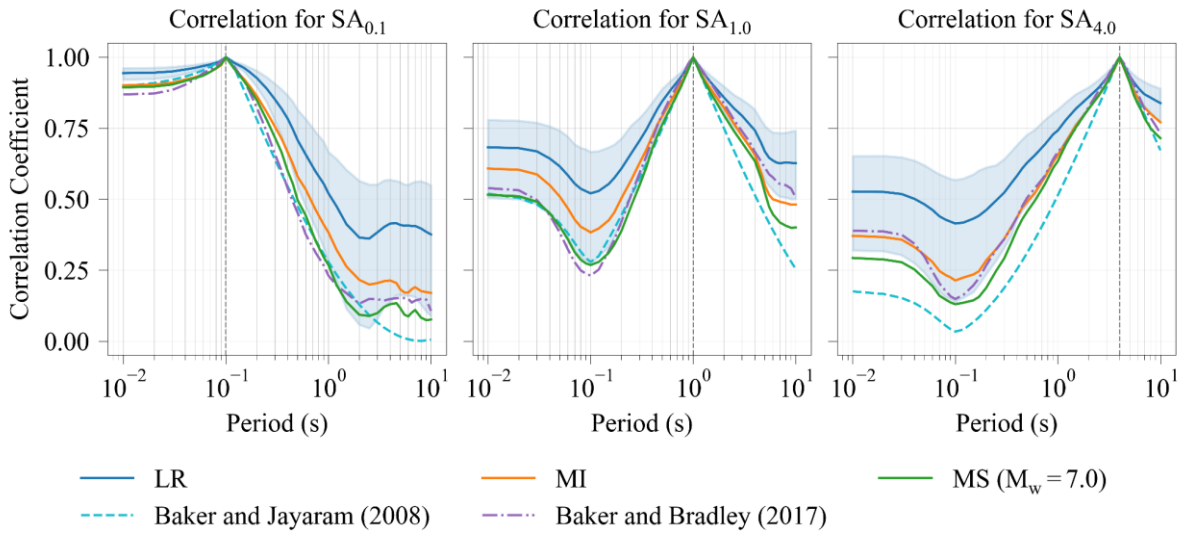


Figure 3.16. Variation of the maximum likelihood estimates of total correlation coefficients for $SA_{0.1}$, $SA_{1.0}$, and $SA_{4.0}$ across spectral periods. The solid line represents the final models estimate, and the shaded region indicates the 95% confidence interval derived from nonparametric cluster bootstrapping for the LR model.

Figure 3.17 to Figure 3.19 illustrate the predicted median SA at periods of 0.1, 1.0, and 4.0 s from the LR and MI models as a function of M_w and R_{rup}. Results from the MS model are not shown, as its fixed-effects component is similar to that of the MI model. The left panels of the figures show the magnitude scaling. As expected, predicted SA values increase with M_w, with the MI model capturing nonlinear behaviors, including the tendency for scaling to saturate at large M_w. The plots also illustrate the effect of Z_{tor}. In the LR model, a deeper depth to the top of rupture is associated with higher predicted SA at short periods ($SA_{0.1}$). This effect gradually diminishes at longer periods ($SA_{4.0}$). In contrast, the ML model exhibits substantial overlap and reduced sensitivity to Z_{tor}. This behavior reflects the data-driven nature of the ML model and the absence of explicit functional constraints beyond those imposed by the training dataset.

The right panels show the distance scaling (i.e., the attenuation of SAs with R_{rup}). All models correctly capture the expected decrease in amplitude with distance due to geometric spreading and anelastic attenuation. The LR model, which uses a simple logarithm of R_{rup}, tends to overpredict amplitudes at very close distances and exhibits a steep attenuation as distance increases. While this limitation is typically resolved in conventional GMMs by explicitly formulating a magnitude-dependent fictitious depth term (e.g., $\sqrt{R_{rup}^2 + C^2}$ [53]), the simple form was retained to demonstrate the framework's adaptability to different fixed-effects models.

Crucially, the MI model, due to its inherent flexibility, automatically learns this complex near-fault scaling behavior directly from the data without requiring the user to pre-define the geometric saturation function. This demonstrates the ability of the data-driven approach to capture physically realistic patterns even when the underlying functional form is not explicitly provided.

Furthermore, the models capture site amplification, with SA commonly decreasing as V_{S30} increases. This indicates that in general softer soil sites experience stronger shaking than stiffer, rock-like sites, and the effect becomes more pronounced at longer periods. Collectively, these figures demonstrate that the models developed within the proposed multivariate framework have learned the fundamental scaling relationships that are consistent with seismological principles, with the MLP model better capturing the complex nonlinear behaviors.

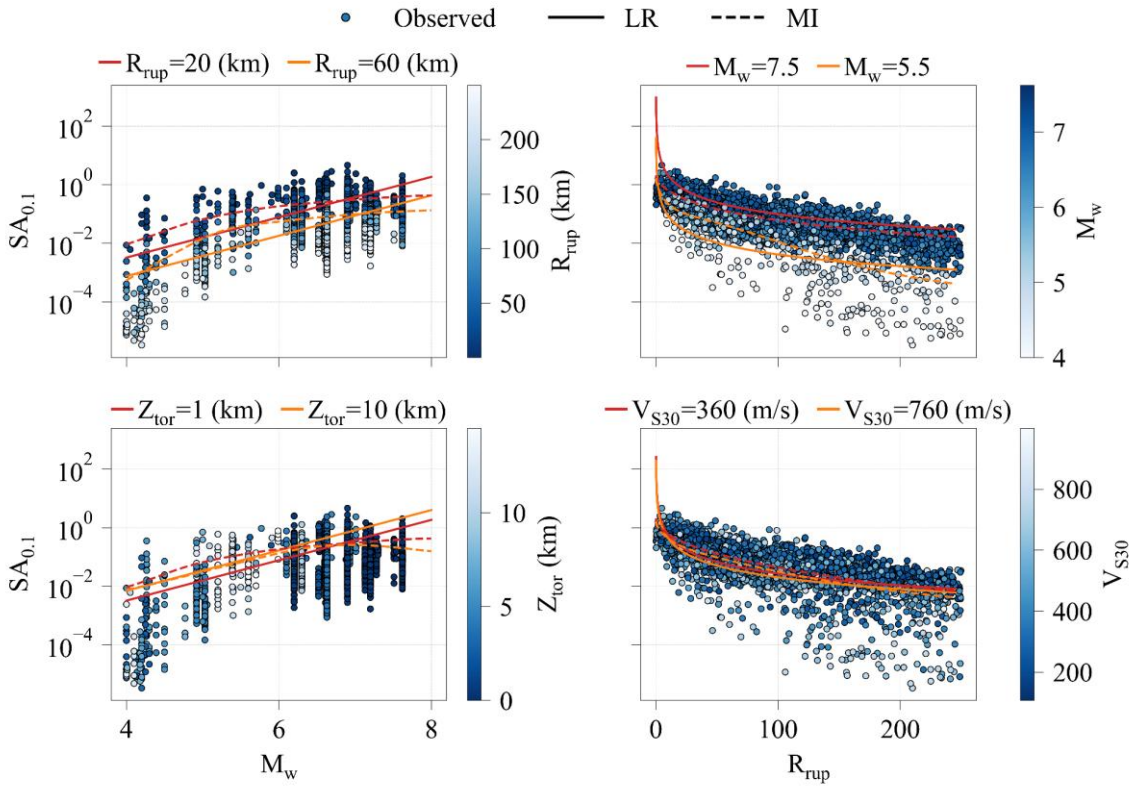


Figure 3.17. Scaling relationships for $SA_{0.1}$ with different seismological parameters. Default values for unspecified parameters are Z_{tor}=1 km, V_{S30}=760 m/s, R_{rup}=20 km, M_w=6.5, and a strike-slip fault mechanism.

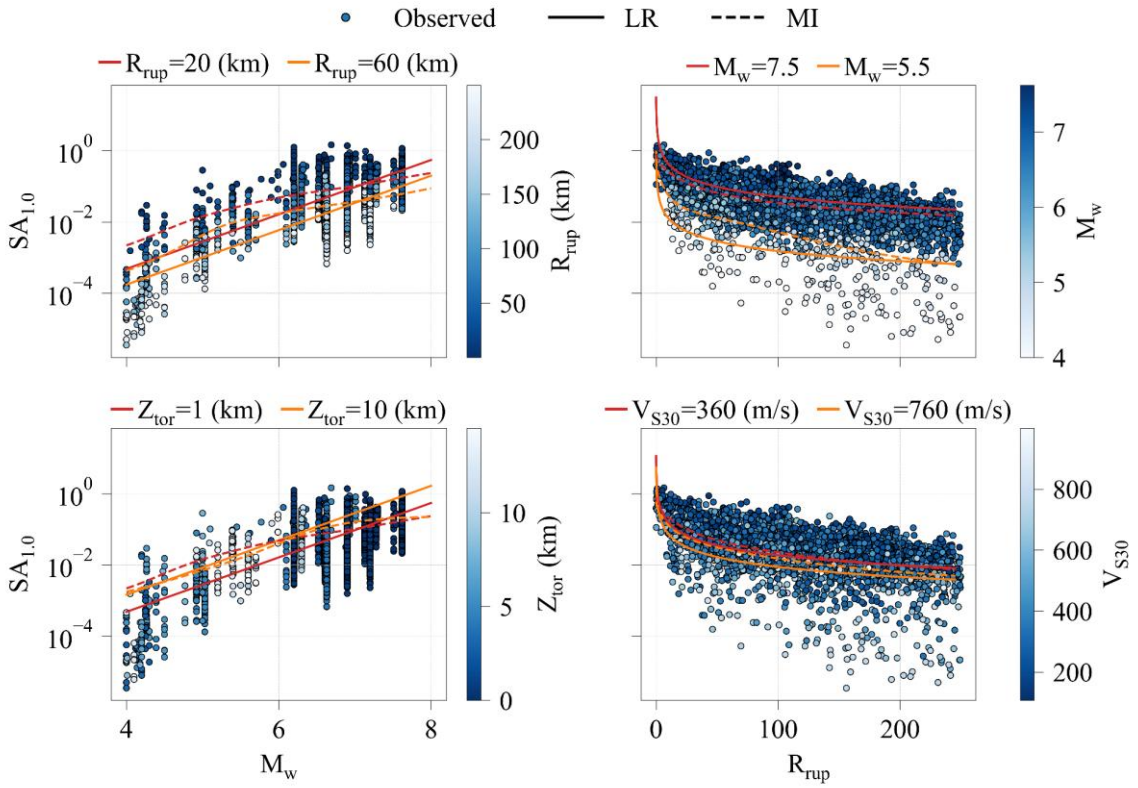


Figure 3.18. Scaling relationships for $SA_{1.0}$ with different seismological parameters. Default values for unspecified parameters are Z_{tor}=1 km, V_{S30}=760 m/s, R_{rup}=20 km, M_w=6.5, and a strike-slip fault mechanism.

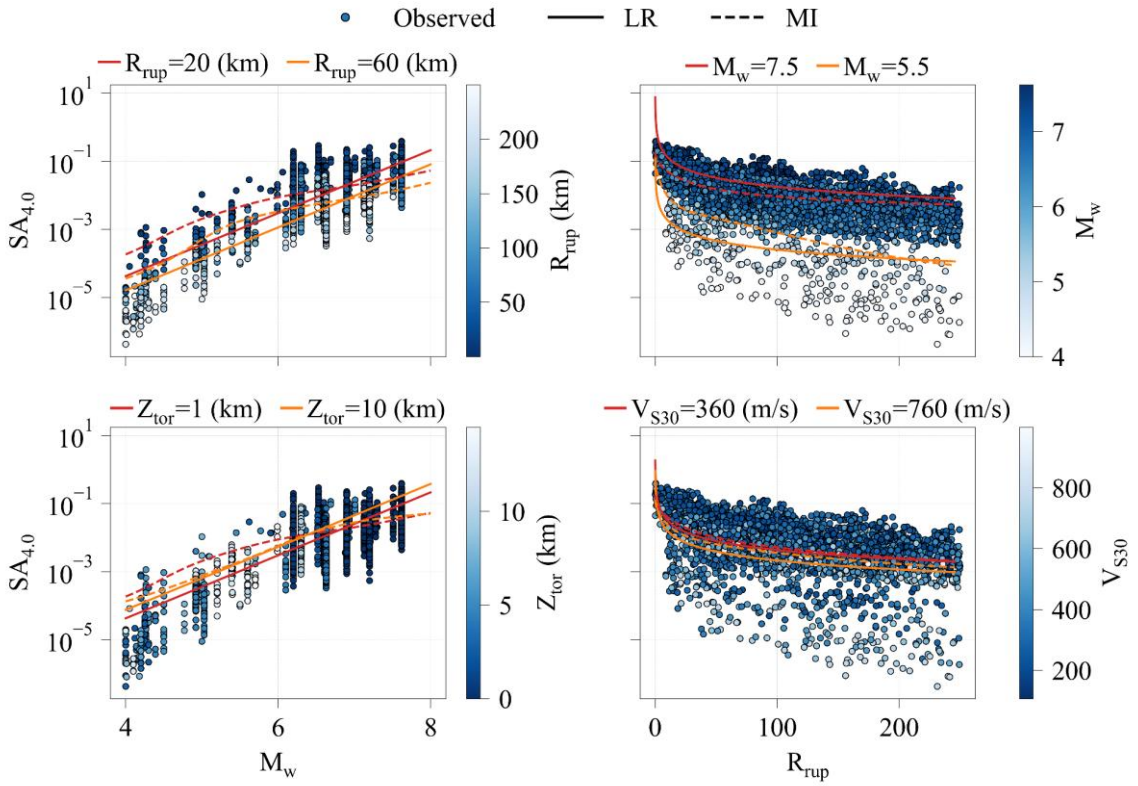


Figure 3.19. Scaling relationships for $SA_{4.0}$ with different seismological parameters. Default values for unspecified parameters are Z_{tor}=1 km, V_{S30}=760 m/s, R_{rup}=20 km, M_w=6.5, and a strike-slip fault mechanism.

While the ML-based models demonstrate flexibility in capturing non-linear trends, it is important to acknowledge a specific vulnerability of this data-driven approach. Unlike parametric models, which impose a global functional form (ensuring, for example, that distance attenuation follows a similar decay rate across all site categories), nonparametric methods can inadvertently learn spurious interactions in regions of the parameter space where data is sparse or unevenly distributed. To evaluate whether such effects are present, the scaling plots in Figure 3.17 to Figure 3.19 serve as a critical diagnostic. The stable trends and consistent distance attenuation slopes observed across different V_{S30} values suggest that the model has successfully captured a baseline of physical interactions without clear data artifacts. However, ensuring strict compliance with physical laws under all data constraints requires architectural ML constraints, providing a direct motivation for the integrated, physics-informed framework presented in the next chapter.

3.6. Conclusions

This chapter introduced a multivariate mixed-effects regression (MMER) framework for ground motion model development within a unified statistical structure. The framework enables consistent estimation of the full uncertainty decomposition, including between-event, between-site, and residual components, while allowing flexible fixed-effects specifications ranging from parametric formulations to data-driven functional representations.

Validations demonstrated that the embedded machine learning components captured nonlinear scaling behaviors, such as magnitude saturation, directly from the data without requiring rigid pre-defined functional forms. Furthermore, by integrating nonparametric cluster bootstrapping, the framework enables quantification of epistemic uncertainty in both median predictions and variance structures required for probabilistic seismic hazard analysis.

Building on this statistical foundation, the next step is to operationalize the MMER framework to predict the parameters of the stochastic simulation method derived in Chapter 2. To address this, Chapter 4 integrates these statistical and physical methodologies, culminating in a unified framework capable of generating hazard-compatible, three-component conditional ground motion simulations.

Chapter 4
Hazard-Compatible Three-Component Stochastic Simulation

> *The contents of this chapter are based on a manuscript that was submitted for publication and was still under review at the time of thesis submission. Minor formatting and structural modifications have been made to align with the overarching thesis narrative.*

4.1. Introduction

The developments presented in Chapters 2 and 3 address two complementary but historically disconnected challenges in earthquake engineering. Chapter 2 focused on the generation of realistic earthquake ground motion time-series through an enhanced broadband stochastic simulation methodology, while Chapter 3 introduced a unified multivariate mixed-effects regression framework for jointly modeling correlated response variables and their associated uncertainty structure. Although each component addresses an important methodological problem on its own, a key gap remains in connecting probabilistic intensity measures (IMs) with the generation of physically consistent, three-component (3C) ground motion time-series. Achieving the objectives of performance-based earthquake engineering (PBEE) ultimately requires these elements to be integrated within a unified framework capable of generating hazard-compatible synthetic ground motions directly from prescribed seismic scenarios.

In conventional practice, hazard analyses typically operate in terms of IMs, whereas simulation methodologies operate in terms of internal model parameters. As a result, hazard information cannot be directly propagated into the simulation process without introducing additional intermediate procedures.

This chapter addresses this gap by integrating the methodologies developed in Chapters 2 and 3 into a single probabilistic framework. The central idea is to treat both important IMs and stochastic simulation parameters as components of a unified multivariate statistical system. By modeling these quantities jointly, information contained within target hazard-consistent IMs can be propagated through the covariance structure of the model to infer the corresponding stochastic simulation parameters required for waveform generation.

Within the proposed framework, the fixed-effects component is represented using a physics-informed neural additive model (NAM), in which separate neural networks are assigned to individual seismological predictors. In contrast to conventional black-box neural network formulations, this structure allows for partial interpretability while enforcing physically motivated monotonicity constraints that reflect expected scaling behavior in ground motions.

A key feature of the proposed formulation is its ability to perform conditional simulation using standard results from multivariate normal theory. This enables one or more target hazard-consistent IMs to be specified explicitly, while the conditional distributions of all remaining IMs and simulation parameters are inferred in a statistically consistent manner. The resulting parameter realizations can then be propagated through the stochastic simulation engine developed in Chapter 2 to generate complete 3C ground motion time-series.

Overall, the proposed framework establishes a direct link between seismic hazard characterization and synthetic waveform generation. In contrast to traditional workflows that rely on historical seed records, record-selection procedures, spectrum matching, or iterative adjustment processes, the present approach generates hazard-compatible 3C ground motions directly from prescribed hazard conditions while preserving physically meaningful dependence structures among waveform characteristics. This provides

a coherent and computationally efficient alternative for applications requiring large suites of statistically consistent synthetic ground motions.

4.2. Ground Motion Dataset and Parameter Extraction

4.2.1. Dataset Selection and Intensity Measures

As introduced in Chapter 3, this research uses a filtered subset of the NGA-West2 database. The dataset was further filtered to focus on crustal earthquakes with engineering importance using the following criteria:

- **Magnitude-Dependent Distance:** To maintain a high signal-to-noise ratio, the maximum rupture distance (R_{rup}) was constrained based on moment magnitude (M_w) using an approach similar to established empirical models (e.g., [100]): 80 km for $4.5 \leq M_w < 5.0$, 150 km for $5.0 \leq M_w < 5.5$, and a maximum of 300 km for $5.5 \leq M_w$.
- **Source and Site Parameters:** Events were restricted to shallow crustal seismicity with depth to top of rupture (Z_{tor}) of 15 km or less ([83]) and sites with time-averaged shear-wave velocity in the top 30 meters of soil (V_{S30}) between 100 and 850 m/s.
- **Data Density:** A minimum of five recordings per event and per station was considered. This improves the statistical reliability of random-effects estimates.

The resulting dataset comprises 1747 3C recordings from 43 events and 310 stations. To characterize the source, path, and site conditions for practical engineering applications, five primary predictor variables were selected: M_w, Z_{tor}, R_{rup}, V_{S30}, and fault mechanism (F_m, categorized as strike-slip, normal, reverse, reverse-oblique, and normal-oblique). Figure 4.1 illustrates the distribution of the selected dataset across these primary predictors.

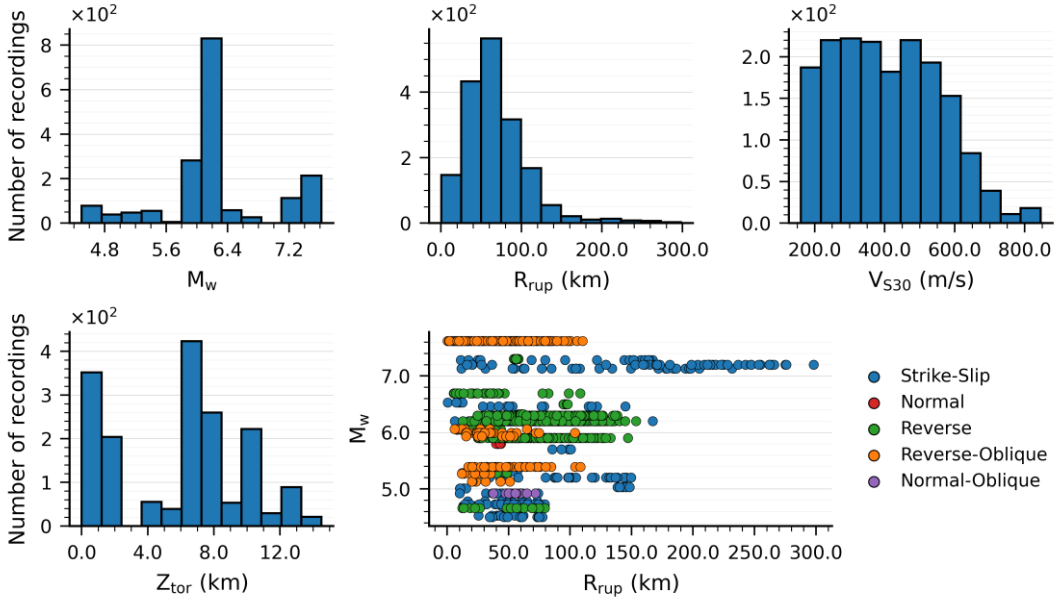


Figure 4.1. Distribution of different seismological parameters of the selected dataset.

The horizontal components of each recording were rotated from their as-recorded orientations into their principal axes of horizontal motion using the rotation angle θ_p in Equation 4.1. This transformation identifies the major (M) and intermediate (I) directions, corresponding to the axes of maximum and minimum horizontal energy, respectively. Here, energy is defined as the time-integral of squared amplitudes. The vertical (V) component was preserved in its original orientation.

The rotation angle θ_p, used in a standard two-dimensional transformation matrix, is calculated such that the resulting pair of horizontal ground motion time-series are statistically uncorrelated. For two orthogonal horizontal components $a_1(t)$ and $a_2(t)$ over a total duration D, this angle is derived using the following closed-form solution:

$$\theta_p = \frac{1}{2}\arctan\left(\frac{2\int_0^D a_1(t)a_2(t)dt}{\int_0^D a_1^2(t)dt - \int_0^D a_2^2(t)dt}\right) \quad 4.1$$

Subsequently, peak ground acceleration (PGA), peak ground velocity (PGV), and 5%-damped spectral acceleration (SA) for periods up to 4.0 s were calculated for each recording across the three principal axes. This data extraction and processing step was executed using the open-source "SGSIM" Python package, which was introduced and verified as part of the methodological developments in Chapter 2 (More information is provided in Chapter 5, Section 5.3.).

4.2.2. Parameterization of the Stochastic Simulation Method

The site-based non-stationary stochastic simulation method developed and validated in Chapter 2 is adopted in this chapter. Ground motion is represented as a non-stationary process derived from band-pass filtered, time-modulated Gaussian white noise. By applying the spectral filter directly to the pre-modulated process, the approach preserves low-frequency content and inherently avoids spectral distortion. This formulation produces an evolutionary Fourier spectrum in which temporal and spectral non-stationarities are explicitly separated.

The modular structure of the simulation framework enables flexible parameterization of both the time-modulating and spectral filter functions. In Chapter 2, a multi-phase modulating function and time-varying filter parameters were employed to achieve high-fidelity simulations of individual accelerograms. However, extending such a high-dimensional parameterization to a large heterogeneous dataset such as the NGA-West2 subset introduces the risk of over-parameterization. This increased statistical complexity can lead to unstable covariance estimates, which are unsuitable for constructing generalized, hazard-consistent ground motion models (GMMs). Therefore, within the integrated predictive framework developed in this chapter, the functional forms are simplified to balance record-level physical fidelity with the statistical stability required for robust predictive modeling. To achieve this balance, physically motivated constraints are imposed during the parameter inversion process, as described in the following subsections.

4.2.2.1. Time-Modulating Function

The temporal energy release is assumed to be dominated by a single strong phase. The time-modulating function $q(t)$ is parameterized using a modified Beta distribution, which is intrinsically bounded by the total duration (D) and total energy (E), building upon the formulation introduced in Chapter 2. To ensure the parameters are more physically intuitive for engineering applications and stable for predictive modeling, the Beta distribution shape parameters, α and β, are reparametrized in terms of the energy centroid ratio (C_r) and its relative spread (S_r) using the statistical method of moments, as follows:

$$v = \frac{C_r(1-C_r)}{S_r^2} - 1, \qquad \alpha = C_r \cdot v, \qquad \beta = (1-C_r)\cdot v \quad 4.2$$

where C_r represents the normalized time of energy arrival ($0 < C_r < 1$), and S_r represents its relative dispersion ($S_r^2 < C_r \cdot (1-C_r)$). The modulating function is then defined as:

$$q(t) = \sqrt{E\frac{t^{\alpha-1}(D-t)^{\beta-1}}{B(\alpha,\beta)D^{\alpha+\beta+1}}} \quad 4.3$$

where $B(\alpha, \beta)$ is the Beta function. While the normalized ratios dictate the mathematical shape of the envelope, the final predictive model is parameterized using the absolute time equivalents: the energy centroid ($C = C_r \cdot D$) and the energy spread ($S = S_r \cdot D$). This choice yields directly interpretable physical quantities. Specifically, the centroid represents the temporal center of the seismic energy release, and the spread corresponds to the effective active duration of the strong motion. For illustrative purposes, Figure 4.2 demonstrates the modulating function and its parameter definitions fitted to a sample ground motion recording from the dataset.

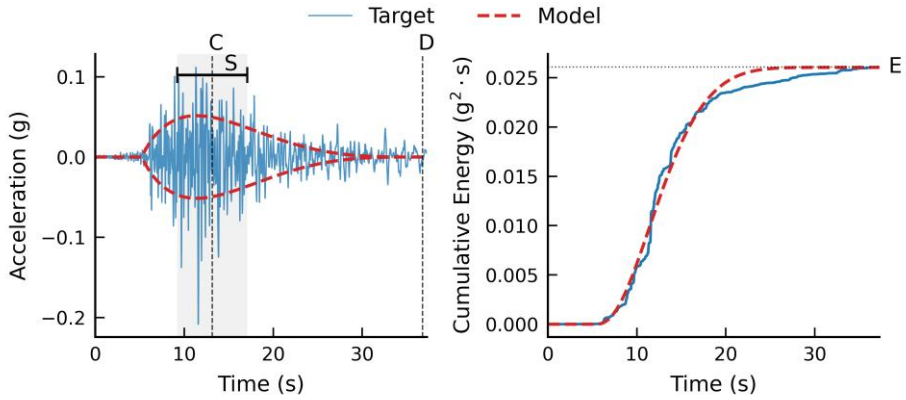


Figure 4.2. Illustrative fit of the Beta modulating function to a sample ground motion record. The extracted parameters are: E_t=0.0261 g^2s, D=36.78 s, C=13.14 s, S=3.93 s.

4.2.2.2. Spectral Filter Function

To ensure a stable and physically interpretable parameterization of the spectral content, two primary constraints are applied to the filter function:

- **Stationary Filter Frequencies:** Tracking frequencies that change rapidly over time can make the model overly sensitive to random noise. To ensure mathematical stability, constant lower (f_L) and upper (f_U) dominant frequencies are assumed. These parameters define the average shape of the frequency spectrum (the "spectral backbone") over the total duration of the record, as established in Chapter 2.
- **Fixed Damping Coefficients:** The damping ratios are constrained to physically informed values to reduce the parameter space and prevent over-fitting. The upper damping ratio is set to $\zeta_U = \frac{1}{\sqrt{2}} = 0.707$, consistent with the maximally flat response of a second-order Butterworth low-pass filter. The lower damping ratio is fixed at $\zeta_L = 1.0$ (critical damping), aligning with established seismic source spectrum models such as Brune's ω^2 model [29,104]. For illustrative purposes, Figure 4.3 compares the Fourier Amplitude Spectrum (FAS) of a sample ground motion recording with the fitted spectral backbone model.

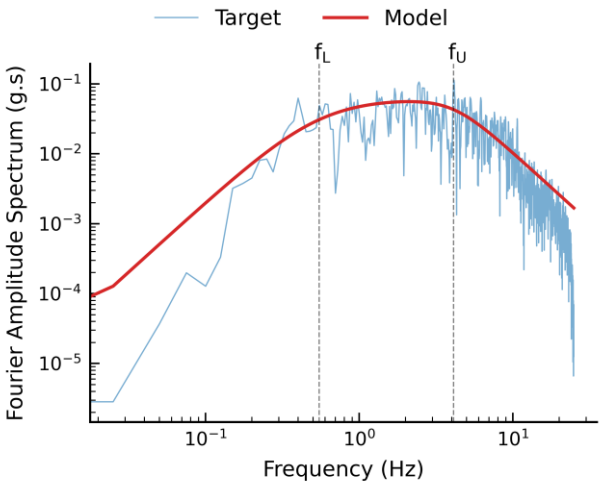


Figure 4.3. Illustrative comparison of the Fourier Amplitude Spectrum (FAS) for a sample recording against the proposed spectral backbone model. The extracted dominant frequencies are: f_L=0.55 Hz and f_U=4.12 Hz.

To calibrate the stochastic model parameters for each rotated record, the "SGSIM" Python package (See Section 5.3) is used. Under the constrained configuration described above, and using the objective functions and optimization procedures defined in Chapter 2, the estimation is reduced to a compact set of six interpretable parameters per principal component (E, D, C, S, f_L, f_U). In the remainder of this chapter, these quantities are collectively referred to as the simulation parameters.

4.2.3. Dataset Preprocessing

The final dataset comprises six simulation parameters (E, D, C, S, f_L, f_U) and 17 IMs (PGA, PGV, and 15 SAs from 0.03s up to 4.0s) per principal component (M, I, V), resulting in 69 response variables per recording. To prevent data leakage during model development, the dataset was partitioned by earthquake events into a training set of 1,533 records and a reserved test set of 214 records for out-of-sample validation. The R_{rup} and V_{S30} predictors and all response variables were transformed into natural logarithmic space to stabilize variance, linearize physical relationships, and ensure strictly positive-definite predictions. The F_m variable was encoded as a set of binary indicator variables representing the different fault mechanisms. Subsequently, the continuous variables were normalized using standard scaling (zero mean and unit variance) to prevent variables with larger numerical ranges from disproportionately influencing the model fitting process and numerical convergence, as described in Section 3.4.1.

4.3. Predictive Modeling Framework

4.3.1. Physics-Informed Neural Additive Model

In the development of empirical GMMs, IMs are conceptually modeled as a multiplicative combination of source, path, and site effects. By applying a natural logarithm transformation to the response variables, this relationship is conventionally formulated as an additive structure:

$$\ln(\mathrm{IM}) = \ln(\mathrm{Source}) + \ln(\mathrm{Path}) + \ln(\mathrm{Site}) \tag{4.4}$$

Conventional GMMs often use rigid, pre-defined functional forms to capture these components, which can introduce bias if the underlying scaling significantly departs from the assumed parametric shape, as discussed in Chapter 3. Conversely, while fully connected ANNs offer considerable flexibility, they typically require large, well-distributed datasets to reliably disentangle multiple physical scaling effects. As illustrated in Chapter 3, even with careful training, limited or uneven data coverage can cause weaker scaling relationships, such as the effect of Z_{tor}, to become partially conflated with stronger predictors,

preventing their independent characterization. To address these limitations while preserving physically interpretable scaling functions, a physics-informed neural additive model (NAM) architecture is adopted here.

4.3.1.1. Model Architecture and Physical Constraints

The NAM architecture mirrors the classic additive GMM form by assigning an isolated one-dimensional (1D) subnetwork to each predictor, effectively preventing unphysical cross-variable interactions. To maintain physical realism, a two-dimensional (2D) subnetwork is dedicated exclusively to the (M_w, R_{rup}) pair. This enables the model to explicitly capture essential magnitude-dependent distance attenuation and joint scaling interactions without compromising the overall interpretability of the framework. As illustrated in Figure 4.4, the global prediction y is formulated as the sum of six independent subnetworks and a global bias, β_0, expressed as:

$$y = \beta_0 + \sum_{i=1}^{6} f_i(x_i) \qquad 4.5$$

To enforce physical constraints while preventing overfitting, the additive subnetworks $f_i(x_i)$ employ distinct architectural designs based on the physical nature of their input features:

- **Wide Path:** A direct linear bypass with no bias and no activation function for only nonmonotonic features. This path allows for unbounded physical scaling.
- **Deep Path:** A multi-layer perceptron (MLP) consisting of a single hidden layer with a hyperbolic tangent (Tanh) activation function to capture smooth, saturating non-linearities.

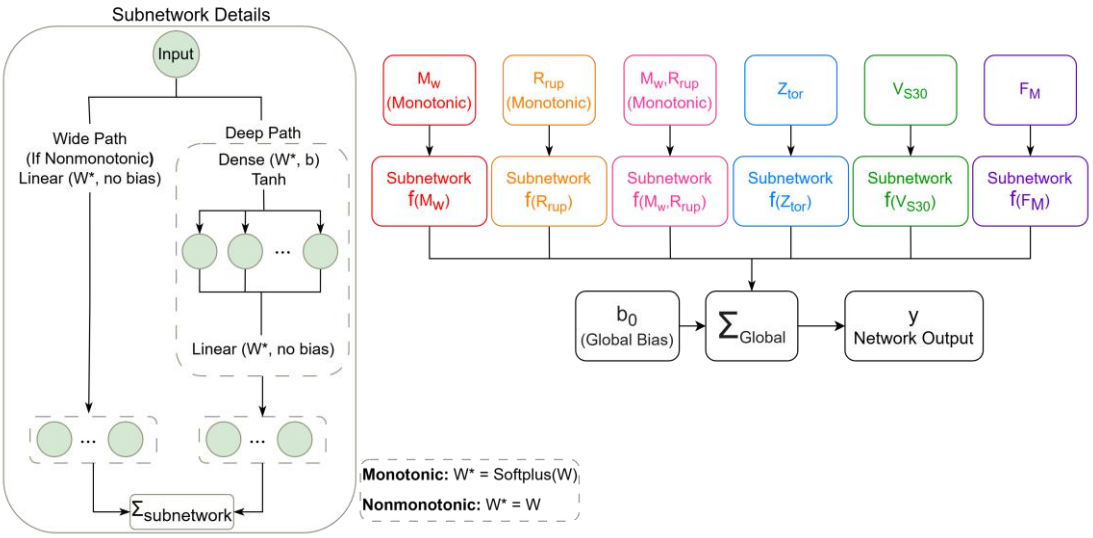


Figure 4.4. Schematic architecture of the physics-informed neural additive model. The left panel details the internal wide path and deep path design of a single subnetwork.

While purely data-driven machine learning (ML) models generally capture macroscopic scaling trends in data-rich regions, they can violate established physical scaling laws when trained on sparse seismic datasets or extrapolated to extreme hazard scenarios. To explicitly embed physical domain knowledge and prevent such non-physical behavior, hard architectural constraints are enforced for monotonic predictors (i.e., M_w, R_{rup}) rather than relying on soft penalty terms in a loss function. To guarantee strict physical monotonicity, the internal weights are constrained to be strictly positive via a softplus transformation, defined as:

$$f(x) = \ln(1 + e^x) \qquad 4.6$$

For a subnetwork with input x, the positive slope is preserved such that $\frac{\partial \mathrm{f}}{\partial \mathrm{x}} \geq 0$. Decreasing physical trends, such as attenuation with distance, are enforced by applying a negative sign-flip to the input before it enters the monotonic subnetwork. Conversely, nonmonotonic features (e.g., V_{S30}) use unconstrained weights to allow for more flexible shapes.

4.3.1.2. Implementation and Hyperparameter Tuning

Within this integrated framework, the neural network architectures were implemented in Python using the PyTorch library. Because the response variables exhibit distinct scaling behaviors, they were grouped into four categories with group-specific physical constraints applied as detailed in Table 4.1.

To establish the hyperparameter configuration, a broad sequential search was initially performed using the Optuna optimization framework [102] coupled with 5-fold Group K-Fold cross-validation. Adopting the validation procedure established in Section 3.4.2, the data was strictly partitioned by earthquake events to prevent data leakage and ensure robust generalization to unseen seismic scenarios. Optimization was performed using the L-BFGS algorithm with a Strong-Wolfe line search, which provides efficient deterministic convergence for empirical modeling.

Initial exploratory tuning revealed that due to the strict physical constraints enforced by the monotonic architecture, large network capacities led to parameter unidentifiability without yielding meaningful improvements in empirical accuracy. Therefore, to prioritize model parsimony, the subnetworks were explicitly restricted to a minimal capacity of exactly 3 hidden units per feature. Additionally, convergence analyses demonstrated that the L-BFGS optimizer was highly efficient, consistently reaching the loss plateau within the first few iterations. To prevent overfitting to noise and avoid redundant computation, training was governed by an early stopping rule that terminated execution once the absolute change in loss between consecutive epochs fell below10^{-4}. Consequently, while the maximum ceiling was set to 100 epochs as a nominal safety margin, the algorithm consistently achieved stable convergence and triggered an early stop well under 10 epochs.

Therefore, the core optimization strategy focused exclusively on tuning the L2 regularization penalty (weight decay). Optimization used a fixed learning rate of 1.0, a Hessian history size of 20, and a maximum of 20 iterations for the internal L-BFGS line search. Crucially, the tuned L2 penalty was selectively applied only to the weights of the Deep Path to penalize unnecessary non-linear complexity. All global biases and Wide Path weights were explicitly left unregularized, guaranteeing that the baseline macro-physical scaling and linear trends were perfectly preserved without penalty. Table 4.1 summarizes the final tuned configurations.

Table 4.1. Summary of physical constraints and hyperparameters for grouped variables.

Response Variables	M_w Constraint	R_{rup} Constraint	L2 (Weight Decay)
E, PGA, PGV, SA	Increasing (+)	Decreasing (–)	5.0×10^{-3}
D, C, S	Increasing (+)	Increasing (+)	4.2×10^{-3}
fL	Decreasing (–)	Decreasing (–)	6.3×10^{-3}
fU	Decreasing (–)	Decreasing (–)	4.6×10^{-3}

4.3.2. Multivariate Mixed-Effects Regression

The NAM acts as the fixed-effects component to capture the median physical scaling. However, as established in Chapter 3, ground motion recordings inherently violate the standard regression assumption of independent observations. Multiple recordings from the same earthquake share macro-source characteristics, while multiple recordings at the same station reflect identical localized site conditions. To explicitly model these multi-level correlated dependencies and rigorously partition the total aleatory variability, the NAM architecture is directly integrated into the multivariate mixed-effects regression (MMER) framework developed in Chapter 3.

To provide a physically intuitive representation of how individual components interact, the predicted vector of response variables Y_{ijk} for a given ground motion record i, generated by earthquake event j, and recorded at station k, can be expanded at the individual record level. Inheriting the formal multivariate matrix structure established in Chapter 3, this multi-level statistical mapping is explicitly decomposed as follows:

$$\ln(Y_{ijk}) = f_{NAM}(X_{ijk}) + \eta_j + \delta_k + \epsilon_{ijk} \quad 4.7$$

where:

- $f_{NAM}(X_{ijk})$ is the median response vector predicted by the physics-informed NAM (fixed-effects).
- η_j denotes the multivariate between-event residual for earthquake j, assumed to follow $N(0, \Sigma_{event})$. It captures the average systematic deviation due to unmodeled source characteristics (e.g., stress drop).
- δ_k is the multivariate between-site residual for station k, assumed to follow $N(0, \Sigma_{site})$. It captures systematic deviations caused by localized, unmodeled site effects.
- ϵ_{ijk} is the remaining within-event residual, assumed to follow $N(0, \Sigma_{residual})$. It describes record-to-record variability.

The joint estimation of the fixed-effects and multi-level covariance components was executed via maximum likelihood estimation using the "MMER" Python package developed in Chapter 3. Repository availability and open-access details are summarized in Section 5.3.

4.4. Model Validation and Physical Scaling

4.4.1. Predictive Performance

The predictive performance of the NAM was evaluated using the coefficient of determination (R^2), Pearson correlation coefficient (r), mean absolute error (MAE), and root mean squared error (RMSE), all computed in natural logarithmic (ln) units. Table 4.2 summarizes the average performance across all response variables for both the training and unseen test sets in natural logarithmic space. Although the test performance is marginally higher than that of the training set, this behavior is expected given the event-based data partitioning strategy and the model's reduced tendency to fit training noise due to the imposed physical constraints. Results reveal that the NAM achieves an average R^2 of 0.695 on the unseen test set. This degree of explanatory power indicates strong generalization capability, despite the sparse nature of the seismic dataset. Furthermore, the consistency between training and test metrics confirms that the physics-informed architecture effectively isolated scaling trends without overfitting to the training set.

Table 4.2. Average model performance metrics across all response variables (ln units).

Metric	Training	Test
R2	0.635	0.695
r	0.794	0.861
MAE	0.505	0.613
RMSE	0.660	0.753

To ensure clarity and avoid visual clutter, the subsequent analyses focus exclusively on the major component, as the intermediate and vertical components exhibit highly similar scaling trends. The detailed performance metrics for all response variables across the three principal axes are provided in Table A3 of the Appendix. As illustrated in Figure 4.5 and Figure 4.6, the model's performance varies according to the physical nature of the response variables. Amplitude-based parameters, such as E and IMs, exhibit the highest explanatory power ($R^2 > 0.70$) and relatively low prediction errors. These parameters are well-described by the selected predictor variables. In contrast, temporal parameters

(D, C, S) show higher dispersion and lower R^2 values. This reflects the inherent stochasticity of earthquake rupture kinematics. The temporal duration of ground motion is highly sensitive to complex wave scattering and multipath propagation, resulting in a naturally higher aleatory noise floor. Frequency parameters (f_L, f_U) exhibit intermediate performance. The reduced explanatory power for temporal and frequency parameters suggests that they are less strictly described by the simplified predictors used in this chapter, and are more sensitive to unmodeled source, path, and site heterogeneities.

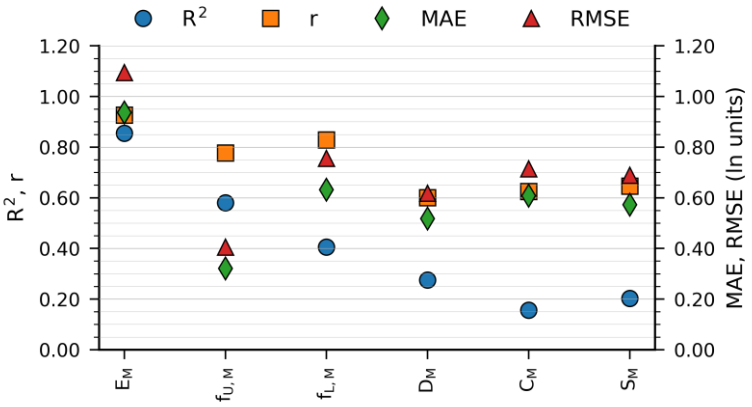


Figure 4.5. Predictive performance metrics for simulation parameters (major component).

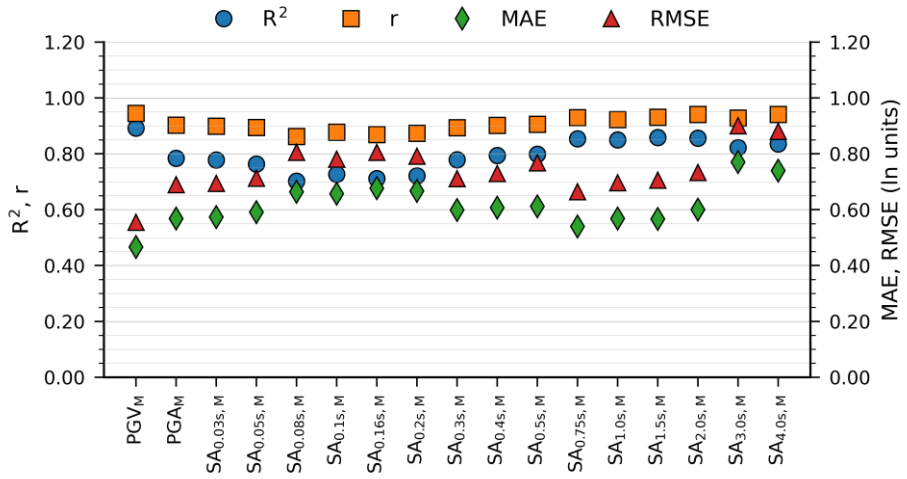


Figure 4.6. Predictive performance metrics for intensity measures (major component).

4.4.2. Median Physical Scaling

To verify that the NAM has learned physical relationships, the median predictions across representative earthquake scenarios were examined. Figure 4.7 to Figure 4.12 illustrate the scaling of a representative set of simulation parameters and IMs of the major horizontal component (S_M, E_M, $f_{L,M}$, $f_{U,M}$, PGA_M, $SA_{4.0s,M}$) with respect to M_w and R_{rup}.

Consistent with established seismological principles [29,105], S_M (Figure 4.7) exhibits a predominantly log-linear increase with M_w, reflecting the longer source rupture durations of larger events. It increases monotonically with R_{rup} due to wave propagation path scattering and then stabilizes into an asymptotic trend at large distances. Notably, the model smoothly captures the scaling interaction between M_w and R_{rup}, while the enforced monotonicity constraints strictly prevent non-physical oscillations and preserve stable extrapolation bounds outside the data range.

As shown in Figure 4.8, E_M exhibits a distinct curvature with M_w, where the magnitude scaling rate visibly flattens at larger M_w. This smooth saturation behavior is consistent with established empirical

cumulative energy models (e.g., [106]). Additionally, the model accurately tracks the expected geometric attenuation of energy with R_{rup}. The embedded physical constraints ensure stable behavior for $M_w > 7.0$, capturing a clear yet natural saturation trend supported by the data.

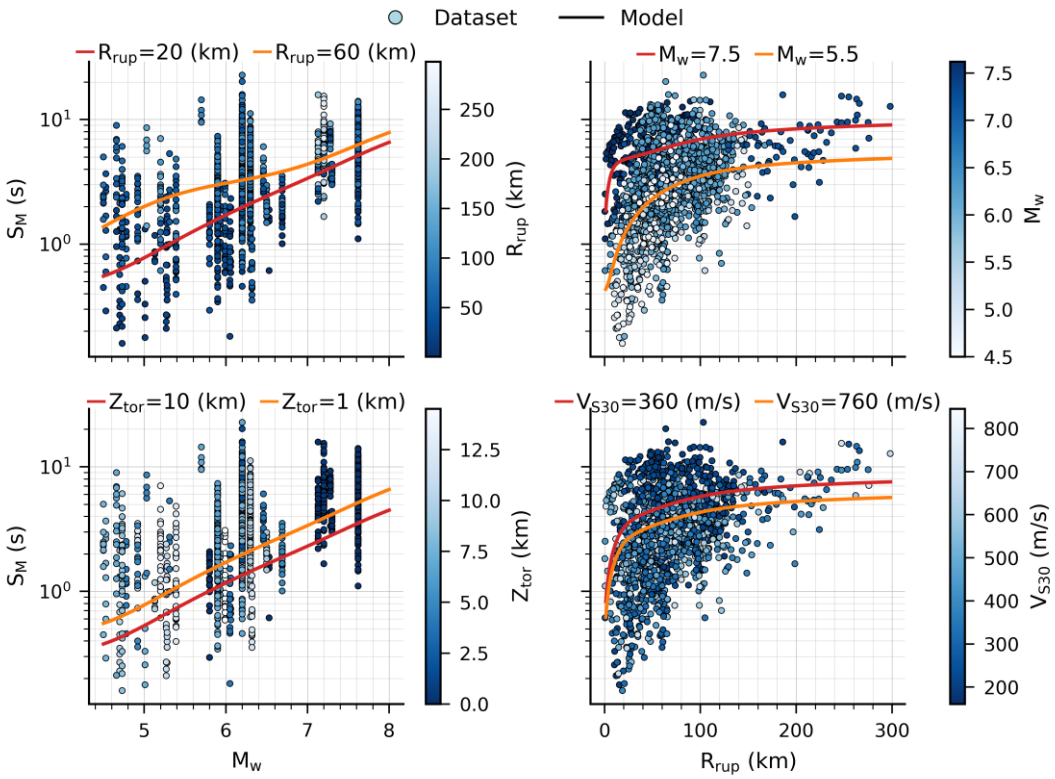


Figure 4.7. Median scaling relationship for spread parameter of the major component (S_M). Default values for unspecified parameters are Z_{tor} = 1 km, V_{S30} = 760 m/s, R_{rup} = 20 km, M_w = 6.5, and a strike-slip fault mechanism.

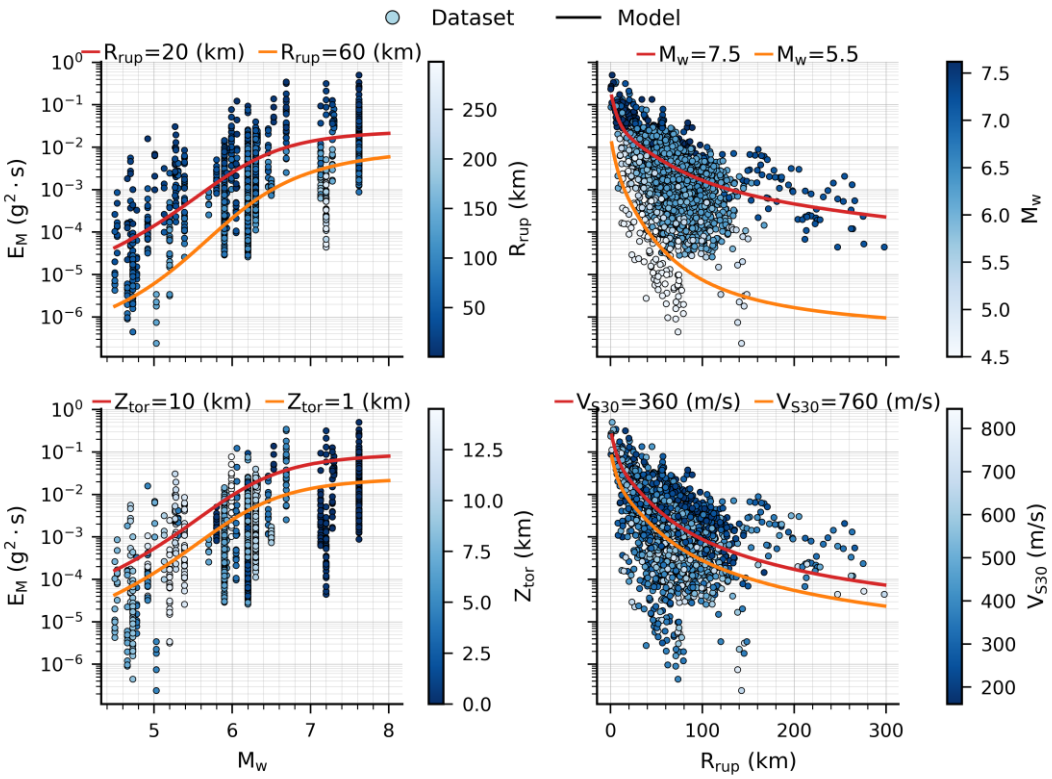


Figure 4.8. Median scaling relationship for total energy of the major component (E_M). Default values for unspecified parameters are Z_{tor} = 1 km, V_{S30} = 760 m/s, R_{rup} = 20 km, M_w = 6.5, and a strike-slip fault mechanism.

The NAM also captures established physical relationships governing the frequency content of the ground motions. As shown in Figure 4.9, the lower dominant frequency ($f_{L,M}$) exhibits a clear inverse relationship with M_w. This fundamentally aligns with Brune's source model [29,104], which dictates that larger magnitude events, having larger rupture surfaces, naturally produce lower corner frequencies. Beyond this primary source-size effect, the model resolves a very slight downward scaling with R_{rup} for larger M_w events, which conceptually reflects the gradual scattering and elongation of the wave records over longer distances. Conversely, for smaller events, the trend remains relatively flat, consistent with the limited long-period energy generated by smaller, shorter-duration source ruptures. The slight curvature observed at the M_w extremes may reflect the operational limits of the dataset. Because f_L is extracted from records, its resolution at extreme M_w values can be inherently constrained by a combination of instrument sensitivity, record lengths, and signal-processing filters.

The upper dominant frequency ($f_{U,M}$), shown in Figure 4.10, characterizes the high-frequency decay of the spectrum. Unlike the source-driven lower frequency parameter, which shows no discernible sensitivity to site conditions (V_{S30}), f_U exhibits a clear dependence on V_{S30}, reflecting near-surface filtering. The model captures a clear downward scaling of f_U with R_{rup}, reflecting the physical effects of geometric spreading and anelastic attenuation as high-frequency energy dissipates over longer propagation distances.

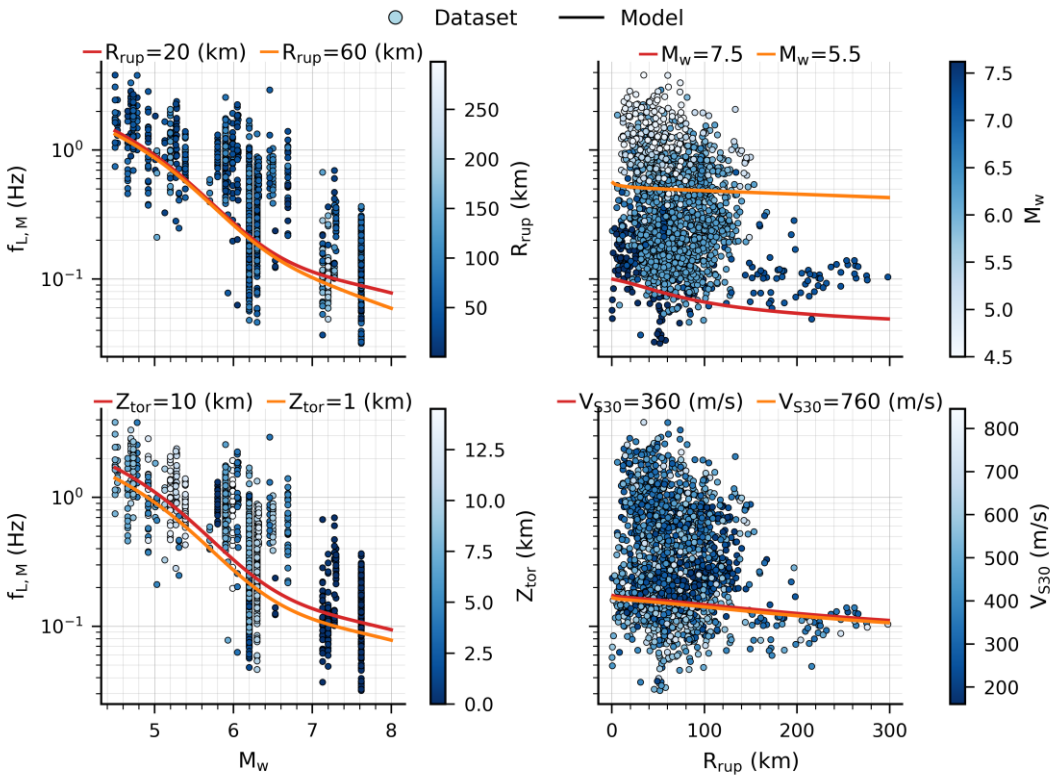


Figure 4.9. Median scaling relationship for the lower dominant frequency of the major component ($f_{L,M}$). Default values for unspecified parameters are Z_{tor}=1 km, V_{S30}=760 m/s, R_{rup}=20 km, M_w=6.5, and a strike-slip fault mechanism.

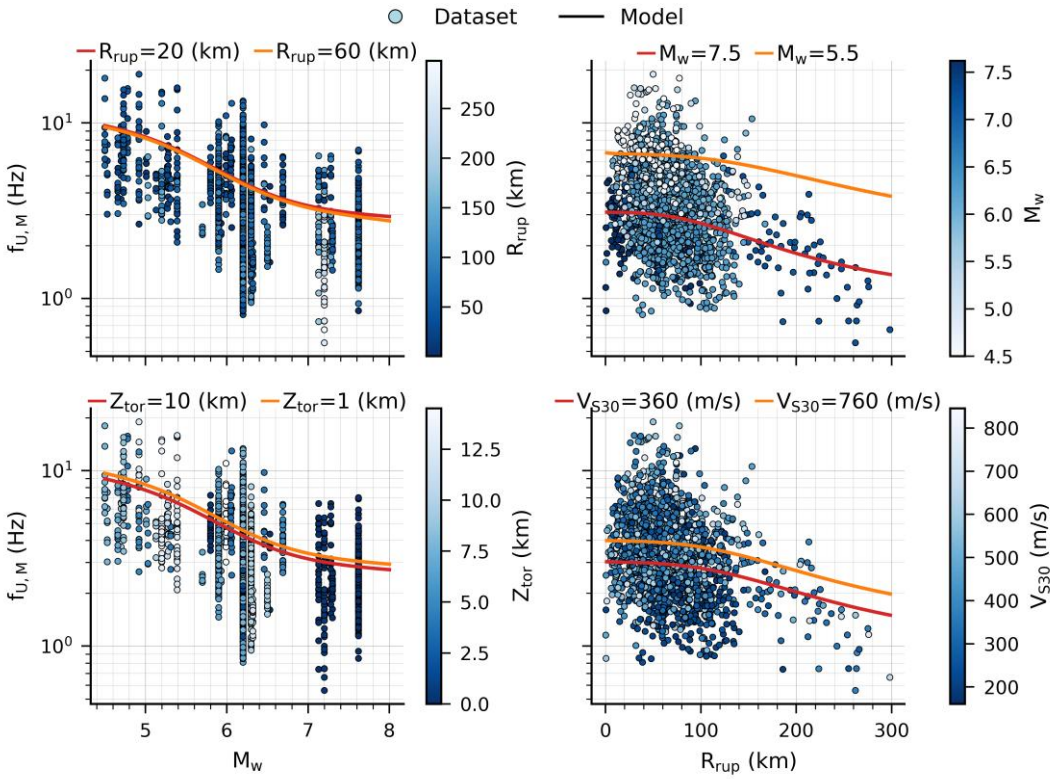


Figure 4.10. Median scaling relationship for upper dominant frequency of the major component ($f_{U,M}$). Default values for unspecified parameters are Z_{tor}=1 km, V_{S30}=760 m/s, R_{rup}=20 km, M_w=6.5, and a strike-slip fault mechanism.

Finally, the median scaling of PGA_M and $SA_{4.0s,\ M}$ confirms that the NAM captures distinct frequency-dependent behavior across IMs, as shown in Figure 4.11 and Figure 4.12, respectively. Both IMs exhibit smooth magnitude saturation at large M_w values, while distance attenuation remains robust and monotonic across the entire R_{rup} range. A key distinction lies in the frequency-dependent sensitivity to Z_{tor}. As shown in the bottom-left panels of Figure 4.11 and Figure 4.12, the high-frequency PGA_M is amplified for deeper, buried ruptures, consistent with established seismological observations that such ruptures typically exhibit higher stress drops and radiate stronger high-frequency energy [107]. In contrast, the long-period $SA_{4.0s,\ M}$ shows negligible sensitivity to Z_{tor}. Notably, this distinct frequency-dependent sensitivity to Z_{tor} is resolved with much greater clarity here than in the initial illustrative models of Chapter 3. While the standard unconstrained MLP formulation in Section 3.5.2 struggled to fully isolate these secondary physical paths due to over-parameterization and minor data sparsity, the physics-informed architecture of the NAM successfully uncouples these interactions. By explicitly constraining the primary scaling behaviors (M_w, R_{rup}), the modeling framework is stabilized enough to resolve subtle, localized physical trends like Z_{tor} scaling without learning non-physical data artifacts. Additionally, both models accurately reproduce the expected linear site amplification associated with V_{S30}.

Lastly, the model's ability to automatically learn and distinguish these subtle source-, path-, and site-dependent effects highlights its robustness for seismic hazard applications. Collectively, these evaluations confirm that the NAM effectively balances the flexibility of ML with the stability of empirical scaling laws.

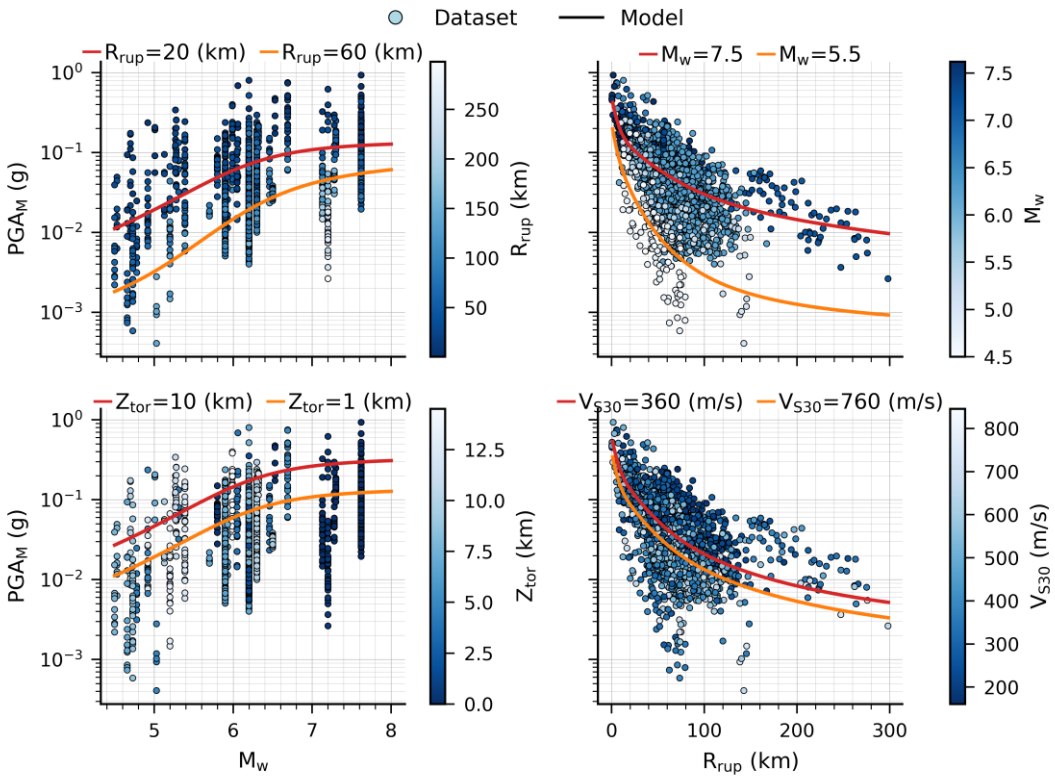


Figure 4.11. Median scaling relationship for peak ground acceleration of the major component (PGA_M). Default values for unspecified parameters are Z_{tor}=1 km, V_{S30}=760 m/s, R_{rup}=20 km, M_w=6.5, and a strike-slip fault mechanism.

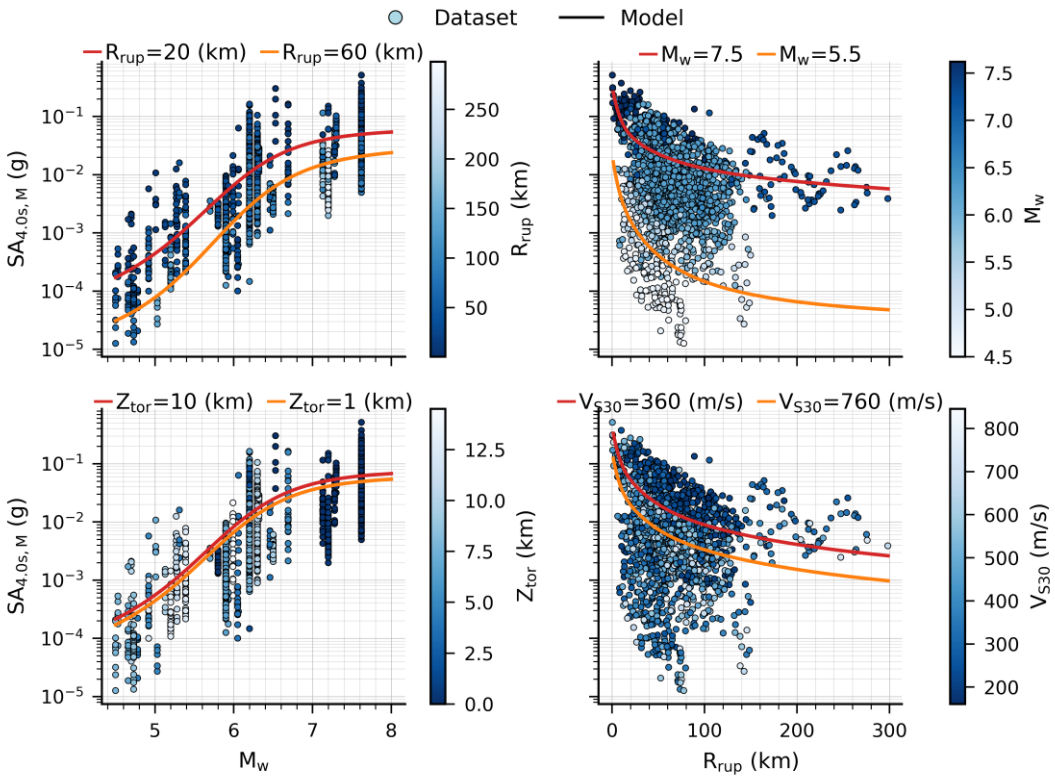


Figure 4.12. Median scaling relationship for spectral acceleration at a period of 4.0s of the major component ($SA_{4.0s,M}$). Default values for unspecified parameters are Z_{tor}=1 km, V_{S30}=760 m/s, R_{rup}=20 km, M_w=6.5, and a strike-slip fault mechanism.

4.4.3. Variance Partitioning and Residual Analysis

The integration of the NAM into the MMER framework allows for the explicit decomposition of total aleatory variability into three statistically independent components: between-event, between-site, and the remaining within-event residual. The standard deviations of all response variables across these aleatory components are derived from the diagonal elements of the estimated covariance matrices and provided in the Appendix Table A3.

The partitioning of variance for the simulation parameters and IMs of the major component is illustrated in Figure 4.13 and Figure 4.14, respectively. Across both figures, the between-event component emerges as the primary source of uncertainty. This reflects substantial source-to-source variations, such as varying stress drop and rupture complexity, which are not fully captured by primary macroscopic source predictors like M_w alone.

In Figure 4.13, $f_{L,M}$ exhibits minimal between-site variance, reinforcing that it is primarily a source-driven parameter governed by rupture size rather than path or site conditions. In contrast, $f_{U,M}$ shows a noticeably higher contribution from the between-site component, reflecting its physical sensitivity to localized, site-specific attenuation.

For the IMs (Figure 4.14), the between-event component is characterized by a localized increase around the 0.08 s period and a steady rise toward longer periods, consistent with previous observations [51,100]. The within-event residual acts as the second substantial contributor across all IMs, representing standard record-to-record path scattering and waveform variability. While the between-site component is a smaller contributor to the total variance, it remains relatively stable across the spectrum, decreasing only slightly at long period SAs.

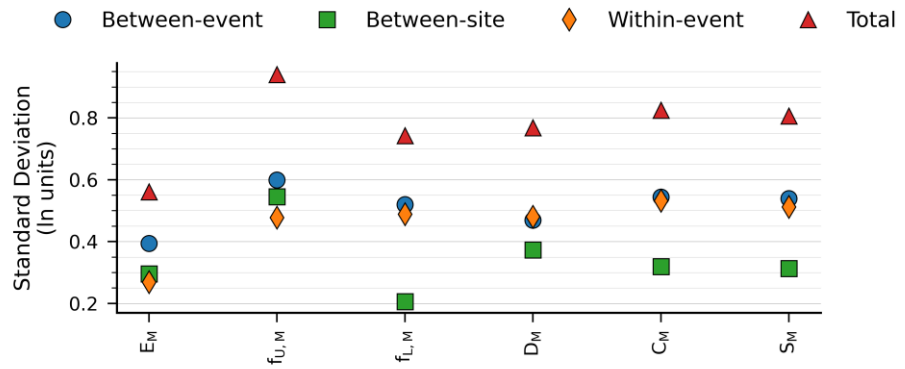


Figure 4.13. Standard deviations of the aleatory components across major-component simulation parameters.

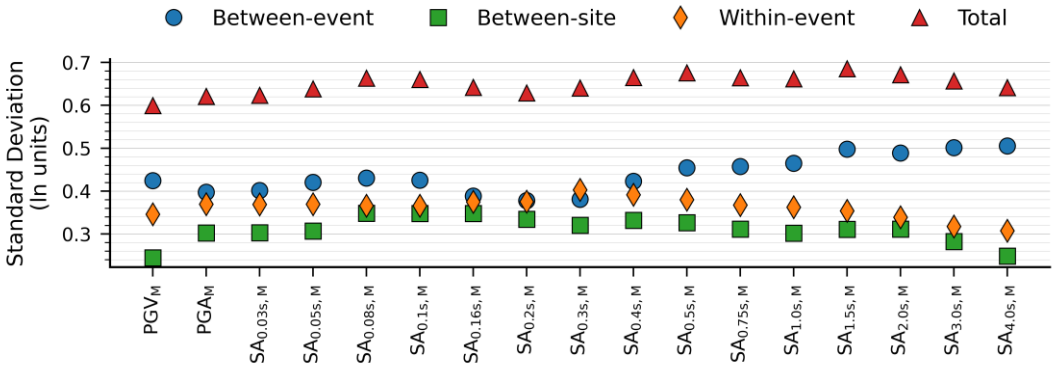


Figure 4.14. Standard deviations of the aleatory components across major-component intensity measures.

To assess the model for systematic bias, residuals were analyzed against the primary seismological predictors, focusing on the representative set of response variables of the major component. Binned means and corresponding standard deviations were overlaid on the scatter data, alongside p-values derived from linear regression. As shown in Figure 4.15, the within-event residuals against R_{rup} exhibit random dispersion. The binned means remain close to zero, and the p-values consistently exceed 0.05, indicating no detectable linear trend with distance. Similarly, the between-site residuals show no discernible trend with V_{S30}, as shown in Figure 4.16. Overall, the absence of systematic structure in these residuals suggests that the NAM adequately represents the average distance attenuation and site response.

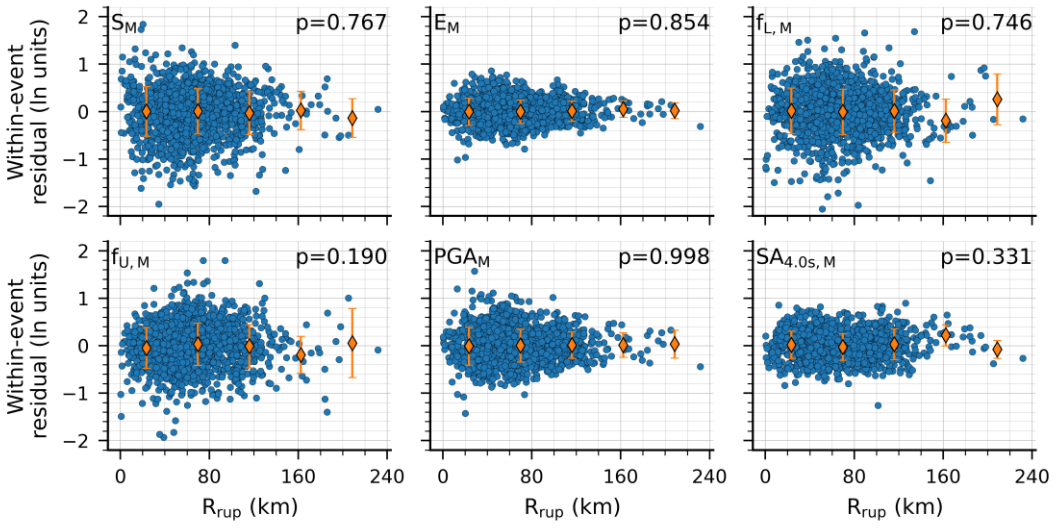


Figure 4.15. Variation of unexplained within-event residuals with R_{rup}.

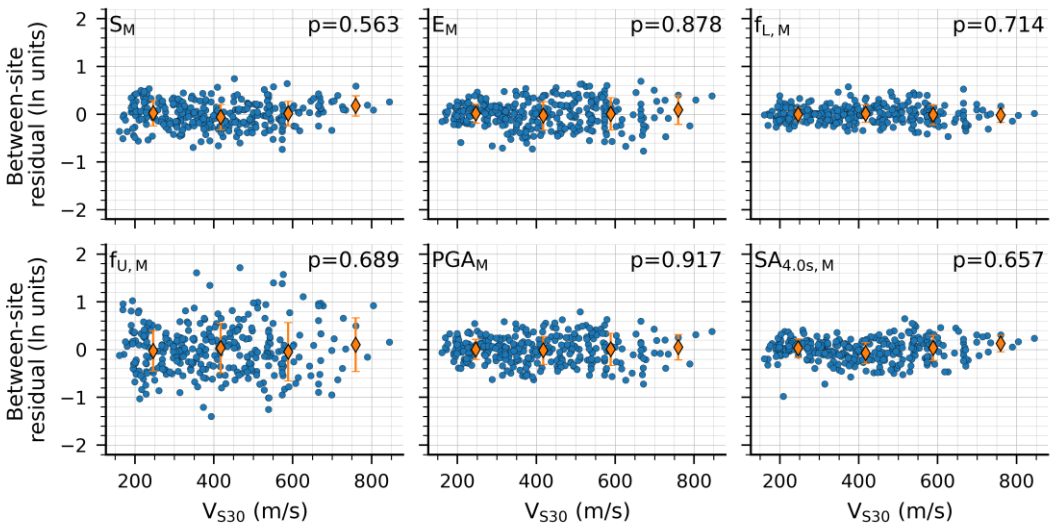


Figure 4.16. Variation of between-site residuals with V_{S30}.

Between-event residuals were evaluated against M_w and Z_{tor} in Figure 4.17 and Figure 4.18. While the binned means exhibit minor fluctuations around zero across the magnitude range, the p-values remain strictly above 0.05, confirming no statistically significant linear bias. The localized deviations observed in certain bins are directly attributable to the uneven data density resulting from the applied magnitude-distance filtering, making those specific intervals more sensitive to sampling variability. Overall, the residuals do not exhibit systematic structure with respect to M_w or Z_{tor}.

Finally, the absence of systematic structure in the residuals across source, path, and site predictors supports the adequacy of the NAM architecture and the numerical stability of the regression framework.

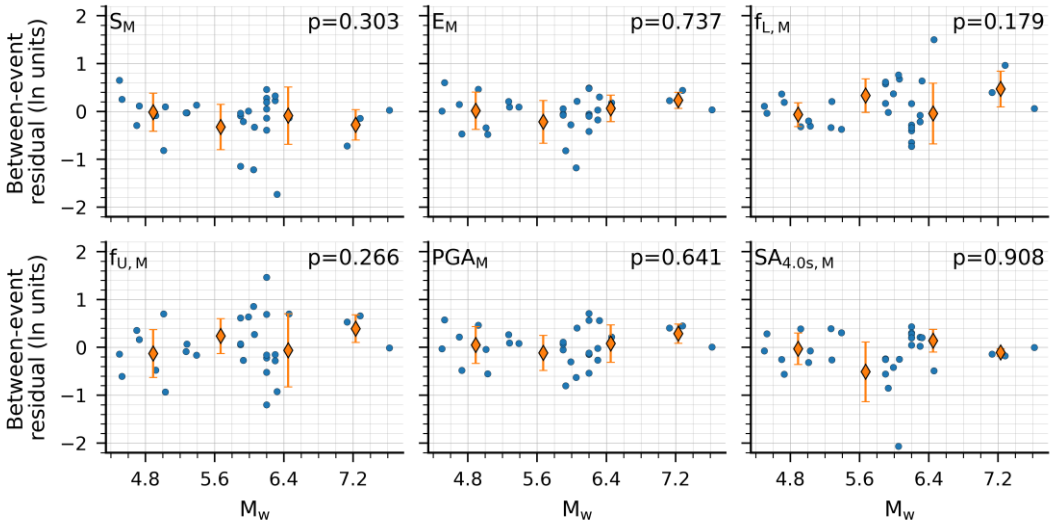


Figure 4.17. Variation of between-event residuals with M_w.

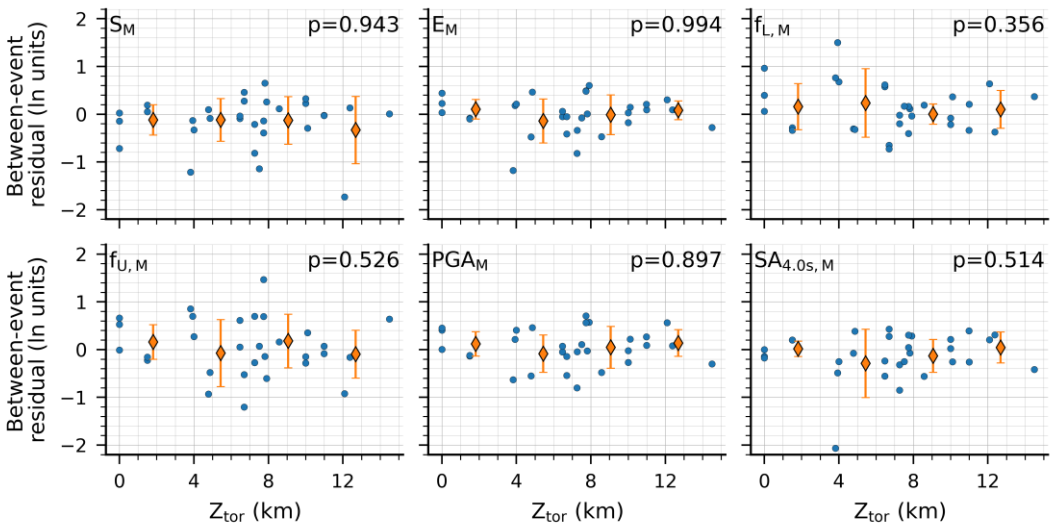


Figure 4.18. Variation of between-event residuals with Z_{tor}.

4.4.4. Inter-Parameter and Spectral Correlations

This section evaluates the total correlation structure, which integrates the combined effects of the between-event, between-site, and within-event aleatory components. The complete total correlation matrix, encompassing all response variables across the three principal axes, is embedded directly within the deployed generative model and is openly accessible via the accompanying Python package repository (as detailed in Section 5.3).

Figure 4.19 presents the total correlation matrix for the simulation parameters across the principal axes. The matrix exhibits a clear block-structured pattern, indicating strong intra-component and inter-component dependencies. As expected, the correlation between the parameters of two horizontal components (M-I) is consistently stronger than the correlation between either horizontal component and the vertical axis (M-V or I-V). This difference arises because horizontal ground motions are primarily dominated by shear-wave (S-wave) energy [108], whereas vertical motions are more strongly influenced by P-waves and exhibit distinct propagation and site-response characteristics [109].

To further investigate the underlying physical interactions, Figure 4.20 illustrates the cross-correlations between the simulation parameters and the IMs of the major component. As expected, PGA exhibits a strong positive correlation with short-period spectral accelerations, with this dependence gradually weakening toward longer periods, whereas PGV remains strongly correlated with intermediate- and long-period spectral ordinates, reflecting their respective sensitivity to high- and mid-frequency ground motion content.

The temporal parameters (D, C, and S) show a pronounced frequency-dependent behavior, characterized by negative correlations with short-period spectral accelerations that progressively transition to positive values at longer periods. This trend is physically meaningful, as longer-duration motions are typically associated with large-magnitude events and basin-induced surface waves, which contain substantial long-period energy, while short-duration impulsive ruptures tend to generate concentrated high-frequency acceleration peaks [110,111].

A similarly consistent pattern is observed for the frequency parameters (f_L and f_U), which correlate positively with short-period IMs and negatively with long-period IMs, confirming that higher dominant frequencies preferentially concentrate seismic energy in the short-period range while reducing relative long-period amplitudes. Across all IMs, the total energy parameter (E) maintains strong positive correlations, highlighting its fundamental role as the principal scaling parameter controlling the overall intensity of ground motions.

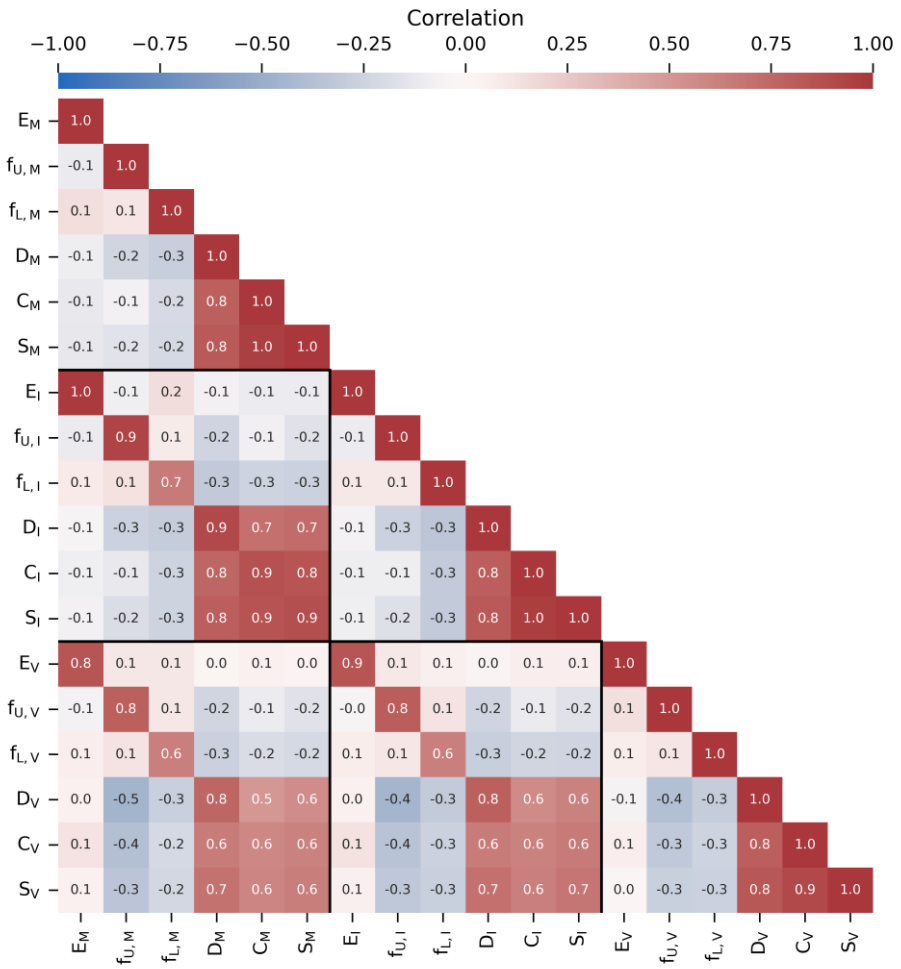


Figure 4.19. Total correlation matrix of the simulation parameters for the major (M), intermediate (I), and vertical (V) components.

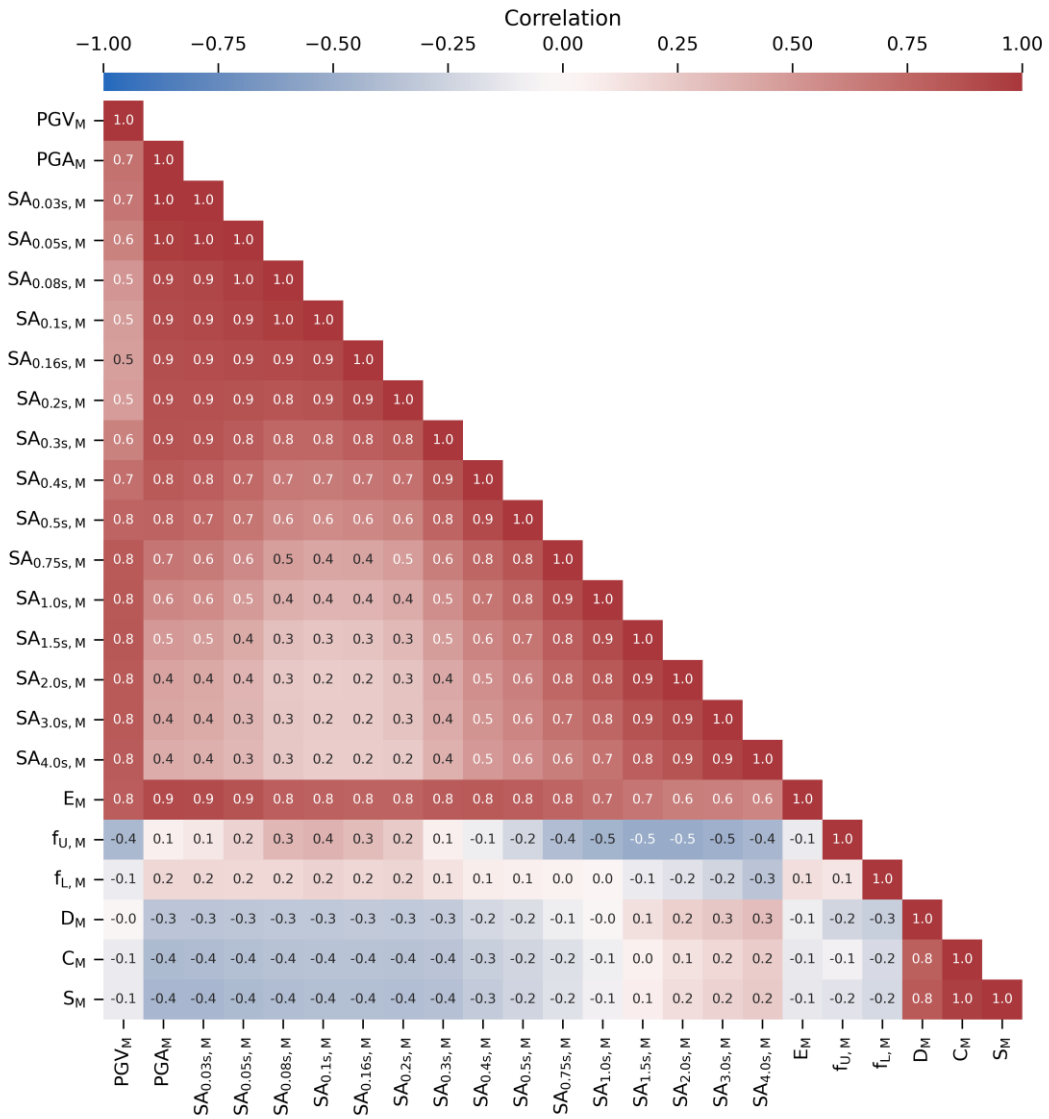


Figure 4.20. Total correlation matrix of the simulation parameters and intensity measures for the major (M) component.

Lastly, the inter-period correlation structure provides an additional validation of the framework's spectral consistency. Figure 4.21 compares the total correlation for three representative spectral periods (0.1 s, 1.0 s, and 4.0 s) against the empirical models of Baker and Jayaram (2008) and Baker and Bradley (2017) [59,60]. Across all periods, the major, intermediate, and vertical components exhibit remarkable consistency, closely tracking the empirical benchmarks throughout the entire period range. Notably, for the long-period $SA_{4.0s}$, the simulated components demonstrate a closer affinity to the Baker and Bradley (2017) model, capturing the updated long-period correlation features. Because the framework directly estimates the full covariance structure, these physically meaningful inter-period dependencies are captured inherently within the framework, without requiring additional correlation adjustment or post-processing.

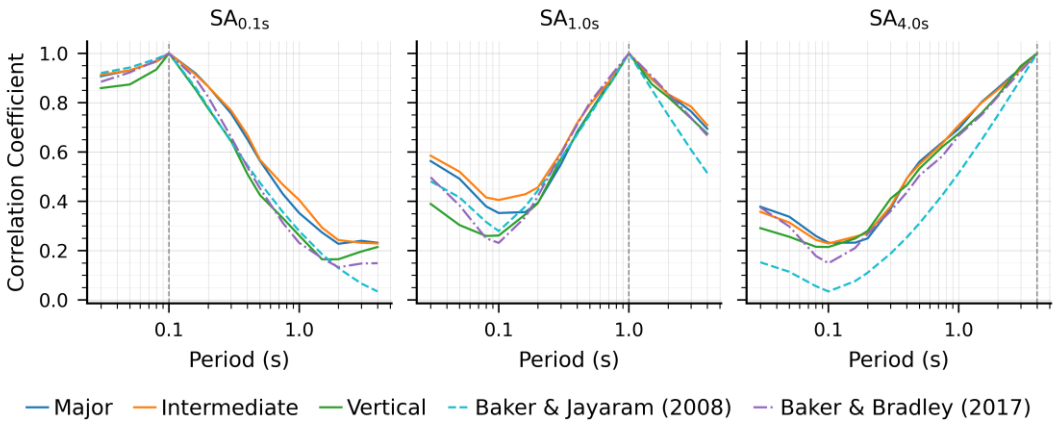


Figure 4.21. Total correlation coefficients of spectral acceleration (SA) at representative periods (0.1, 1.0, and 4.0 s) across spectral periods for the principal axes.

4.5. Hazard-Compatible Ground Motion Simulation

4.5.1. Unconditional Simulation

Given an earthquake design scenario defined by basic seismological parameters (M_w, R_{rup}, V_{S30}, Z_{tor}, F_m), the proposed framework predicts the median response vector, encompassing both the stochastic simulation parameters and standard IMs across the three principal axes. To capture the natural aleatory variability of ground motions, a synthetic response vector Y_{sim} can be sampled from a multivariate normal distribution:

$$Y_{sim} \sim N(\mu_{NAM}, \Sigma_{total}) \quad 4.8$$

where μ_{NAM} is the median predictive vector from the NAM, and Σ_{total} is the total covariance matrix (the sum of the between-event, between-site, and within-event covariance matrices). Once sampled, the component-specific simulation parameters within Y_{sim} are directly passed to the stochastic simulation method using the SGSIM Python package to synthesize the corresponding three-component ground motion time-series.

Sampling directly from the covariance matrix is a critical advantage of this framework. It mathematically enforces that physical differences and statistical correlations among the major, intermediate, and vertical components are strictly preserved (e.g., $E_M > E_I$).

Because the simulation relies on an underlying stochastic white noise sequence, the goal is not to deterministically match any particular recorded waveform, as such a comparison would inherently be subjective. Instead, the objective is to generate an ensemble of statistically consistent and physically realistic ground motions. As a visual validation, Figure 4.22 demonstrates the simulated acceleration, velocity, and displacement time-series for a specified sample earthquake scenario (M_w = 6.5, Z_{tor} = 1.0 km, R_{rup} = 25.0 km, V_{S30} = 560.0 m/s, F_m = Strike-Slip). One distinct realization is highlighted in black and overlaid on five faded realizations to illustrate the natural waveform diversity. These simulations exhibit realistic waveform characteristics while maintaining physically appropriate amplitude scaling across the major, intermediate, and vertical components.

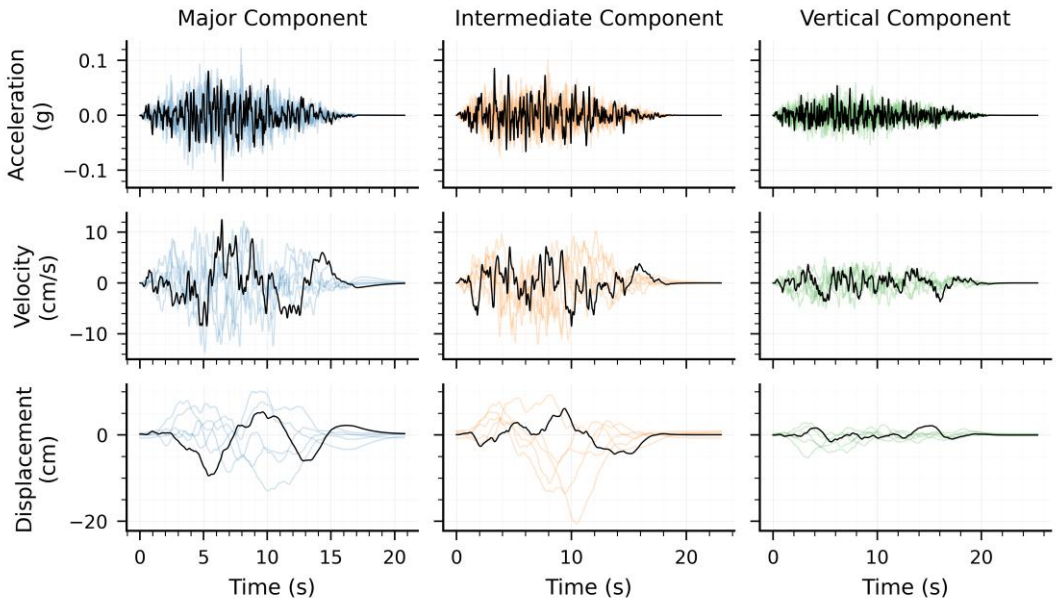


Figure 4.22. Qualitative visualization of simulated major, intermediate, and vertical component time-series (acceleration, velocity, and displacement) for M_w=6.5, Z_{tor}=1.0 km, R_{rup}=25.0 km, V_{S30}=560.0 m/s, F_m=Strike-Slip. One realization is highlighted in black and overlaid on five faded realizations to illustrate waveform diversity.

4.5.2. Spectral Consistency Verification

For further validation, the empirical SAs predicted by the NAM (SA_{NAM}) were compared with those derived from the corresponding stochastic simulations (SA_{Sim}). The stochastic simulation reproduces the average behavior of its target ground motion through random realizations of white noise excitation. Individual realizations therefore exhibit local fluctuations and spectral variability that are not expected to exactly match the recorded waveform. Accordingly, validation is not based on pointwise agreement, but on the consistency between the SA_{NAM} and the ensemble-average behavior of SA_{Sim}.

For this purpose, the median simulation parameters predicted by the NAM ($\mu_{\mathbf{NAM}}$) for the previous sample scenario were used to generate 100 independent stochastic ground motion realizations. This isolates the white noise stochasticity from the parameter sampling variance. Then, the median SA from these 100 simulated waveforms was calculated and compared directly against the discrete SA_{NAM}.

As illustrated in Figure 4.23, the median SA_{Sim} aligns closely with the direct SA_{NAM} predictions across the entire period range for both horizontal components. For the vertical component, a minor spectral shift is observed near the peak response period (0.1 s to 0.3 s). This localized discrepancy stems from the fundamental difference between the two modeling approaches. Direct SA_{NAM} predicts spectral acceleration directly at discrete periods that are well-explained by macroscopic predictors. Conversely, the stochastic simulation framework relies on predicting the underlying frequency parameters (f_U and f_L), which are inherently noisier, carry much higher aleatory uncertainty, and exhibit less statistical differentiation across components.

Despite this minor localized shift, the overall broadband spectral shape, energy levels, and long-period attenuation closely match across all three components, confirming the model's stability for multi-component hazard applications.

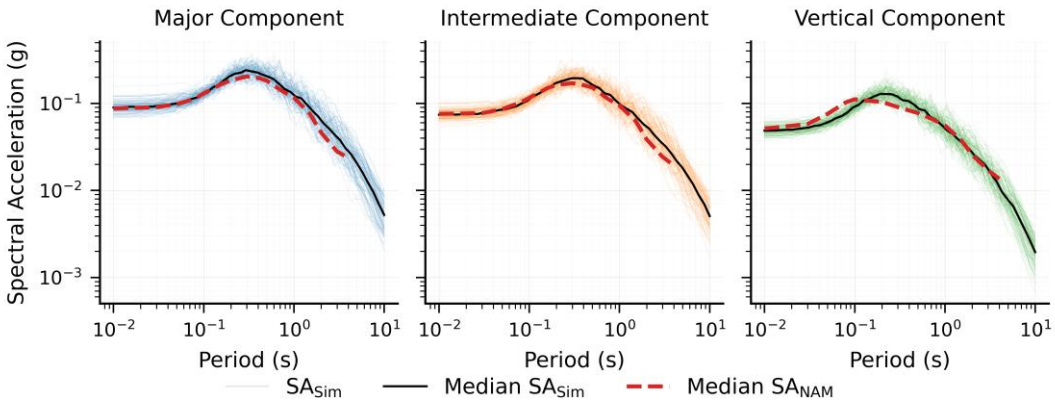


Figure 4.23. Comparison of spectral accelerations from stochastic simulations (SA_{Sim}) and the corresponding predicted empirical values (SA_{NAM}).

4.5.3. Validation Against Empirical GMMs

To evaluate the predictive performance of the proposed framework, the distribution of SA_{Sim} for the previously defined scenario was compared against established empirical GMMs. For visual clarity, the comparison was limited to two well-established reference models: Boore et al. (2014) [100], hereafter denoted as BSSA14, for the horizontal components, and Bozorgnia and Campbell (2016) [112], denoted as BC16, for the vertical component.

A minor conceptual distinction should be noted when interpreting the horizontal comparison. While BSSA14 and BC16 predict the orientation-independent median horizontal IM (known as RotD50), the proposed framework simulates orthogonal horizontal components expressed along their principal axes (major, intermediate, and vertical components). Consequently, the horizontal comparison should be regarded as a consistency benchmark rather than a direct one-to-one validation of identical IMs. Despite these differing metric definitions and slight variations in distance formulations, equivalent primary input parameters together with scenario-consistent default values for unspecified secondary parameters were used. The BSSA14 and BC16 predictions were obtained using the corresponding implementations provided by the OpenQuake Engine in Python.

To generate the simulation ensemble, 50 parameter realizations were sampled from the framework's covariance matrix (Σ_{total}), with exactly one stochastic time-series generated per sample. This approach couples the model's parametric covariance with the intrinsic variability of the stochastic simulation. The 16th, 50th (median), and 84th percentiles of the resulting simulations were then extracted and plotted against the median and standard deviation bounds of the reference GMMs as well as the SA_{NAM}.

As demonstrated in Figure 4.24, the SA_{Sim} replicates both the central tendency and the dispersion of the reference GMMs. The median SA_{Sim} closely tracks the GMM medians, confirming the macroscopic accuracy of the framework. Crucially, the intermediate component consistently exhibits lower spectral amplitudes than the major component, a characteristic feature that aligns with the principal axes of ground motion. Furthermore, the model's sampled uncertainty interval closely aligns with the uncertainty intervals predicted by the GMMs. These results indicate that, despite differences in component definitions and uncertainty formulations, the proposed framework reproduces the overall median scaling and variability expected from established empirical GMMs.

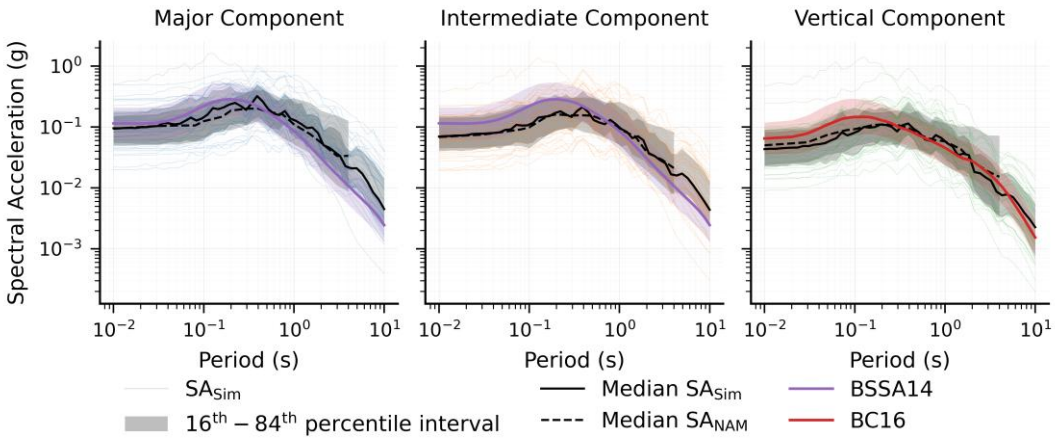


Figure 4.24. Comparison of spectral accelerations from stochastic simulations (SA_{Sim}), the corresponding predicted empirical values (SA_{NAM}), and predictions from reference ground motion models [100,112].

4.5.4. Conditional Simulation for Prescribed Hazard

While unconditional simulation validates the baseline predictive capabilities of the proposed framework, PBEE frameworks frequently require ground motion time-series conditioned on specific, extreme hazard targets (e.g., a 2% probability of exceedance in 50 years for $SA_{1.0s}$). Traditionally, this is achieved by selecting historical seed records and applying artificial spectral matching to force the waveform to meet the target. The proposed framework solves this complex inverse problem inherently through exact multivariate normal conditioning. Instead of altering a waveform after it is generated, the framework uses learned inter-parameter correlations to modify the physical simulation parameters prior to simulation.

Let the full response vector Y (comprising all response variables across the three principal axes) be partitioned into two subsets: the vector of target IMs to be conditioned upon (Y_{IM}), and the vector of the remaining simulation parameters and unconditioned IMs to be updated (Y_{α}). Their joint multivariate normal distribution is defined as:

$$\begin{bmatrix} Y_{\alpha} \\ Y_{IM} \end{bmatrix} \sim N\left(\begin{bmatrix} \mu_{\alpha} \\ \mu_{IM} \end{bmatrix}, \begin{bmatrix} \Sigma_{\alpha\,\alpha} & \Sigma_{\alpha\,IM} \\ \Sigma_{IM\,\alpha} & \Sigma_{IM\,IM} \end{bmatrix} \right) \tag{4.9}$$

Where μ and Σ denote the mean vector and covariance matrix of the joint distribution, respectively. When a specific target hazard level is prescribed such that $Y_{IM} = y_{target}$, the expected values of the associated remaining parameters are mathematically updated. The exact conditional mean ($\mu_{\alpha|IM}$) is computed as:

$$\mu_{\alpha|IM} = \mu_{\alpha} + \Sigma_{\alpha\,IM}\Sigma_{IM\,IM}^{-1}(y_{target} - \mu_{IM}) \tag{4.10}$$

Furthermore, because the framework captures the full covariance structure, conditioning on a known target inherently reduces the uncertainty of all correlated parameters. The updated, narrowed conditional covariance matrix ($\Sigma_{\alpha|IM}$) is computed as:

$$\Sigma_{\alpha|IM} = \Sigma_{\alpha\,\alpha} - \Sigma_{\alpha\,IM}\Sigma_{IM\,IM}^{-1}\Sigma_{IM\,\alpha} \tag{4.11}$$

This operation systematically and physically shifts the remaining parameters to accommodate the target hazard. For example, conditioning the model on an unusually high long-period SA will automatically use the covariances to increase the predicted total energy and adjust the dominant frequencies, ensuring the generated waveform is physically capable of producing that specific spectral demand. The framework then samples hazard-compatible simulation parameter vectors directly from the updated distribution:

$$Y_{\alpha|IM} \sim N(\mu_{\alpha|IM}, \Sigma_{\alpha|IM}) \tag{4.12}$$

Figure 4.25 provides a visual representation of this mathematical shift. For the previously defined earthquake scenario, the target $SA_{1.0s}$ was conditioned to a high hazard level, corresponding to an extreme deviation of 2 standard deviations above the median. The figure compares the median and uncertainty

bands of 50 unconditional and 50 conditional simulations. Under conditioning, the covariance structure shifts the correlated SAs upward across all three axes to satisfy the increased target demand. As expected, for the discrete empirical predictions (SA_{NAM}), the uncertainty band collapses exactly to zero at the 1.0 s conditioning period, reflecting the deterministic constraint imposed on that specific spectral ordinate.

In contrast, the SA_{Sim} ensemble retains stochastic variability even after conditioning. Because the final time-series are generated from an underlying stochastic white noise process, the uncertainty band does not collapse to zero at 1.0 s. Moreover, while the median of the conditional simulations is substantially elevated relative to the unconditional SA_{Sim}, it does not exactly replicate the sharp, isolated peak of the conditioned SA_{NAM} at the target period.

This behavior stems from the fundamental mechanics of the stochastic simulation method. The synthetic waveforms are governed by global physical parameters that define a smooth, average frequency filter ("spectral backbone"). The simulation cannot artificially isolate and inflate a single spectral period. Instead, it accommodates the target hazard by adjusting its global parameters, naturally distributing the increased energy demand across a broader frequency range. Unlike conventional time-series spectral matching approaches, which enforce an exact mathematical fit to a target spectrum, the proposed framework preserves broadband physical consistency and the inherent record-to-record stochasticity.

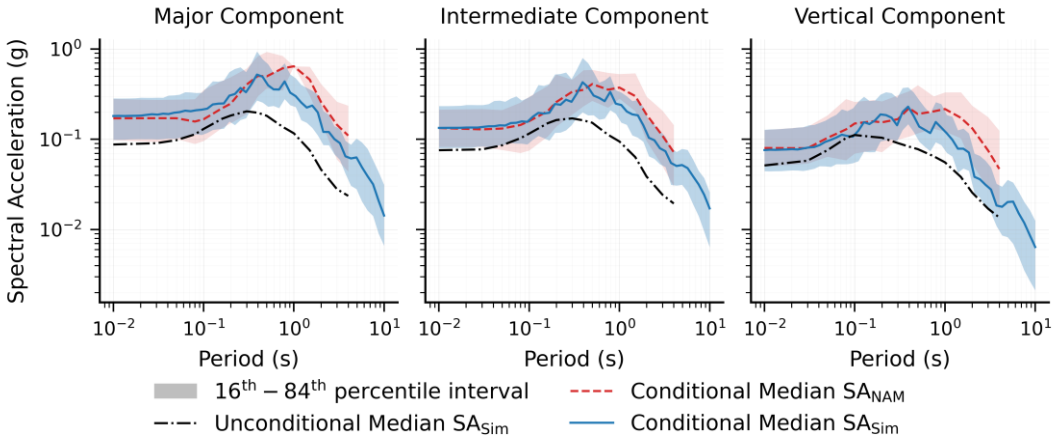


Figure 4.25. Comparison of spectral accelerations from stochastic simulations (SA_{Sim}) and the corresponding predicted empirical values (SA_{NAM}) conditioned on $SA_{1.0s}$ to +2 standard deviation, alongside unconditional SA_{Sim}.

Finally, Figure 4.26 illustrates the outcome of the conditional sampling process for the previously defined earthquake scenario. To isolate the effect of conditioning, the same underlying white noise sequence was used for both simulations. The resulting time-series confirm that the simulation parameters were consistently updated under the prescribed hazard at $SA_{1.0s}$, leading to an increase in the overall response amplitude and associated energy content. Compared with the unconditional realization, the conditioned simulation exhibits larger acceleration amplitudes, which propagate through integration to produce correspondingly larger velocity and displacement responses. Despite these amplitude changes, the overall temporal evolution of the ground motion remains broadly similar because both simulations originate from the same stochastic excitation. Since the conditioning is performed through the joint covariance structure of the simulation parameters, rather than by directly modifying the excitation, any changes in frequency content arise implicitly through the updated parameter values rather than from an explicit spectral adjustment.

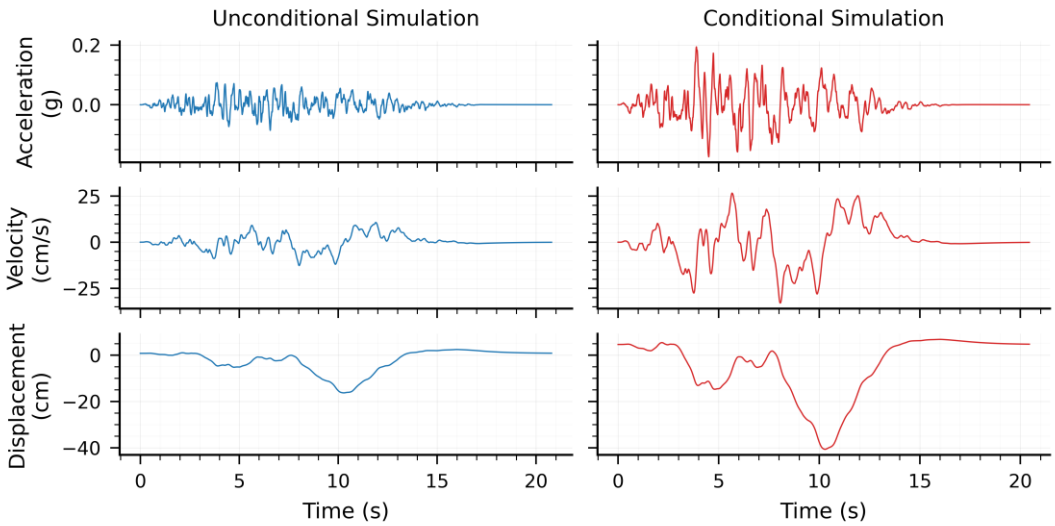


Figure 4.26. A direct comparison of unconditional versus conditional ground motion simulation.

4.6. Conclusions

This chapter integrated the broadband stochastic simulation method developed in Chapter 2 with the multivariate mixed-effects regression (MMER) framework established in Chapter 3, resulting in a unified generative model that directly links the prediction of intensity measures with the generation of hazard-compatible, three-component stochastic ground motion time-series.

A key component of this framework is the incorporation of a physics-informed neural additive model (NAM), which embeds fundamental seismological scaling relationships within the parameter prediction process. By combining physically constrained machine learning with a multivariate statistical structure, the framework provides stable predictions of stochastic simulation parameters while preserving the statistical dependencies required for three-component conditional simulation.

The resulting model enables the direct generation of broadband, physically coherent ground motion time-series that satisfy single or vector-valued hazard constraints without relying on historical seed records or artificial spectral matching procedures. In doing so, it establishes a unified pathway from seismological and site variables to hazard-compatible synthetic ground motions while preserving the natural stochastic variability required for performance-based earthquake engineering applications.

While the framework provides a robust end-to-end solution for conditional ground motion simulation, several limitations remain. These include constraints associated with the available empirical dataset, the representation of motions in principal axes rather than fault-relative orientations, and the current treatment of spectral nonstationarity. These broader limitations, together with the overarching scientific contributions and future research directions arising from this work, are discussed in Chapter 5.

Chapter 5
Conclusions and Future Research Directions

5.1. Introduction

The primary objective of this thesis was to bridge a critical gap in performance-based earthquake engineering (PBEE), specifically the disconnect between probabilistic seismic hazard targets and the simulation of physically coherent, hazard-compatible three-component (3C) ground motion time-series. To address this challenge, the core philosophy of this thesis has been fundamentally methodological rather than application-oriented. By systematically addressing both the realistic simulation of ground motions and the statistical prediction of their parameters, this research culminates in a unified, end-to-end generative framework. Ultimately, this thesis was designed to deliver a robust, generalized toolset, implemented as a suite of open-source Python packages and complemented by accessible graphical user interfaces, that enables the wider engineering community to conduct high-fidelity application studies and structural validations in the future. This chapter summarizes the core findings of this research, highlights its broader scientific impact, and outlines essential limitations that pave the way for future investigations.

5.2. Summary of Research Findings

The primary findings and methodological advancements of this research are drawn from the developments in Chapters 2, 3, and 4. The foundation of the proposed framework was established in Chapter 2, which introduced an enhanced, fully nonstationary site-based stochastic simulation method. A defining advancement of this method is its inherent modularity, which treats time modulation and frequency filtering as interchangeable, adaptable components. This flexibility allows for the application of multi-strong phase modulating functions to achieve high-fidelity reproductions of complex records, or simpler, single-strong phase functions to avoid over-parameterization and ensure numerical stability when building predictive models. Furthermore, the enhanced broadband filter function explicitly captures the low-frequency energy content characteristic, often associated with near-fault pulse-like and deep-basin ground motions without relying on artificial post-processing corrections. By preserving these energy characteristics natively, the method provides a highly adaptable generative tool that can be tailored to diverse earthquake scenarios capable of representing multiple strong motion phases and low-frequency content.

To transition the simulation tool into a predictive, scenario-specific engine, Chapter 3 developed a modular multivariate mixed-effects regression (MMER) framework. A defining feature of this statistical architecture is that it is intentionally agnostic to the specification of the fixed-effects component. This flexibility allows the framework to seamlessly integrate conventional parametric functions or nonparametric machine learning algorithms, such as artificial neural networks (ANNs), to capture complex nonlinear scaling behaviors directly from empirical data. Furthermore, the framework simultaneously models multiple correlated intensity measures while accommodating various nested or crossed grouping factors. This enables the rigorous decomposition of total aleatory uncertainty into distinct partitions, such as between-event, between-site, and within-event residual components. Finally, to address the challenge of evaluating statistical stability when using machine learning models, the framework incorporates nonparametric cluster bootstrapping, providing a robust mathematical capability to quantify the associated epistemic uncertainty in both median predictions and variance structures.

Building upon the former developments, Chapter 4 integrated the physical and statistical domains. While using the core stochastic simulation method established in Chapter 2, Chapter 4 intentionally

adopted a streamlined, parsimonious parameter configuration, constraining the formulation to stationary dominant frequencies and a single dominant energy phase, to ensure the numerical stability required for high-dimensional predictive modeling. By embedding a physics-informed neural additive model (NAM) within the MMER structure, the research established a stable predictive baseline that explicitly respects seismological scaling laws (such as magnitude saturation and distance attenuation). The resulting unified model successfully extracts complete inter-component covariance matrices, enabling three-component conditional simulation. Consequently, the framework generates broadband, physically realistic waveforms that satisfy target hazards without the need for historical seed records or artificial time-domain spectral matching.

5.3. Broad Scientific Impact and Open-Source Software

The integration of physically constrained machine learning with hierarchical statistical modeling introduces several key contributions to the field of earthquake engineering:

Advancement of Conditional Simulation: The proposed framework eliminates the reliance on artificial spectral matching and historical seed record scaling. By mathematically adjusting global stochastic simulation parameters to satisfy vector-valued target hazards, the model rigorously preserves the natural record-to-record variability essential for robust structural response history analyses.

Physics-Informed Machine Learning for Sparse Datasets: By enforcing architectural monotonicity within the NAM, this research demonstrates how embedded seismological domain knowledge can prevent the overfitting and non-physical predictions that often arise in unconstrained machine learning models when applied to highly curated, sparse empirical datasets (e.g., a small subset of the NGA-West2 database).

Open-Source Contributions to the Scientific Community: To ensure reproducibility and facilitate immediate adoption by researchers and practicing engineers, the core methodologies developed in this thesis have been released as a suite of open-source Python packages complemented by accessible graphical user interfaces. These tools are actively maintained, available on PyPI, and archived on Zenodo:

- **SGSIM (Simulation and Analysis of Ground Motions):** A modular, high-performance, object-oriented package for general ground motion analysis, processing, filtering, and the extraction of intensity measures and signal attributes such as Fourier Amplitude Spectrum (FAS). It also implements the broadband stochastic simulation method as described in Chapter 2.
  GitHub: https://github.com/Sajad-Hussaini/SGSIM
  PyPI: https://pypi.org/project/sgsim
  Online Documentation: https://sgsim.readthedocs.io
  DOI: 10.5281/zenodo.14565922)

- **MMER (Multivariate Mixed-Effects Regression):** A modular, high-performance, object-oriented, domain-agnostic statistical package for hierarchical and longitudinal data analysis. It enables the specification of flexible fixed effects, including both parametric models and machine learning algorithms, within a unified multivariate mixed-effects framework as described in Chapter 3.
  GitHub: https://github.com/Sajad-Hussaini/mmer
  PyPI: https://pypi.org/project/mmer
  Online Documentation: https://mmer.readthedocs.io
  DOI: 10.5281/zenodo.18068839

- **PINAGMM (Physics-Informed Neural Additive Ground Motion Model):** A deployed framework implementing the hazard-compatible three-component ground motion simulation model described in Chapter 4. The framework includes a high-performance web-based graphical user interface that enables users to configure simulation parameters, execute simulations, visualize results, and export generated ground motions and associated outputs for further analysis when run locally. In addition, a publicly accessible demonstration instance of the same web application is provided, allowing users to explore the framework without requiring local installation of Python or its dependencies. The demonstration application is hosted on an on-demand cloud service; consequently, the first request after periods of inactivity may require a few minutes to initialize the hosting environment before the application becomes available. This startup delay is solely related to the hosting environment and does not reflect the computational performance of the PINAGMM framework.
  GitHub: https://github.com/Sajad-Hussaini/pinagmm
  DOI: 10.5281/zenodo.20746843
  Demo Web Application: https://pinagmm.onrender.com

5.4. Limitations and Future Research Directions

While the developed framework provides a robust solution for scenario-specific ground motion generation, certain constraints were necessary to ensure model stability and simplicity. These limitations also define clear directions for future research aimed at improving physical realism and general applicability:

- **Empirical Dataset Dependencies and Ergodicity:** The current framework is calibrated on a rigorously filtered subset of the NGA-West2 database. Consequently, the model is inherently ergodic, predicting the average ground motion for generalized site conditions (via V_{S30}) rather than modeling true, non-ergodic localized 3D geology.
- **Spatial Orientation Assumptions:** The current model generates ground motions in statistically derived principal axes. While mathematically efficient for decoupling orthogonal components, these axes are not explicitly tied to physical fault geometries (e.g., fault-normal and fault-parallel orientations), nor are they explicitly conditioned on modern orientation-independent median metrics (e.g., RotD50). However, from a practical design perspective, this constraint does not limit engineering utility. Because the horizontal components are generated as an orthogonal, statistically uncorrelated pair, they can be readily rotated using standard coordinate transformations into any arbitrary direction. This allows practicing engineers to align the synthetic time-series directly with the principal axes, or the strong and weak structural directions, of a target civil engineering system under evaluation.
- **Spectral Stationarity:** The stochastic formulation adopted in Chapter 5 for the proposed generative framework assumes stationary dominant frequencies for a specified earthquake scenario. This should not be interpreted as a limitation of the underlying stochastic simulation methodology presented in Chapter 2, which can accommodate spectral non-stationarity. Rather, this modeling choice was deliberately adopted to avoid over-parameterization and overfitting to the highly scattered, localized time-frequency variations observed in individual empirical records. At present, simplistic time-varying functions have not demonstrated sufficient robustness for reliable global ground motion modeling.

These limitations highlight key opportunities for further development. Future studies should focus on the following advancements:

- **Expansion of the Predictor Space for Improved Model Resolution:** The current framework uses a parsimonious set of five primary predictors to maintain interpretability and support practical use in engineering applications where more complex seismological parameters may not be readily available. Future work may extend this set to align more closely with modern ground motion models by incorporating additional seismological variables, such as hanging-wall effects, rupture geometry (e.g., rupture width), and basin response metrics (e.g., $Z_{1.0}$ or $Z_{2.5}$). These extensions may improve the representation of source, path, and site effects and reduce unexplained variability.
- **Transitioning Toward Non-Ergodic Modeling:** The hierarchical nature of the developed MMER framework naturally lends itself to non-ergodic ground motion modeling. Future research could introduce region-specific or site-specific random effects to relax the ergodic assumption, providing localized hazard assessments.
- **Robust Nonstationary Parameterizations:** Investigating stable, time-varying frequency parameterizations will be vital to capture pronounced record-specific spectral nonstationarity. Solving this will enable fully nonstationary simulations, which are critical for high-fidelity seismic risk evaluations of narrow-band structures.
- **Structural Response and PBEE Validation:** Although the proposed framework was developed to support nonlinear response history analysis within PBEE, the present study focuses on the development and ground motion level validation of the generative methodology. A systematic evaluation of its influence on structural response, engineering demand parameters, fragility functions, and seismic risk estimates, relative to conventional record-selection and spectrum-matching procedures, remains an important direction for future research.

References

1. Yang TY, Moehle J, Stojadinovic B, Der Kiureghian A. Seismic Performance Evaluation of Facilities: Methodology and Implementation. Journal of Structural Engineering 2009; 135(10): 1146–1154. DOI: 10.1061/(ASCE)0733-9445(2009)135:10(1146).
2. Baker JW, Cornell CA. Vector-valued Intensity Measures Incorporating Spectral Shape For Prediction of Structural Response. Journal of Earthquake Engineering 2008; 12(4): 534–554. DOI: 10.1080/13632460701673076.
3. Vamvatsikos D, Cornell CA. Incremental dynamic analysis. Earthquake Engineering & Structural Dynamics 2002; 31(3): 491–514. DOI: 10.1002/eqe.141.
4. Hussaini SMS, Karimzadeh S, Rezaeian S, Lourenço PB. Broadband stochastic simulation of earthquake ground motions with multiple strong phases with an application to the 2023 Kahramanmaraş, Turkey (Türkiye), earthquake. Earthquake Spectra 2025: 87552930251331981. DOI: 10.1177/87552930251331981.
5. EN 1998-1. Eurocode 8: Design of structures for earthquake resistance - Part 1: General rules, seismic actions and rules for buildings. vol. 50. Brussels: European Committee for Standardization; 2004.
6. Kallioras S, Graziotti F, Magenes G. Vertical accelerations in seismic analysis: A numerical investigation of their effects on URM structures. Earthquake Spectra 2025: 87552930251348482. DOI: 10.1177/87552930251348482.
7. Phung VB, Abrahamson NA, Huang BS, Loh CH. Vertical ground-motion prediction equation and the vertical-to-horizontal spectral ratio for crustal earthquakes in Taiwan. Earthquake Spectra 2022: 875529302110611. DOI: 10.1177/87552930211061168.
8. Rezaeian S, Stewart JP, Luco N, Goulet CA. Findings from a decade of ground motion simulation validation research and a path forward. Earthquake Spectra 2024; 40(1): 346–378. DOI: 10.1177/87552930231212475.
9. Yamamoto Y, Baker JW. Stochastic model for earthquake ground motion using wavelet packets. Bulletin of the Seismological Society of America 2013; 103(6): 3044–3056. DOI: 10.1785/0120120312.
10. Hancock J, Watson-Lamprey J, Abrahamson NA, Bommer JJ, Markatis A, McCoyh E, et al. An improved method of matching response spectra of recorded earthquake ground motion using wavelets. Journal of Earthquake Engineering 2006; 10(sup001): 67–89. DOI: 10.1080/13632460609350629.
11. Watson-Lamprey J, Abrahamson N. Selection of ground motion time series and limits on scaling. Soil Dynamics and Earthquake Engineering 2006; 26(5): 477–482. DOI: 10.1016/j.soildyn.2005.07.001.
12. Luco N, Bazzurro P. Does amplitude scaling of ground motion records result in biased nonlinear structural drift responses? Earthquake Engineering & Structural Dynamics 2007; 36(13): 1813–1835. DOI: 10.1002/eqe.695.
13. Naeim F, Lew M. On the use of design spectrum compatible time histories. Earthquake Spectra 1995; 11(1): 111–127. DOI: 10.1193/1.1585805.
14. Arslan Kelam A, Karimzadeh S, Yousefibavil K, Akgün H, Askan A, Erberik MA, et al. An evaluation of seismic hazard and potential damage in Gaziantep, Turkey using site specific models for sources, velocity structure and building stock. Soil Dynamics and Earthquake Engineering 2022; 154: 107129. DOI: 10.1016/j.soildyn.2021.107129.
15. Askan A, Karimzadeh S, Bilal M. Seismic intensity maps for the eastern part of the north Anatolian fault zone (Turkey) based on recorded and simulated ground-motion data 2017: 273–287. DOI: 10.1002/9781118944998.ch10.
16. Bernardo V, Karimzadeh S, Caicedo D, Hussaini SMS, Lourenco P. Fragility-Based Seismic Assessment of Traditional Masonry Buildings on Azores (Portugal) Using Simulated Ground Motion Records. Earthquake Spectra 2024. DOI: https://doi.org/10.1177/87552930241256287.
17. Fayaz J, Rezaeian S, Zareian F. Evaluation of simulated ground motions using probabilistic seismic demand analysis: CyberShake (ver. 15.12) simulations for Ordinary Standard Bridges. Soil Dynamics and Earthquake Engineering 2021; 141: 106533. DOI: 10.1016/j.soildyn.2020.106533.

18. Karimzadeh S, Funari MF, Szabó S, Hussaini SMS, Rezaeian S, Lourenço PB. Stochastic simulation of earthquake ground motions for the seismic assessment of monumental masonry structures: Source-based vs site-based approaches. Earthquake Engineering & Structural Dynamics 2024; 53(1): 303–330. DOI: 10.1002/eqe.4012.
19. Rezaeian S, Hartzell S, Sun X, Mendoza C. Simulation of earthquake ground motions in the eastern United States using deterministic physics-based and site-based stochastic approaches. Bulletin of the Seismological Society of America 2017; 107(1): 149–168. DOI: 10.1785/0120160031.
20. Hariri-Ardebili MA, Rezaeian S. Utilization of stochastic ground motion simulations for scenario-based performance assessment of geo-structures. Reliability Engineering & System Safety 2024; 251: 110375. DOI: 10.1016/J.RESS.2024.110375.
21. Douglas J, Aochi H. A survey of techniques for predicting earthquake ground motions for engineering purposes. Surveys in Geophysics 2008; 29(3): 187–220. DOI: 10.1007/s10712-008-9046-y.
22. Rezaeian S, Sun X. Stochastic ground motion simulation. Encyclopedia of Earthquake Engineering 2014: 1–15. DOI: 10.1007/978-3-642-36197-5_239-1.
23. Beresnev IA, Atkinson GM. Modeling finite-fault radiation from the ω_n spectrum. Bulletin of the Seismological Society of America 1997; 87(1): 67–84. DOI: 10.1785/BSSA0870010067.
24. Hartzell SH. Earthquake aftershocks as Green's functions. Geophysical Research Letters 1978; 5(1): 1–4. DOI: 10.1029/GL005i001p00001.
25. Hartzell S. Calculation of broadband time histories of ground motion, part ii: kinematic and dynamic modeling using theoretical green's functions and comparison with the 1994 Northridge earthquake. Bulletin of the Seismological Society of America 2005; 95(2): 614–645. DOI: 10.1785/0120040136.
26. Zeng Y, Anderson JG, Yu G. A composite source model for computing realistic synthetic strong ground motions. Geophysical Research Letters 1994; 21(8): 725–728. DOI: 10.1029/94GL00367.
27. Komatitsch D. Simulations of ground motion in the Los Angeles basin based upon the spectral-element method. Bulletin of the Seismological Society of America 2004; 94(1): 187–206. DOI: 10.1785/0120030077.
28. Kristek J. Seismic-wave propagation in viscoelastic media with material discontinuities: a 3D fourth-order staggered-grid finite-difference modeling. Bulletin of the Seismological Society of America 2003; 93(5): 2273–2280. DOI: 10.1785/0120030023.
29. Boore DM. Simulation of ground motion using the stochastic method. Pure and Applied Geophysics 2003; 160(3): 635–676. DOI: 10.1007/PL00012553.
30. Motazedian D, Atkinson GM. Stochastic Finite-Fault Modeling Based on a Dynamic Corner Frequency. Bulletin of the Seismological Society of America 2005; 95(3): 995–1010. DOI: 10.1785/0120030207.
31. Rezaeian S, Der Kiureghian A. A stochastic ground motion model with separable temporal and spectral nonstationarities. Earthquake Engineering & Structural Dynamics 2008; 37(13): 1565–1584. DOI: 10.1002/eqe.831.
32. Boore DM. Comparing stochastic point-source and finite-source ground-motion simulations: SMSIM and EXSIM. Bulletin of the Seismological Society of America 2009; 99(6): 3202–3216. DOI: 10.1785/0120090056.
33. Chouet B, Aki K, Tsujiura M. Regional variation of the scaling law of earthquake source spectra. Bulletin of the Seismological Society of America 1978; 68(1): 49–79. DOI: 10.1785/BSSA0680010049.
34. Stafford PJ, Sgobba S, Marano GC. An energy-based envelope function for the stochastic simulation of earthquake accelerograms. Soil Dynamics and Earthquake Engineering 2009; 29(7): 1123–1133. DOI: 10.1016/j.soildyn.2009.01.003.
35. Wang F, Zhang Y, Yang B, Lin X, Ba Z. Stochastic finite fault simulation of 2023 Mw 7.8 and Mw 7.5 Turkey earthquakes and its application to regional buildings damage estimation at Kahramanmaras City. Bulletin of Earthquake Engineering 2024: 1–26. DOI: 10.1007/S10518-024-01990-1/FIGURES/17.
36. Graves RW, Pitarka A. Broadband ground-motion simulation using a hybrid approach. Bulletin of the Seismological Society of America 2010; 100(5A): 2095–2123. DOI: 10.1785/0120100057.
37. Burks LS, Baker JW. Validation of ground-motion simulations through simple proxies for the response of engineered systems. Bulletin of the Seismological Society of America 2014; 104(4): 1930–1946. DOI: 10.1785/0120130276.

38. Smerzini C, Amendola C, Paolucci R, Bazrafshan A. Engineering validation of BB-SPEEDset, a data set of near-source physics-based simulated accelerograms. Earthquake Spectra 2024; 40(1): 420–445. DOI: 10.1177/87552930231206766.
39. Alamilla J, Esteva L, García-Pérez J, Díaz-López O. Evolutionary properties of stochastic models of earthquake accelerograms: Their dependence on magnitude and distance. Journal of Seismology 2001 5:1 2001; 5(1): 1–21. DOI: 10.1023/A:1009892002555.
40. Dabaghi M, Der Kiureghian A. Stochastic model for simulation of near-fault ground motions. Earthquake Engineering & Structural Dynamics 2017; 46(6): 963–984. DOI: 10.1002/eqe.2839.
41. Waezi Z, Rofooei FR, Hashemi MJ. A multi-peak evolutionary model for stochastic simulation of ground motions based on time-domain features. Journal of Earthquake Engineering 2021; 25(2): 343–379. DOI: 10.1080/13632469.2018.1518279.
42. Lin YK. On random pulse train and its evolutionary spectral representation. Probabilistic Engineering Mechanics 1986; 1(4): 219–223. DOI: 10.1016/0266-8920(86)90015-9.
43. Sgobba S, Stafford PJ, Marano GC, Guaragnella C. An evolutionary stochastic ground-motion model defined by a seismological scenario and local site conditions. Soil Dynamics and Earthquake Engineering 2011; 31(11): 1465–1479. DOI: 10.1016/j.soildyn.2011.05.014.
44. Huang D, Wang G. Energy-compatible and spectrum-compatible (ECSC) ground motion simulation using wavelet packets. Earthquake Engineering & Structural Dynamics 2017; 46(11): 1855–1873. DOI: 10.1002/eqe.2887.
45. Vlachos C, Papakonstantinou KG, Deodatis G. A multi-modal analytical non-stationary spectral model for characterization and stochastic simulation of earthquake ground motions. Soil Dynamics and Earthquake Engineering 2016; 80: 177–191. DOI: 10.1016/j.soildyn.2015.10.006.
46. Alimoradi A, Beck JL. Machine-learning methods for earthquake ground motion analysis and simulation. Journal of Engineering Mechanics 2015; 141(4): 04014147. DOI: 10.1061/(ASCE)EM.1943-7889.0000869.
47. Tamhidi A, Kuehn N, Ghahari SF, Rodgers AJ, Kohler MD, Taciroglu E, et al. Conditioned simulation of ground-motion time series at uninstrumented sites using Gaussian process regression. Bulletin of the Seismological Society of America 2022; 112(1): 331–347. DOI: 10.1785/0120210054.
48. Rezaeian S, Der Kiureghian A. Simulation of orthogonal horizontal ground motion components for specified earthquake and site characteristics. Earthquake Engineering & Structural Dynamics 2012; 41(2): 335–353. DOI: 10.1002/eqe.1132.
49. Waezi Z, Balzadeh S. Simulation of near-field pulse-like ground motions using a correlated bimodal fractional stochastic model. Soil Dynamics and Earthquake Engineering 2022; 161: 107434. DOI: 10.1016/j.soildyn.2022.107434.
50. Akkar S, Sandıkkaya MA, Ay BÖ. Compatible ground-motion prediction equations for damping scaling factors and vertical-to-horizontal spectral amplitude ratios for the broader Europe region. Bulletin of Earthquake Engineering 2014; 12(1): 517–547. DOI: 10.1007/s10518-013-9537-1.
51. Chiou BSJ, Youngs RR. Update of the Chiou and Youngs NGA Model for the Average Horizontal Component of Peak Ground Motion and Response Spectra. Earthquake Spectra 2014; 30(3): 1117–1153. DOI: 10.1193/072813EQS219M.
52. Sedaghati F, Pezeshk S. Machine learning–based ground motion models for shallow crustal earthquakes in active tectonic regions. Earthquake Spectra 2023; 39(4): 2406–2435. DOI: 10.1177/87552930231191759.
53. Campbell KW, Bozorgnia Y. Empirical ground-motion models for horizontal Fourier amplitude spectra from fixed-effects and mixed-effects analyses of the NGA-West2 database. Earthquake Spectra 2025: 87552930241312708. DOI: 10.1177/87552930241312708.
54. Ji K, Karimzadeh S, Yaghmaei-Sabegh S, Hou R, Carvalho A, Lourenço PB. Ground motion model using simulated scenario earthquake records in Azores Plateau (Portugal) at bedrock. Soil Dynamics and Earthquake Engineering 2025; 197: 109521. DOI: 10.1016/j.soildyn.2025.109521.
55. Karimzadeh S, Mohammadi A, Hussaini SMS, Caicedo D, Askan A, Lourenço PB. ANN-based ground motion model for Turkey using stochastic simulation of earthquakes. Geophysical Journal International 2023; 236(1): 413–429. DOI: 10.1093/gji/ggad432.

56. Campbell KW, Bozorgnia Y, Kuehn NM. Revision of empirical NGA-West2 horizontal ground-motion models using fixed-effects and mixed-effects regression and Bayesian inference. Bulletin of Earthquake Engineering 2025. DOI: 10.1007/s10518-025-02218-6.
57. Sriwastav RK, Yedulla J, Raghukanth STG. A non-parametric model of ground motion parameters for shallow crustal earthquakes in Europe. Soil Dynamics and Earthquake Engineering 2024; 186: 108923. DOI: 10.1016/j.soildyn.2024.108923.
58. Kotha SR, Weatherill G, Bindi D, Cotton F. A regionally-adaptable ground-motion model for shallow crustal earthquakes in Europe. Bulletin of Earthquake Engineering 2020; 18(9): 4091–4125. DOI: 10.1007/s10518-020-00869-1.
59. Baker JW, Jayaram N. Correlation of Spectral Acceleration Values from NGA Ground Motion Models. Https://DoiOrg/101193/12857544 2008; 24(1): 299–317. DOI: 10.1193/1.2857544.
60. Baker JW, Bradley BA. Intensity Measure Correlations Observed in the NGA-West2 Database, and Dependence of Correlations on Rupture and Site Parameters. Earthquake Spectra 2017; 33(1): 145–156. DOI: 10.1193/060716eqs095m.
61. Cimellaro GP. Correlation in spectral accelerations for earthquakes in Europe. Earthquake Engineering & Structural Dynamics 2013; 42(4): 623–633. DOI: 10.1002/eqe.2248.
62. Kuehn NM, Kishida T, AlHamaydeh M, Lavrentiadis G, Bozorgnia Y. A Bayesian model for truncated regression for the estimation of empirical ground-motion models. Bulletin of Earthquake Engineering 2020; 18(14): 6149–6179. DOI: 10.1007/s10518-020-00943-8.
63. Kuehn NM, Scherbaum F. Ground-motion prediction model building: a multilevel approach. Bulletin of Earthquake Engineering 2015; 13(9): 2481–2491. DOI: 10.1007/s10518-015-9732-3.
64. Arroyo D, Ordaz M. Multivariate Bayesian Regression Analysis Applied to Ground-Motion Prediction Equations, Part 1: Theory and Synthetic Example. Bulletin of the Seismological Society of America 2010; 100(4): 1551–1567. DOI: 10.1785/0120080354.
65. Arroyo D, Ordaz M. Multivariate Bayesian Regression Analysis Applied to Ground-Motion Prediction Equations, Part 2: Numerical Example with Actual Data. Bulletin of the Seismological Society of America 2010; 100(4): 1568–1577. DOI: 10.1785/0120090320.
66. Bortolotti T, Peli R, Lanzano G, Sgobba S, Menafoglio A. Weighted Functional Data Analysis for the Calibration of a Ground Motion Model in Italy. Journal of the American Statistical Association 2024; 119(547): 1697–1708. DOI: 10.1080/01621459.2023.2300506.
67. Dabaghi M, Der Kiureghian A. Simulation of orthogonal horizontal components of near-fault ground motion for specified earthquake source and site characteristics. Earthquake Engineering & Structural Dynamics 2018; 47(6): 1369–1393. DOI: 10.1002/eqe.3021.
68. Khosravikia F, Clayton P. Machine learning in ground motion prediction. Computers & Geosciences 2021; 148: 104700. DOI: 10.1016/J.CAGEO.2021.104700.
69. Temiz C, Hussaini SMS, Karimzadeh S, Askan A, Lourenço PB. Seismic scenario simulation and ANN-based ground motion model development on the North Tabriz Fault in Northwest Iran. Journal of Seismology 2025; 29(1): 147–169. DOI: 10.1007/s10950-024-10264-x.
70. Karimzadeh S, Mohammadi A, Salahuddin U, Carvalho A, Lourenço PB. Backbone ground motion model through simulated records and XGBoost machine learning algorithm: An application for the Azores plateau (Portugal). Earthquake Engineering & Structural Dynamics 2023. DOI: 10.1002/EQE.4040.
71. Brillinger DR, Preisler HK. Further analysis of the Joyner-Boore attenuation data. Bulletin of the Seismological Society of America 1985; 75(2): 611–614. DOI: 10.1785/BSSA0750020611.
72. Abrahamson NA, Youngs RR. A stable algorithm for regression analyses using the random effects model. Bulletin of the Seismological Society of America 1992; 82(1): 505–510. DOI: 10.1785/BSSA0820010505.
73. Jayaram N, Baker JW. Considering Spatial Correlation in Mixed-Effects Regression and the Impact on Ground-Motion Models. Bulletin of the Seismological Society of America 2010; 100(6): 3295–3303. DOI: 10.1785/0120090366.
74. Mohammadi A, Karimzadeh S, Amir S, Ozsarac V, Lourenço PB. The potential of region-specific machine-learning-based ground motion models: Application to Turkey. Soil Dynamics and Earthquake Engineering 2023; 172(January): 108008. DOI: 10.1016/J.SOILDYN.2023.108008.
75. Bates D, Mächler M, Bolker B, Walker S. Fitting Linear Mixed-Effects Models Using lme4. Journal of Statistical Software 2015; 67(1). DOI: 10.18637/jss.v067.i01.

76. Derras B, Bard PY, Cotton F. Towards fully data driven ground-motion prediction models for Europe. Bulletin of Earthquake Engineering 2014; 12(1): 495–516. DOI: 10.1007/s10518-013-9481-0.
77. Meenakshi Y, Vemula S, Alne A, Raghukanth S. Ground motion model for Peninsular India using an artificial neural network. Earthquake Spectra 2023; 39(1): 596–633. DOI: 10.1177/87552930221144330.
78. Yanni H, Fragiadakis M, Mitseas IP. Wavelet-Based Stochastic Model for the Generation of Fully Nonstationary Bidirectional Seismic Accelerograms. Earthquake Engineering & Structural Dynamics 2025: eqe.4315. DOI: 10.1002/eqe.4315.
79. Olsen KB, Mayhew JE. Goodness-of-fit criteria for broadband synthetic seismograms, with application to the 2008 mw 5.4 Chino Hills, California, earthquake. Seismological Research Letters 2010; 81(5): 715–723. DOI: 10.1785/gssrl.81.5.715.
80. Luzi L, Puglia R, Russo E, D'Amico M, Felicetta C, Pacor F, et al. The engineering strong-motion database: A platform to access pan-European accelerometric data. Seismological Research Letters 2016; 87(4): 987–997. DOI: 10.1785/0220150278.
81. Wu F, Xie J, An Z, Lyu C, Taymaz T, Irmak TS, et al. Pulse-like ground motion observed during the 6 February 2023 MW7.8 Pazarcık Earthquake (Kahramanmaraş, SE Türkiye). Earthquake Science 2023; 36(4): 328–339. DOI: 10.1016/J.EQS.2023.05.005.
82. Baker JW. Quantitative Classification of Near-Fault Ground Motions Using Wavelet Analysis. Bulletin of the Seismological Society of America 2007; 97(5): 1486–1501. DOI: 10.1785/0120060255.
83. Ancheta TD, Darragh RB, Stewart JP, Seyhan E, Silva WJ, Chiou BSJ, et al. NGA-West2 Database. Earthquake Spectra 2014; 30(3): 989–1005. DOI: 10.1193/070913EQS197M.
84. Shahi SK, Baker JW. An Efficient Algorithm to Identify Strong-Velocity Pulses in Multicomponent Ground Motions. Bulletin of the Seismological Society of America 2014; 104(5): 2456–2466. DOI: 10.1785/0120130191.
85. Rezaeian S, Der Kiureghian A. Simulation of synthetic ground motions for specified earthquake and site characteristics. Earthquake Engineering & Structural Dynamics 2010; 39(10): 1155–1180. DOI: 10.1002/eqe.997.
86. Housner GW, Jennings PC. Generation of artificial earthquakes. Journal of the Engineering Mechanics Division 1964; 90(1): 113–150. DOI: 10.1061/JMCEA3.0000448.
87. Rodolfo Saragoni G, Hart GC. Simulation of artificial earthquakes. Earthquake Engineering & Structural Dynamics 1973; 2(3): 249–267. DOI: 10.1002/eqe.4290020305.
88. Su M, Dabaghi M, Broccardo M. The importance of corner frequency in site-based stochastic ground motion models. Earthquake Engineering & Structural Dynamics 2024; 53(10): 3318–3329. DOI: 10.1002/EQE.4139.
89. Safak E, Boore DM. On low-frequency errors of uniformly modulated filtered white-noise models for ground motions. Earthquake Engineering & Structural Dynamics 1988; 16(3): 381–388. DOI: 10.1002/eqe.4290160307.
90. Amin M, Ang AHS. Nonstationary stochastic models of earthquake motions. Journal of the Engineering Mechanics Division 1968; 94(2): 559–584. DOI: 10.1061/JMCEA3.0000969.
91. Shinozuka M, Sato Y. Simulation of nonstationary random process. Journal of the Engineering Mechanics Division 1967; 93(1): 11–40. DOI: 10.1061/JMCEA3.0000822.
92. Broccardo M, Dabaghi M. Preliminary validation of a spectral-based stochastic ground motion model with a non-parametric time-modulating function, 2019. DOI: 10.22725/ICASP13.187.
93. Yeh CH, Wen YK. Modeling of nonstationary ground motion and analysis of inelastic structural response. Structural Safety 1990; 8(1–4): 281–298. DOI: 10.1016/0167-4730(90)90046-R.
94. Lutes LD, Sarkani S. Frequency, Bandwidth, and Amplitude. Random Vibrations, Elsevier; 2004. DOI: 10.1016/B978-075067765-3/50007-4.
95. Shannon CE. Communication in the presence of noise. Proceedings of the IRE 1949; 37(1): 10–21. DOI: 10.1109/JRPROC.1949.232969.
96. Karimzadeh S. Seismological and engineering demand misfits for evaluating simulated ground motion records. Applied Sciences 2019; 9(21): 4497. DOI: 10.3390/app9214497.

97. Goulet CA, Abrahamson NA, Somerville PG, Wooddell KE. The SCEC broadband platform validation exercise: methodology for code validation in the context of seismic-hazard analyses. Seismological Research Letters 2015; 86(1): 17–26. DOI: 10.1785/0220140104.
98. Hulin W, Jin-Ting Z. Nonparametric Regression Methods for Longitudinal Data Analysis: Mixed-Effects Modeling Approaches. 1st ed. Wiley; 2006. DOI: 10.1002/0470009675.
99. Boore DM. Orientation-Independent, Nongeometric-Mean Measures of Seismic Intensity from Two Horizontal Components of Motion. Bulletin of the Seismological Society of America 2010; 100(4): 1830–1835. DOI: 10.1785/0120090400.
100. Boore DM, Stewart JP, Seyhan E, Atkinson GM. NGA-West2 equations for predicting PGA, PGV, and 5% damped PSA for shallow crustal earthquakes. Earthquake Spectra 2014; 30(3): 1057–1085. DOI: 10.1193/070113EQS184M.
101. Hinton GE. CONNECTIONIST LEARNING PROCEDURES. Machine Learning, Elsevier; 1990. DOI: 10.1016/B978-0-08-051055-2.50029-8.
102. Akiba T, Sano S, Yanase T, Ohta T, Koyama M. Optuna: A Next-generation Hyperparameter Optimization Framework. Proceedings of the 25th ACM SIGKDD International Conference on Knowledge Discovery and Data Mining, 2019.
103. Lundberg SM, Lee SI. A unified approach to interpreting model predictions. Advances in Neural Information Processing Systems 2017; 30.
104. Brune JN. Tectonic stress and the spectra of seismic shear waves from earthquakes. Journal of Geophysical Research 1970; 75(26): 4997–5009. DOI: 10.1029/JB075i026p04997.
105. Afshari K, Stewart JP. Physically Parameterized Prediction Equations for Significant Duration in Active Crustal Regions. Earthquake Spectra 2016; 32(4): 2057–2081. DOI: 10.1193/063015EQS106M.
106. Travasarou T, Bray JD, Abrahamson NA. Empirical attenuation relationship for Arias Intensity. Earthquake Engineering & Structural Dynamics 2003; 32(7): 1133–1155. DOI: 10.1002/EQE.270.
107. Pitarka A, Dalguer LA, Day SM, Somerville PG, Dan K. Numerical Study of Ground-Motion Differences between Buried-Rupturing and Surface-Rupturing Earthquakes. Bulletin of the Seismological Society of America 2009; 99(3): 1521–1537. DOI: 10.1785/0120080193.
108. Hisada Y. Broadband strong motion simulation in layered half-space using stochastic Green's function technique. Journal of Seismology 2008; 12(2): 265–279. DOI: 10.1007/s10950-008-9090-6.
109. Smerzini C, Paolucci R, Sgobba S, Ramadan F. Vertical Seismic Action for Design: Developments for the Next Generation of European and Italian Norms. Earthquake Engineering & Structural Dynamics 2025: eqe.70086. DOI: 10.1002/eqe.70086.
110. Mavroeidis GP, Papageorgiou AS. A Mathematical Representation of Near-Fault Ground Motions. Bulletin of the Seismological Society of America 2003; 93(3): 1099–1131. DOI: 10.1785/0120020100.
111. Somerville P. Seismic hazard evaluation. Bulletin of the New Zealand Society for Earthquake Engineering 2000; 33(3): 371–386. DOI: 10.5459/bnzsee.33.3.371-386.
112. Bozorgnia Y, Campbell KW. Vertical Ground Motion Model for PGA, PGV, and Linear Response Spectra Using the NGA-West2 Database. Earthquake Spectra 2016; 32(2): 979–1004. DOI: 10.1193/072814eqs121m.

Appendix

Based on Parseval's theorem, assuming a zero mean unit variance Gaussian white noise process ($\mathrm{E}[\mathrm{w}(\tau_1)\mathrm{w}(\tau_2)] = 0$ and $\mathrm{E}[\mathrm{w}(\tau)^2] = 1$), and the equivalent energy normalization functions in Equations 2.3 and 2.4, It follows that:

In time domain:

$$\begin{aligned}\mathrm{E}\left[\int_{-\infty}^{\infty} \mathrm{x}^2(\mathrm{t})\mathrm{dt}\right] &= \int_{-\infty}^{\infty}\int_{-\infty}^{\infty} \mathrm{q}^2(\tau,\alpha)\mathrm{E}[\mathrm{w}^2(\tau)]\frac{\mathrm{h}^2\big(\mathrm{t}-\tau,\lambda(\tau)\big)}{\gamma_{\mathrm{h}}^2(\tau)}\mathrm{d}\tau\,\mathrm{dt} \\ &= \int_{-\infty}^{\infty} \mathrm{q}^2(\tau,\alpha)\frac{\int_{-\infty}^{\infty}\mathrm{h}^2\big(\mathrm{t}-\tau,\lambda(\tau)\big)\mathrm{dt}}{\int_{-\infty}^{\infty}\mathrm{h}^2\big(\mathrm{t}-\tau,\lambda(\tau)\big)\mathrm{dt}}\mathrm{d}\tau = \int_{-\infty}^{\infty}\mathrm{q}^2(\tau,\alpha)\,\mathrm{d}\tau \\ &= \int_{-\infty}^{\infty}\mathrm{q}^2(\mathrm{t},\alpha)\,\mathrm{dt}\end{aligned} \qquad \text{A1}$$

In frequency domain:

$$\begin{aligned}\mathrm{E}\left[\int_{-\infty}^{\infty}|\mathrm{X}(\bar{\omega})|^2\,\mathrm{d}\bar{\omega}\right] &= \int_{-\infty}^{\infty}\int_{-\infty}^{\infty}\mathrm{q}^2(\tau,\alpha)\mathrm{E}[\mathrm{w}^2(\tau)]\frac{\left|e^{-\mathrm{i}\bar{\omega}\tau}\right|^2\left|\mathrm{H}\big(\bar{\omega},\lambda(\tau)\big)\right|^2}{\gamma_{\mathrm{H}}^2(\tau)}\,\mathrm{d}\tau\,\mathrm{d}\bar{\omega} \\ &= \int_{-\infty}^{\infty}\mathrm{q}^2(\tau,\alpha)\frac{\int_{-\infty}^{+\infty}\left|\mathrm{H}\big(\bar{\omega},\lambda(\tau)\big)\right|^2\mathrm{d}\bar{\omega}}{\int_{-\infty}^{+\infty}\left|\mathrm{H}\big(\bar{\omega},\lambda(\tau)\big)\right|^2\mathrm{d}\bar{\omega}}\mathrm{d}\tau = \int_{-\infty}^{\infty}\mathrm{q}^2(\tau,\alpha)\,\mathrm{d}\tau \\ &= \int_{-\infty}^{\infty}\mathrm{q}^2(\mathrm{t},\alpha)\,\mathrm{dt}\end{aligned} \qquad \text{A2}$$

Thus, the energy of the model (either in the time or frequency domain) is controlled by the modulating function.

Table A1. Selected pan-European strong motion (ESM) dataset for the February 6, 2023, Kahramanmaraş, Türkiye, earthquake (M_w = 7.8) [80,81]. Parameters include moment magnitude (M_w), Joyner-Boore distance (R_{JB}), rupture distance (R_{rup}), averaged shear wave velocity at the top 30 m of soil (V_{S30}), and largest pulse period (T_p).

#	ESM ID	Country	Year	Station Code	M_w	Mechanism	R_{JB} (km)	R_{rup} (km)	V_{S30} (m/s)	T_p (s)
1	INT-20230206-0000008	Türkiye	2023	KHMN	7.8	Strike-slip	0.0	4.7	587	-
2	INT-20230206-0000008	Türkiye	2023	2308	7.8	Strike-slip	61.8	62.0	547	-
3	INT-20230206-0000008	Türkiye	2023	2703	7.8	Strike-slip	32.0	35.2	311	-
4	INT-20230206-0000008	Türkiye	2023	2708	7.8	Strike-slip	1.0	2.1	210	3.2
5	INT-20230206-0000008	Türkiye	2023	2709	7.8	Strike-slip	0.6	2.0	427	-
6	INT-20230206-0000008	Türkiye	2023	2712	7.8	Strike-slip	0.0	2.6	403	7.1
7	INT-20230206-0000008	Türkiye	2023	2715	7.8	Strike-slip	4.5	13.6	794	-
8	INT-20230206-0000008	Türkiye	2023	2716	7.8	Strike-slip	4.7	13.8	410	7.1
9	INT-20230206-0000008	Türkiye	2023	2717	7.8	Strike-slip	5.0	14.0	790	7.0
10	INT-20230206-0000008	Türkiye	2023	2718	7.8	Strike-slip	0.0	2.5	373	-
11	INT-20230206-0000008	Türkiye	2023	3116	7.8	Strike-slip	13.7	13.9	513	14.5
12	INT-20230206-0000008	Türkiye	2023	3123	7.8	Strike-slip	0.0	2.4	322	2.3
13	INT-20230206-0000008	Türkiye	2023	3124	7.8	Strike-slip	0.0	2.3	377	3.4
14	INT-20230206-0000008	Türkiye	2023	3131	7.8	Strike-slip	0.0	3.4	825	-
15	INT-20230206-0000008	Türkiye	2023	3132	7.8	Strike-slip	0.0	3.3	414	-
16	INT-20230206-0000008	Türkiye	2023	3133	7.8	Strike-slip	24.5	32.9	316	-
17	INT-20230206-0000008	Türkiye	2023	3134	7.8	Strike-slip	23.8	23.9	284	-
18	INT-20230206-0000008	Türkiye	2023	3136	7.8	Strike-slip	4.0	13.2	519	-
19	INT-20230206-0000008	Türkiye	2023	3137	7.8	Strike-slip	0.0	5.8	513	9.3
20	INT-20230206-0000008	Türkiye	2023	3138	7.8	Strike-slip	0.0	2.8	367	7.7
21	INT-20230206-0000008	Türkiye	2023	3139	7.8	Strike-slip	0.0	5.0	353	-
22	INT-20230206-0000008	Türkiye	2023	3142	7.8	Strike-slip	0.0	5.2	376	-
23	INT-20230206-0000008	Türkiye	2023	3143	7.8	Strike-slip	0.0	4.1	367	7.2
24	INT-20230206-0000008	Türkiye	2023	3144	7.8	Strike-slip	0.0	2.9	447	8.3
25	INT-20230206-0000008	Türkiye	2023	3145	7.8	Strike-slip	0.0	2.2	533	4.1
26	INT-20230206-0000008	Türkiye	2023	4404	7.8	Strike-slip	16.4	18.1	653	-
27	INT-20230206-0000008	Türkiye	2023	4611	7.8	Strike-slip	15.8	16.0	553	14.0
28	INT-20230206-0000008	Türkiye	2023	4612	7.8	Strike-slip	78.2	78.2	242	-

#	ESM ID	Country	Year	Station Code	M_w	Mechanism	R_{JB} (km)	R_{rup} (km)	V_{S30} (m/s)	T_p (s)
29	INT-20230206-0000008	Türkiye	2023	4613	7.8	Strike-slip	46.8	46.9	513	-
30	INT-20230206-0000008	Türkiye	2023	4614	7.8	Strike-slip	6.0	9.8	474	-
31	INT-20230206-0000008	Türkiye	2023	4615	7.8	Strike-slip	0.0	4.2	224	5.7
32	INT-20230206-0000008	Türkiye	2023	4616	7.8	Strike-slip	1.2	2.3	302	8.0
33	INT-20230206-0000008	Türkiye	2023	4620	7.8	Strike-slip	17.6	17.7	414	-
34	INT-20230206-0000008	Türkiye	2023	4624	7.8	Strike-slip	12.0	12.2	346	-
35	INT-20230206-0000008	Türkiye	2023	4629	7.8	Strike-slip	0.0	2.3	351	-
36	INT-20230206-0000008	Türkiye	2023	4632	7.8	Strike-slip	0.0	2.5	339	-
37	INT-20230206-0000008	Türkiye	2023	6304	7.8	Strike-slip	72.0	74.9	481	-
38	INT-20230206-0000008	Türkiye	2023	8002	7.8	Strike-slip	12.3	12.4	682	8.3
39	INT-20230206-0000008	Türkiye	2023	8003	7.8	Strike-slip	30.7	30.8	358	12.4
40	INT-20230206-0000008	Türkiye	2023	8004	7.8	Strike-slip	58.4	58.5	341	-
41	INT-20230206-0000008	Türkiye	2023	NAR	7.8	Strike-slip	0.0	4.7	587	4.7

Table A2. Selected Next Generation Attenuation Relationships for Western United States (NGA-West2) dataset of near-fault pulse-like records [83]. Parameters include moment magnitude (M_w), Joyner-Boore distance (R_{JB}), rupture distance (R_{rup}), averaged shear wave velocity at the top 30 m of soil (V_{S30}), and largest pulse period (T_p).

#	Earthquake Name	Year	Station Name	M_w	Mechanism	R_{JB} (km)	R_{rup} (km)	V_{S30} (m/s)	T_p (s)
1	San Fernando	1971	Pacoima Dam (upper left abut)	6.61	Reverse	0.00	1.81	2016.1	1.64
2	Tabas, Iran	1978	Tabas	7.35	Reverse	1.79	2.05	766.8	6.19
3	Imperial Valley-06	1979	Agrarias	6.53	Strike-slip	0.00	0.65	242.1	2.34
4	Imperial Valley-06	1979	Brawley Airport	6.53	Strike-slip	8.54	10.42	208.7	4.40
5	Imperial Valley-06	1979	EC County Center FF	6.53	Strike-slip	7.31	7.31	192.1	4.42
6	Imperial Valley-06	1979	El Centro - Meloland Geot. Array	6.53	Strike-slip	0.07	0.07	264.6	3.42
7	Imperial Valley-06	1979	El Centro Array #10	6.53	Strike-slip	8.60	8.60	202.9	4.52
8	Imperial Valley-06	1979	El Centro Array #4	6.53	Strike-slip	4.90	7.05	208.9	4.79
9	Imperial Valley-06	1979	El Centro Array #5	6.53	Strike-slip	1.76	3.95	205.6	4.13
10	Imperial Valley-06	1979	El Centro Array #6	6.53	Strike-slip	0.00	1.35	203.2	3.77
11	Imperial Valley-06	1979	El Centro Array #7	6.53	Strike-slip	0.56	0.56	210.5	4.38
12	Imperial Valley-06	1979	El Centro Differential Array	6.53	Strike-slip	5.09	5.09	202.3	6.27
13	Imperial Valley-06	1979	Holtville Post Office	6.53	Strike-slip	5.35	7.50	202.9	4.82
14	Irpinia, Italy-01	1980	Bagnoli Irpinia	6.90	Normal	8.14	8.18	649.7	1.71
15	Irpinia, Italy-01	1980	Sturno (STN)	6.90	Normal	6.78	10.84	382.0	3.27
16	Morgan Hill	1984	Coyote Lake Dam–Southwest Abutment	6.19	Strike-slip	0.18	0.53	561.4	1.07
17	Morgan Hill	1984	Gilroy Array #6	6.19	Strike-slip	9.85	9.87	663.3	1.23
18	Superstition Hills-02	1987	Parachute Test Site	6.54	Strike-slip	0.95	0.95	348.7	2.39
19	Loma Prieta	1989	Saratoga - Aloha Ave	6.93	Reverse Oblique	7.58	8.50	380.9	4.57
20	Loma Prieta	1989	Saratoga - W Valley Coll.	6.93	Reverse Oblique	8.48	9.31	347.9	5.65
21	Cape Mendocino	1992	Petrolia	7.01	Reverse	0.00	8.18	422.2	3.00
22	Landers	1992	Lucerne	7.28	Strike-slip	2.19	2.19	1369.0	5.12
23	Northridge-01	1994	Jensen Filter Plant Administrative Building	6.69	Reverse	0.00	5.43	373.1	3.16
24	Northridge-01	1994	Jensen Filter Plant Generator Building	6.69	Reverse	0.00	5.43	525.8	3.54
25	Northridge-01	1994	LA - Sepulveda VA Hospital	6.69	Reverse	0.00	8.44	380.1	0.93
26	Northridge-01	1994	LA Dam	6.69	Reverse	0.00	5.92	629.0	1.62
27	Northridge-01	1994	Newhall - Fire Sta	6.69	Reverse	3.16	5.92	269.1	1.37
28	Northridge-01	1994	Newhall - W Pico Canyon Rd.	6.69	Reverse	2.11	5.48	285.9	2.98
29	Northridge-01	1994	Pacoima Dam (downstr)	6.69	Reverse	4.92	7.01	2016.1	0.59
30	Northridge-01	1994	Pacoima Dam (upper left)	6.69	Reverse	4.92	7.01	2016.1	0.84

#	Earthquake Name	Year	Station Name	M_w	Mechanism	R_{JB} (km)	R_{rup} (km)	V_{S30} (m/s)	T_p (s)
31	Northridge-01	1994	Pacoima Kagel Canyon	6.69	Reverse	5.26	7.26	508.1	0.73
32	Northridge-01	1994	Pardee - SCE	6.69	Reverse	5.54	7.46	325.7	1.23
33	Northridge-01	1994	Rinaldi Receiving Sta	6.69	Reverse	0.00	6.50	282.3	1.25
34	Northridge-01	1994	Sylmar - Converter Sta	6.69	Reverse	0.00	5.35	251.2	2.98
35	Northridge-01	1994	Sylmar - Converter Sta East	6.69	Reverse	0.00	5.19	370.5	3.53
36	Northridge-01	1994	Sylmar - Olive View Med FF	6.69	Reverse	1.74	5.30	440.5	2.44
37	Kobe, Japan	1995	KJMA	6.90	Strike-slip	0.94	0.96	312.0	1.09
38	Kobe, Japan	1995	Port Island (0 m)	6.90	Strike-slip	3.31	3.31	198.0	2.83
39	Kobe, Japan	1995	Takarazuka	6.90	Strike-slip	0.00	0.27	312.0	1.81
40	Kobe, Japan	1995	Takatori	6.90	Strike-slip	1.46	1.47	256.0	1.55
41	Kocaeli, Türkiye	1999	Gebze	7.51	Strike-slip	7.57	10.92	792.0	5.99
42	Kocaeli, Türkiye	1999	Izmit	7.51	Strike-slip	3.62	7.21	811.0	5.37
43	Kocaeli, Türkiye	1999	Yarimca	7.51	Strike-slip	1.38	4.83	297.0	4.95
44	Chi-Chi, Taiwan	1999	CHY006	7.62	Reverse Oblique	9.76	9.76	438.2	2.57
45	Chi-Chi, Taiwan	1999	CHY024	7.62	Reverse Oblique	9.62	9.62	427.7	6.65
46	Chi-Chi, Taiwan	1999	CHY101	7.62	Reverse Oblique	9.94	9.94	258.9	5.34
47	Chi-Chi, Taiwan	1999	TCU049	7.62	Reverse Oblique	3.76	3.76	487.3	10.22
48	Chi-Chi, Taiwan	1999	TCU051	7.62	Reverse Oblique	7.64	7.64	350.1	10.38
49	Chi-Chi, Taiwan	1999	TCU052	7.62	Reverse Oblique	0.00	0.66	579.1	11.96
50	Chi-Chi, Taiwan	1999	TCU053	7.62	Reverse Oblique	5.95	5.95	454.6	13.12
51	Chi-Chi, Taiwan	1999	TCU063	7.62	Reverse Oblique	9.78	9.78	476.1	6.55
52	Chi-Chi, Taiwan	1999	TCU065	7.62	Reverse Oblique	0.57	0.57	305.9	5.74
53	Chi-Chi, Taiwan	1999	TCU068	7.62	Reverse Oblique	0.00	0.32	487.3	12.29
54	Chi-Chi, Taiwan	1999	TCU075	7.62	Reverse Oblique	0.89	0.89	573.0	5.00
55	Chi-Chi, Taiwan	1999	TCU076	7.62	Reverse Oblique	2.74	2.74	615.0	4.73
56	Chi-Chi, Taiwan	1999	TCU082	7.62	Reverse Oblique	5.16	5.16	472.8	8.10
57	Chi-Chi, Taiwan	1999	TCU087	7.62	Reverse Oblique	6.98	6.98	538.7	10.40
58	Chi-Chi, Taiwan	1999	TCU101	7.62	Reverse Oblique	2.11	2.11	389.4	10.32
59	Chi-Chi, Taiwan	1999	TCU102	7.62	Reverse Oblique	1.49	1.49	714.3	9.63
60	Chi-Chi, Taiwan	1999	TCU103	7.62	Reverse Oblique	6.08	6.08	494.1	8.69
61	Chi-Chi, Taiwan	1999	TCU136	7.62	Reverse Oblique	8.27	8.27	462.1	8.88
62	Denali, Alaska	2002	TAPS Pump Station #10	7.90	Strike-slip	0.18	2.74	329.4	3.16
63	Chi-Chi, Taiwan-04	1999	CHY074	6.20	Strike-slip	6.02	6.20	553.4	2.44
64	Chi-Chi, Taiwan-06	1999	TCU078	6.30	Reverse	5.72	11.52	443.0	4.15
65	Chi-Chi, Taiwan-06	1999	TCU080	6.30	Reverse	0.00	10.20	489.3	1.02

#	Earthquake Name	Year	Station Name	M_w	Mechanism	R_{JB} (km)	R_{rup} (km)	V_{S30} (m/s)	T_p (s)
66	Loma Prieta	1989	Los Gatos - Lexington Dam	6.93	Reverse Oblique	3.22	5.02	1070.3	1.57
67	Cape Mendocino	1992	Bunker Hill FAA	7.01	Reverse	8.49	12.24	566.4	5.36
68	Tottori, Japan	2000	TTR008	6.61	Strike-slip	6.86	6.88	139.2	1.54
69	Bam, Iran	2003	Bam	6.60	Strike-slip	0.05	1.70	487.4	2.02
70	Parkfield-02, CA	2004	PARKFIELD - EADES	6.00	Strike-slip	1.37	2.85	383.9	1.22
71	Parkfield-02, CA	2004	Slack Canyon	6.00	Strike-slip	1.60	2.99	648.1	0.85
72	Parkfield-02, CA	2004	Parkfield - Cholame 1E	6.00	Strike-slip	1.66	3.00	326.6	1.33
73	Parkfield-02, CA	2004	Parkfield - Cholame 2WA	6.00	Strike-slip	1.63	3.01	173.0	1.08
74	Parkfield-02, CA	2004	Parkfield - Cholame 3E	6.00	Strike-slip	4.95	5.55	397.4	0.52
75	Parkfield-02, CA	2004	Parkfield - Cholame 3W	6.00	Strike-slip	2.55	3.63	230.6	1.02
76	Parkfield-02, CA	2004	Parkfield - Cholame 4W	6.00	Strike-slip	3.30	4.23	410.4	0.70
77	Parkfield-02, CA	2004	Parkfield - Fault Zone 1	6.00	Strike-slip	0.02	2.51	178.3	1.19
78	Parkfield-02, CA	2004	Parkfield - Fault Zone 9	6.00	Strike-slip	1.22	2.85	372.3	1.13
79	Parkfield-02, CA	2004	Parkfield - Fault Zone 12	6.00	Strike-slip	0.88	2.65	265.2	1.19
80	Parkfield-02, CA	2004	Parkfield - Stone Corral 1E	6.00	Strike-slip	2.85	3.79	260.6	0.57
81	Niigata, Japan	2004	NIGH11	6.63	Reverse	6.27	8.93	375.0	1.80
82	Montenegro, Yugoslavia	1979	Bar-Skupstina Opstine	7.10	Reverse	0.00	6.98	462.2	1.44
83	Montenegro, Yugoslavia	1979	Ulcinj - Hotel Olimpic	7.10	Reverse	3.97	5.76	318.7	1.97
84	L'Aquila, Italy	2009	L'Aquila - V. Aterno - Centro Valle	6.30	Normal	0.00	6.27	475.0	1.07
85	L'Aquila, Italy	2009	L'Aquila - V. Aterno -F. Aterno	6.30	Normal	0.00	6.55	552.0	1.18
86	L'Aquila, Italy	2009	L'Aquila - Parking	6.30	Normal	0.00	5.38	717.0	1.98
87	Chuetsu-oki, Japan	2007	Joetsu Kakizakiku Kakizaki	6.80	Reverse	9.43	11.94	383.4	1.40
88	Darfield, New Zealand	2010	DSLC	7.00	Strike-slip	5.28	8.46	295.7	7.83
89	Darfield, New Zealand	2010	GDLC	7.00	Strike-slip	1.22	1.22	344.0	6.23
90	Darfield, New Zealand	2010	HORC	7.00	Strike-slip	7.29	7.29	326.0	9.92
91	Darfield, New Zealand	2010	LINC	7.00	Strike-slip	5.07	7.11	263.2	7.37
92	Darfield, New Zealand	2010	ROLC	7.00	Strike-slip	0.00	1.54	295.7	7.14
93	Darfield, New Zealand	2010	TPLC	7.00	Strike-slip	6.11	6.11	249.3	8.93
94	Christchurch, New Zealand	2011	Pages Road Pumping Station	6.20	Reverse Oblique	1.92	1.98	206.0	4.82
95	Christchurch, New Zealand	2011	Christchurch Resthaven	6.20	Reverse Oblique	5.11	5.13	141.0	1.55
96	El Mayor-Cucapah, Mexico	2010	El Centro Array #12	7.20	Strike-slip	9.98	11.26	196.9	8.72
97	Duzce, Türkiye	1999	IRIGM 487	7.14	Strike-slip	2.65	2.65	690.0	10.05

Table A3. Performance metrics for all response variables across the three principal axes.

Variable	R^2	r	MAE	RMSE	Between-event SD	Between-site SD	Within-event SD	Total SD
D_M	0.275	0.601	0.518	0.618	0.469	0.373	0.48	0.768
D_I	0.298	0.6	0.498	0.587	0.5	0.368	0.482	0.786
D_V	0.26	0.598	0.529	0.638	0.507	0.346	0.441	0.756
C_M	0.156	0.625	0.608	0.714	0.544	0.32	0.532	0.825
C_I	0.243	0.654	0.558	0.653	0.581	0.308	0.512	0.834
C_V	0.418	0.741	0.502	0.601	0.509	0.281	0.429	0.723
S_M	0.203	0.646	0.572	0.69	0.539	0.313	0.512	0.807
S_I	0.235	0.652	0.535	0.63	0.588	0.308	0.5	0.831
S_V	0.231	0.683	0.534	0.64	0.454	0.308	0.474	0.725
E_M	0.854	0.927	0.937	1.095	0.394	0.296	0.269	0.561
E_I	0.851	0.924	0.945	1.113	0.384	0.302	0.257	0.552
E_V	0.815	0.903	0.965	1.18	0.429	0.259	0.265	0.567
$f_{U, M}$	0.58	0.777	0.321	0.405	0.599	0.545	0.478	0.94
$f_{U, I}$	0.538	0.739	0.333	0.414	0.579	0.566	0.454	0.928
$f_{U, V}$	0.482	0.72	0.366	0.439	0.581	0.597	0.432	0.938
$f_{L, M}$	0.405	0.828	0.632	0.756	0.519	0.206	0.489	0.743
$f_{L, I}$	0.446	0.817	0.606	0.738	0.487	0.208	0.483	0.716
$f_{L, V}$	0.31	0.791	0.646	0.807	0.54	0.174	0.473	0.739
PGV_M	0.892	0.945	0.466	0.555	0.424	0.245	0.346	0.6
PGV_I	0.893	0.946	0.46	0.556	0.391	0.246	0.324	0.564
PGV_V	0.848	0.93	0.498	0.608	0.46	0.182	0.341	0.6
PGA_M	0.784	0.903	0.568	0.69	0.397	0.302	0.369	0.621
PGA_I	0.796	0.906	0.546	0.662	0.382	0.316	0.353	0.609
PGA_V	0.772	0.894	0.586	0.711	0.39	0.275	0.339	0.586
$SA_{0.03s, M}$	0.778	0.899	0.573	0.695	0.401	0.303	0.369	0.624
$SA_{0.03s, I}$	0.799	0.908	0.535	0.656	0.39	0.317	0.354	0.615
$SA_{0.03s, V}$	0.766	0.892	0.612	0.743	0.425	0.29	0.337	0.615
$SA_{0.05s, M}$	0.764	0.894	0.591	0.713	0.421	0.307	0.369	0.638

Variable	R^2	r	MAE	RMSE	Between-event SD	Between-site SD	Within-event SD	Total SD
$SA_{0.05s, I}$	0.76	0.889	0.593	0.716	0.41	0.324	0.352	0.63
$SA_{0.05s, V}$	0.75	0.886	0.669	0.802	0.442	0.328	0.317	0.636
$SA_{0.08s, M}$	0.702	0.862	0.664	0.806	0.43	0.349	0.366	0.664
$SA_{0.08s, I}$	0.729	0.873	0.636	0.765	0.411	0.365	0.348	0.65
$SA_{0.08s, V}$	0.749	0.885	0.678	0.815	0.416	0.36	0.313	0.633
$SA_{0.1s, M}$	0.727	0.878	0.657	0.781	0.425	0.348	0.366	0.66
$SA_{0.1s, I}$	0.739	0.879	0.636	0.752	0.403	0.362	0.35	0.645
$SA_{0.1s, V}$	0.735	0.878	0.708	0.835	0.407	0.339	0.325	0.622
$SA_{0.16s, M}$	0.712	0.869	0.677	0.806	0.388	0.348	0.375	0.642
$SA_{0.16s, I}$	0.751	0.882	0.624	0.735	0.384	0.367	0.349	0.635
$SA_{0.16s, V}$	0.713	0.866	0.709	0.84	0.398	0.313	0.342	0.611
$SA_{0.2s, M}$	0.722	0.874	0.667	0.792	0.378	0.334	0.375	0.629
$SA_{0.2s, I}$	0.755	0.883	0.615	0.729	0.38	0.343	0.366	0.629
$SA_{0.2s, V}$	0.719	0.86	0.661	0.797	0.387	0.307	0.356	0.609
$SA_{0.3s, M}$	0.778	0.894	0.599	0.711	0.381	0.321	0.403	0.64
$SA_{0.3s, I}$	0.792	0.902	0.568	0.692	0.377	0.322	0.374	0.621
$SA_{0.3s, V}$	0.742	0.871	0.606	0.744	0.424	0.323	0.369	0.648
$SA_{0.4s, M}$	0.794	0.902	0.607	0.73	0.423	0.332	0.392	0.665
$SA_{0.4s, I}$	0.804	0.908	0.585	0.721	0.405	0.333	0.365	0.639
$SA_{0.4s, V}$	0.78	0.889	0.572	0.699	0.46	0.315	0.37	0.67
$SA_{0.5s, M}$	0.799	0.906	0.612	0.768	0.454	0.326	0.38	0.676
$SA_{0.5s, I}$	0.824	0.92	0.564	0.708	0.408	0.331	0.368	0.642
$SA_{0.5s, V}$	0.805	0.901	0.541	0.678	0.46	0.3	0.358	0.656
$SA_{0.75s, M}$	0.854	0.929	0.539	0.665	0.458	0.312	0.368	0.665
$SA_{0.75s, I}$	0.846	0.926	0.548	0.679	0.44	0.309	0.363	0.649
$SA_{0.75s, V}$	0.839	0.916	0.506	0.619	0.456	0.272	0.359	0.641
$SA_{1.0s, M}$	0.85	0.922	0.568	0.697	0.465	0.302	0.362	0.662
$SA_{1.0s, I}$	0.853	0.924	0.566	0.688	0.464	0.306	0.35	0.657
$SA_{1.0s, V}$	0.81	0.91	0.566	0.71	0.471	0.264	0.367	0.653

Variable	R^2	r	MAE	RMSE	Between-event SD	Between-site SD	Within-event SD	Total SD
$SA_{1.5s, M}$	0.858	0.931	0.567	0.706	0.498	0.311	0.354	0.686
$SA_{1.5s, I}$	0.846	0.923	0.604	0.754	0.491	0.307	0.346	0.674
$SA_{1.5s, V}$	0.787	0.908	0.624	0.794	0.532	0.269	0.356	0.694
$SA_{2.0s, M}$	0.856	0.941	0.6	0.733	0.489	0.311	0.339	0.671
$SA_{2.0s, I}$	0.849	0.93	0.635	0.771	0.482	0.309	0.332	0.662
$SA_{2.0s, V}$	0.801	0.924	0.662	0.818	0.56	0.269	0.348	0.712
$SA_{3.0s, M}$	0.822	0.928	0.77	0.901	0.501	0.283	0.318	0.657
$SA_{3.0s, I}$	0.83	0.929	0.764	0.902	0.493	0.292	0.307	0.65
$SA_{3.0s, V}$	0.74	0.924	0.872	1.021	0.58	0.238	0.33	0.709
$SA_{4.0s, M}$	0.836	0.941	0.74	0.88	0.505	0.248	0.308	0.641
$SA_{4.0s, I}$	0.833	0.936	0.772	0.914	0.493	0.246	0.296	0.625
$SA_{4.0s, V}$	0.755	0.931	0.9	1.059	0.57	0.209	0.322	0.687